HELLENIC REPUBLIC
National and Kapodistrian University of Athens
EST. 1837

Quantum states in materials with complex topological electronic and magnetic structure

Adamantia Kosma

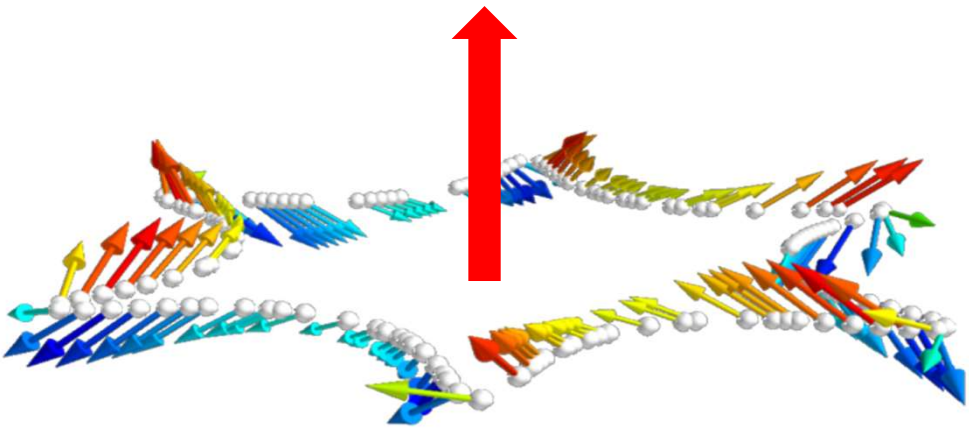

PhD Thesis
Athens, January 2023

HELLENIC REPUBLIC
National and Kapodistrian University of Athens
Department of Physics
Section of Condensed Matter Physics

Quantum states in materials with complex topological electronic and magnetic structure

Adamantia Kosma

Examination Committee

Professor Phivos Mavropoulos (Supervisor), *National and Kapodistrian University of Athens*
Professor Nikolaos Stefanou (Member of the advisory committee), *National and Kapodistrian University of Athens*
Professor Yuriy Mokrousov (Member of the advisory committee), *Johannes Gutenberg-Universität Mainz and Forschungszentrum Jülich*
Dr. Marjana Lezaic, *Forschungszentrum Jülich*
Professor Iosif Galanakis, *University of Patras*
Dr. Athanasios Dimoulas, *NCSR Demokritos*
Professor George Kioseoglou, *University of Crete*

PhD Thesis
Athens, January 2023

H.F.R.I.
Hellenic Foundation for
Research & Innovation

Deutscher Akademischer Austauschdienst
German Academic Exchange Service

"Μία αστραπή η ζωή μας...
μα προλαβαίνουμε!"

Νίκος Καζαντζάκης

Abstract

The research on the complex topological electronic and magnetic structure of materials has been gaining importance over the last few years, as it can be applied in the field of spintronics with prospects for implementation in information technology.

The main goal of this thesis is the theoretical and computational study of spin-transport phenomena in topological structures. Our simulations are based on ab-initio calculations augmented by electronic scattering theory.

Firstly, we focus on the phenomenon of the spin-orbit torque in a special materials class, the topological insulators, doped with magnetic impurities. We investigate the spin-orbit torque exerted on the magnetic moments of ferromagnetically coupled transition-metal defects (Cr, Mn, Fe, and Co) embedded in the surface of the topological insulator Bi_2Te_3, in response to an electrical current flow in the surface. The scattering properties of surface states off multiple magnetic impurities are calculated within the Korringa-Kohn-Rostoker (KKR) Green function method, while the spin-orbit torque calculations are performed by combining the KKR results on the Fermi surface and scattering rate with the semiclassical linearized Boltzmann equation. We discuss the correlation of the spin-orbit torque to the spin current on the Fermi surface, analyzing the spin flux contribution to the spin-orbit torque on the defects. In addition, we relate the torque to the resistivity and the Joule heat production. We find these systems may be favorable for spintronic applications. In particular, we predict that the Mn/Bi_2Te_3 is the most promising among the studied systems for applications of the spin-orbit torque effect.

Secondly, we focus on magnetic skyrmions in magnetic films, which are two-dimensional topological solitons that behave like particles that can be formed, transported, detected. Based on the KKR method, non-collinear spin-density-functional theory calculations are carried out for the formation of stable magnetic skyrmions in Pd/Fe/Ir(111) ultrathin films. Next, solving selfconsistently the Boltzmann transport equation, we study the topological Hall effect (THE) induced by the electron scattering on skyrmion systems. The investigation of the THE is of pivotal importance in these systems, since it is one of the key methods for electrically detecting magnetic skyrmions. We present the resistivity and the Hall angle of the system, and we examine the dependence of the THE on disorder, modelled by an additional electron scattering term. Our findings predict a strong dependence of the topological Hall angle on the degree of disorder of the sample.

Περίληψη

Η σύνθετη τοπολογική ηλεκτρονική και μαγνητική δομή των υλικών είναι ένα πεδίο έρευνας που αποκτά όλο και μεγαλύτερη σημασία τα τελευταία χρόνια, λόγω της εφαρμογής του στο πεδίο της σπιντρονικής, με πιθανές προεκτάσεις στην πληροφορία της τεχνολογίας.

Στην παρούσα διδακτορική διατριβή, κύριο στόχο αποτελεί η θεωρητική και υπολογιστική μελέτη φαινομένων μεταφοράς του σπιν σε τοπολογικές δομές. Οι προσομοιώσεις μας βασίζονται σε υπολογισμούς υλικών από πρώτες αρχές εφαρμόζοντας τη θεωρία ηλεκτρονικής σκέδασης.

Αρχικά, επικεντρωνόμαστε στο φαινόμενο της ροπής στρέψης σπιν σε τοπολογικούς μονωτές εμπλουτισμένους με μαγνητικές προσμίξεις. Μελετούμε τη ροπή στρέψης σπιν που ασκείται στη μαγνητική ροπή σιδηρομαγνητικά συζευγμένων προσμίξεων, και συγκεκριμένα μετάλλων μετάβασης (Cr, Mn, Fe, και Co), στην επιφάνεια του τοπολογικού μονωτή Bi_2Te_3, ως απόκριση σε ηλεκτρικό ρεύματος στην επιφάνεια. Οι ιδιότητες σκέδασης των επιφανειακών καταστάσεων στις μαγνητικές προσμίξεις υπολογίζονται με τη μέθοδο Korringa-Kohn-Rostoker (KKR) συναρτήσεων Green, ενώ οι υπολογισμοί της ροπής στρέψης σπιν πραγματοποιούνται συνδυάζοντας τα αποτελέσματα της KKR στην επιφάνεια Fermi και το ρυθμό σκέδασης με την ημικλασική γραμμικοποιημένη εξίσωση Boltzmann. Συζητάμε τη συσχέτιση της ροπής στρέψης σπιν με το ρεύμα σπιν, αναλύοντας τη συνεισφορά της ροής σπιν στη ροπή στρέψης σπιν στις προσμίξεις. Επιπλέον, εξετάζουμε πώς σχετίζεται η ροπή στρέψης σπιν με την αντίσταση και την παραγωγή θερμότητας Joule. Σύμφωνα με τα αποτελέσματά μας, τα συστήματα αυτά είναι ευνοϊκά για σπιντρονικές εφαρμογές. Ειδικότερα, προβλέπουμε ότι το σύστημα Mn/Bi_2Te_3 είναι το πλέον υποσχόμενο μεταξύ των συστημάτων που μελετήσαμε για εφαρμογές της ροπής στρέψης σπιν.

Στη συνέχεια, επικεντρωνόμαστε στη μελέτη διδιάστατων μαγνητικών σκυρμιονίων, τα οποία είναι τοπολογικά σολιτόνια σε σιδηρομαγνητικά υμένια και τα οποία συμπεριφέρονται ως σωματίδια που δύνανται να σχηματιστούν, μεταφερθούν και ανιχνευθούν. Για τη μελέτη αυτή, βασιστήκαμε στη μέθοδο KKR και πραγματοποιήσαμε υπολογισμούς θεωρίας συναρτησιακού της μη συγγραμικής πυκνότητας σπιν για το σχηματισμό ευσταθών μαγνητικών σκυρμιονίων σε υπέρλεπτα υμένια Pd/Fe/Ir(111). Κατόπιν, επιλύοντας την αυτοσυνεπή εξίσωση Boltzmann, εξετάζουμε το τοπολογικό φαινόμενο Hall, το οποίο προκαλείται από τη σκέδαση των ηλεκτρονίων σε συστήματα σκυρμιονίων. Η μελέτη του τοπολογικού φαινομένου Hall είναι θεμελιώδους σημασίας σε τέτοιου είδους συστήματα, καθώς το φαινόμενο αυτό αποτελεί μία από τις βασικές μεθόδους για την ανίχνευση μαγνητικών σκυρμιονίων. Παρουσιάζουμε την αντίσταση και τη γωνία Hall του συστήματος, και εξετάζουμε την εξάρτηση του τοπολογικού φαινομένου Hall από το βαθμό αταξίας του δείγματος, εισάγοντάς τον στους υπολογισμούς μας μέσω ενός επιπλέον όρου ηλεκτρονικής σκέδασης. Τα ευρήματά μας προβλέπουν μία ισχυρή εξάρτηση του τοπολογικού φαινομένου Hall από το βαθμό αταξίας του δείγματος.

Contents

Abbreviations

The following abbreviations are frequently used in this thesis:

Abbr.	Meaning
AHE	anomalous Hall effect
DFT	density functional theory
DOS	density of states
GF	Green function
KKR	Korringa Kohn Rostoker
LDA	local density approximation
MRAM	magnetoresistive random-access memory
SOC	spin-orbit coupling
SOT	spin-orbit torque
STT	spin-transfer torque
THE	topological Hall effect
THA	topological Hall angle

1 Introduction

Information technology plays an important role in our everyday lives. The field of spintronics [1, 2], that aims at controlling the electron spin degree of freedom in solid-state systems, is a powerful tool for the design energetically efficient devices with applications in information technology.

Spintronic devices are used as data storage, manipulation and transport devices. One of the main challenges in their design is the conservation of the information in materials structures, without dissipation. To this end, the complex topology of electronic and magnetic structures can be a key element. On the one hand, materials like topological insulators show a topological structure in momentum-space with protected metallic surface states, and on the other hand, magnetic skyrmions appear as topological states in real space, with a potential for efficient storage and transport of information.

A very active area in the field of spintronics is the "electrically controlled spintronics" that is related to the manipulation and detection of the magnetization by means of an electric field and by the resulting electric current, allowing for high-density magnetic memory components in magnetism-based memory devices [3, 4]. The area was pioneered in 1996 by Slonczewski [5] and Berger [6], who introduced the concept of the spin transfer torque [7], according to which a spin polarized current, emitted from a ferromagnetic layer which acts as the polarizer, causes a precession of the magnetization of a second ferromagnetic layer. This effect can be used for an electric-field control of Magnetoresistive Random-Access Memories (MRAMs) [8], interpreting the "up" or "down" direction of

magnetization as the logical states of a magnetic memory bit and accordingly writing the magnetic information. In the last few years, another type of current-induced spin torque, the spin-orbit torque (SOT) [9–11], has gained ground. Its main advantage is that the charge current is converted to a spin current without the need of a ferromagnetic polarizer. The SOT effect has been investigated mainly in ferromagnetic bilayers or multilayers theoretically [12–17] and experimentally [18–20].

A prerequisite for the accumulation of spin, and therefore for the appearance of the spin-orbit torque, is a strong spin-orbit coupling [21] in the material. This property is shared by a special class of materials, the topological insulators [22–25] that are narrow-gap semiconductors in the bulk but possess metallic surface states. The strong spin-orbit coupling contributes to a topological protection of these surface states against surface distortions and gives them a special spin texture, locked to the crystal momentum, with absent spin degeneracy. Due to the spin momentum locking, electrons with opposite group velocities have opposite spin directions, resulting in permanent and dissipationless spin currents on their surface. Consequently, the topological insulators display unique and advantageous properties for spin-transport applications [26–30].

A SOT effect has been observed in topological insulators bulk-doped with magnetic transition-metal impurities [31]. Also, (topological insulator)/(ferromagnet) bilayers show a strong SOT [32–35]. The latter case is difficult to analyze in realistic systems, because of the complexity of the ferromagnet's *d*-bands, as they hybridize with the topological insulator surface state. On the other hand, ferromagnetically coupled impurities on topological insulator surfaces affect the surface state only minimally and can be understood in relatively simpler terms.

Motivated by the latter realization, the present Thesis explores the phenomenon of the SOT on the magnetization of ferromagnetically ordered transition metal impurities (Cr, Mn, Fe and Co) embedded in the surface of the topological insulator Bi_2Te_3 [36, 37]. In these systems the SOT generates the precession of the impurity magnetic moments in response to an electrical current in the surface generated by an external electric field. The precession results from the transfer of spin angular momentum from current-carrying conduction electrons to the magnetic atoms during scattering between surface states of different crystal momentum and consequently different spin polarization. The strong topological insulator Bi_2Te_3 is chosen as the substrate, since it is one of the most studied topological insulators. Its simple surface band structure consists of a single Dirac cone which extends well into the bulk band gap in the vicinity of the Γ point [38], building a simple hexagonal snowflake-shaped [39] Fermi surface. Due to the metallic surface states and the insulating bulk of the topological insulator, all current flows near the surface, where the SOT effect takes place, suggesting optimal efficiency. The magnetization of the impurity atoms is directed perpendicular to the surface plane, while the spin polarization of Fermi surface states is mainly directed in the surface plane, reinforcing the SOT.

A conceptual advancement of non-volatile memory was the magnetic racetrack memory, proposed by S. Parkin [40]. In the racetrack memory, the well-known magnetic domains and domain walls are utilized as carriers of information for storing data. Following developments of the past few years that discovered the magnetic skyrmions as new types of magnetic states, a design of skyrmion-based racetrack memories was conceived [41].

Magnetic skyrmions are topological entities formed by the magnetization and confined in space. On a microscopic level, they are the result of the spin-orbit coupling of conduction electrons together with space inversion asymmetry, which promote isotropic (Heisenberg) and anisotropic (Dzyaloshinskii-Moriya) exchange interactions. In the racetrack memory based on a sequence of individual magnetic skyrmions, the data bits are encoded by the presence or absence of skyrmions, or by the presence of skyrmions of positive or negative topological charge.

Magnetic skyrmions are very promising for spintronics applications due to the experimentally and theoretically demonstrated ability to create them, drive them by means of an electric current on the surface, and detect them [42]. A skyrmion is analogous to a domain wall, however its advantages over a domain wall makes it prominent for future applications. One of the most important properties of skyrmions is their topological protection, i.e., they cannot be continuously deformed into another spin configuration, without overcoming an energy barrier [43]. Hence, magnetic skyrmions can be stabilized at the nanoscale. In addition, skyrmions are characterized by chirality, i.e., the magnetization has a unique rotational sense, defined by the microscopic properties of the material. Moreover, a skyrmion is localized in space and can be moved as a particle, but its size can be controlled by means of external magnetic fields or by alloying the material, changing the stength of the interactions. An additional crucial property of magnetic skyrmions is that they have been observed experimentally even at room temperature. Magnetic skyrmions are also very appealing for applications due to the low energy consumption required for their motion, as they can be created and be moved with low current densities [44, 45].

A vital issue that have to be addressed in the context of future applications with skyrmions is an efficient way of detection. Skyrmions in the nanoscale can be detected by means of spin-polarized scanning tunneling microscopy [46, 47], which, however, may not be ideal for applications. An auspicious phenomenon for electrically detecting magnetic skyrmions is the topological Hall effect [48–55]. This effect, caused by the spin chirality of skyrmions, is an additional contribution to the anomalous Hall effect (AHE) [56] and ordinary Hall effect (OHE). The skyrmion detection is pivotal for any spintronic device based on magnetic skyrmions, but as has been already mentioned, may additionally provide a way of readout of the logical state of the racetrack memory [42].

In this work, we consider the THE caused by stabilized magnetic skyrmions in the Fe atomic layer of the heterostructure Pd/Fe/Ir(111) (one atomic layer of Fe on the face-centered-cubic Ir(111) surface, capped by one atomic layer of Pd). Here, the Fe layer is ferromagnetic, the Ir substrate provides the strong spin-orbit coupling necessary for the anisotropic exchange, and the Pd capping enhances the ferromagnetic exchange interaction, enlarging the skyrmion. Magnetic skyrmions of a few-nm size have been already detected in this system by means of spin-polarized scanning tunneling microscopy (STM) experiments [46]. The system has also been investigated in DFT simulations [57, 58] with respect to its energetic stability. However, to the best of our knowledge, first-principles calculations have not been performed with respect to the transport properties of this system, which is the main target here.

Our ab-initio simulations are based on the Korringa-Kohn-Rostoker (KKR) Green

function method and transport theory within the Boltzmann formalism. Within this Thesis, we go beyond previous studies, as the spin-orbit torque on defects in topological surface states and the Hall effect caused by magnetic skyrmions are calculated for first time on a density-functional theory level, allowing for predictions without adjustable parameters. Moreover, both studied systems have been experimentally established, hence this Thesis is exploring the transport properties of realistic materials. Therefore, this work provides a realistic study with respect to detailed properties of materials.

This Thesis is structured as follows:

Chapter 2 presents the basic theoretical background. At first, a short introduction to density functional theory (DFT) and to Green functions for the electronic structure in Solid State Physics is given. It is followed by the presentation of the Korringa-Kohn-Rostoker Green function (KKR) formalism as a DFT method within the framework of multiple scattering theory. The application of KKR method to the calculations of impurity scattering in an otherwise periodic crystal is discussed in the end of the chapter.

Chapter 3 gives a description of the spin-transport theory, employing the Boltzmann formalism combined with the KKR method. Our investigations for the scattering properties off defects under non-equilibrium conditions, considering the application of external electric field in the system, are based on this method. The chapter closes with the equation for the calculation of the conductivity tensor which allows us to obtain some of the main results of this study.

Chapter 4 starts with an introduction to the phenomenon of the spin-orbit torque. Then, the formalism for the calculation of the matrix elements of the spin accumulation, spin-orbit torque and spin flux operators within the framework of the KKR method is presented. Afterwards, the basic equations are derived for the calculation of the linear response coefficients of the spin accumulation, spin-orbit torque and spin flux in an applied electric field, employing the multiple scattering approach, as implemented in the KKR Green function method combined with Boltzmann transport equation.

Chapter 5 focuses on the spin-orbit torque exerted on magnetic moments of magnetic transition-metal impurity atoms Cr, Mn, Fe, and Co, mediated by the topological surface state electrons of Bi_2Te_3, in response to an electric field and an electric current in the system surface. At first, a brief survey of the properties of the topological insulators, as well as their special characteristics with respect to the present Thesis, are given. Next, after the study of the electronic structure of the host system, a Bi_2Te_3 film, we provide a description of the studied system, magnetic impurity atoms embedded in the Bi_2Te_3 film surface, where spin-transport phenomena are investigated. The validity of the independent impurity scattering approximation which is conventionally used for the solution of the Boltzmann transport equation is critically examined and found inadequate in the present system. Because of this, in the calculations, a collection of magnetic impurity atoms randomly placed in the surface is taken as a large defect, including all multiple scattering events off the collection of impurities summed to all orders. The scattering rate thus calculated is used in the Boltzmann equation. In this way, a modification to the usual assumptions for the Boltzmann equation is applied. Finally, results on the response

coefficients of the spin accumulation, spin-orbit torque and spin flux in an electric field, and their correlation are presented and discussed. In addition, the resistivity due to the different impurity types systems and the relation of the torque to the Joule heat production are included in the study.

In Chapter 6, our attention shifts to the ab-initio simulation of stable single magnetic skyrmions in the ferromagnetic Fe layer of the Pd/Fe/Ir(111) heterostructure, employing the KKR Green function method. Initially, the theoretical background of the topological nature of magnetic skyrmions is introduced. Afterwards, a description of the studied system, in which the stable magnetic skyrmions are formed, is provided. Here, the skyrmions are created in the ferromagnetic Fe layer deposited on the heavy metal Ir, characterized by a strong spin-orbit interaction. Additionally, the Fermi surface of this system is studied, where spin-transport phenomena are investigated in the next chapter. We finally present three differently sized skyrmions, which are calculated in Pd/Fe/Ir(111) heterostructure.

Chapter 7 proceeds to the investigation of the topological Hall effect induced by the stable magnetic skyrmions in the Pd/Fe/Ir(111) film. Firstly, an introduction to the topological Hall effect is given. Next, the results of ab-initio calculations on spin-transport phenomena on magnetic skyrmions are presented, based on the KKR Green function method and the Boltzmann transport equation. The Chapter closes with the investigation of the dependence of the topological Hall angle on disorder.

Finally, in Chapter 8 the main conclusions of the Thesis are summarized.

2 The KKR Green function method

2.1 Density functional theory

One of the main issues in solid state physics, for the description of the electronic structure of materials, is the solution of the many-electron time-independent Schrödinger equation

$$\hat{H}\psi_0(\boldsymbol{r}_1, \boldsymbol{r}_2, \ldots, \boldsymbol{r}_N) = E_0\psi_0(\boldsymbol{r}_1, \boldsymbol{r}_2, \ldots, \boldsymbol{r}_N), \tag{2.1}$$

which describes a system of N interacting electrons in an external potential. The Hamiltonian $\hat{H}$ determines the many-body wavefunction $\psi_0(\boldsymbol{r}_1, \boldsymbol{r}_2, \ldots, \boldsymbol{r}_N)$ with eigenvalue the ground state energy E_0, as we are interested in the ground state properties of the system. The Hamiltonian consists of the kinetic energy of the electrons $\hat{T}$, the electron-electron interaction energy $\hat{U}$, and an external potential $\hat{V}_{\text{ext}}$ due to the interaction of the electrons with the atomic nuclei and applied external fields.

$$\begin{aligned}\hat{H} &= \hat{T} + \hat{U} + \hat{V}_{\text{ext}} \\ &= -\sum_{i=1}^{N} \nabla_i^2 + \sum_{i,j;i\neq j} \frac{1}{|\boldsymbol{r}_i - \boldsymbol{r}_j|} + \sum_{i=1}^{N} \hat{V}_{\text{ext}}(\boldsymbol{r}_i).\end{aligned} \tag{2.2}$$

In this formula, the Rydberg atomic units $\hbar = 2m_e = e^2/2 = 1$ with $\hbar$ the Planck constant, m_e the mass of the electron and e its charge, have been used.

The solution of the many-electron Schrödinger equation cannot be obtained with methods which are based on the calculation of the many-body wave function, since it is a function of $3N$ spatial variables. Because of this, a huge computational effort is required for the applications in realistic systems, which makes this task virtually impossible even on modern supercomputers [1].

A powerful tool for the efficient solution of this problem is an alternative method, the density functional theory (DFT) method, in which the system properties on the ground state are determined by the electron density $n_0(\boldsymbol{r})$, instead of using the wavefunction. In this way, the many-electron problem is converted to a single-electron problem, that requires a much smaller numerical effort to be solved. DFT was founded by Hohenberg-Kohn theorem [59] who showed that (a) *The energy of the ground state of an interacting many-electrons system is a unique functional of the electron density* $E_0 = E[n_0]$ and (b) *the total energy functional takes its lowest value for the ground state density.* However, the explicit form of this energy functional remains unknown.

A way of determining the ground state density $n(\boldsymbol{r})$ that was suggested by Kohn and Sham [60], is to consider a fictitious auxiliary system of non-interacting electrons with density equal to the interacting electron system. The many-body wavefunction of the auxiliary system is constructed by a set of single-electron orbitals $\phi_i(\boldsymbol{r})$ (the so-called Kohn-Sham orbitals). The orbitals obey the single-particle Kohn–Sham equation, the non-interacting Schrödinger-like equation of the auxiliary system, defined by an effective potential V_{eff} in which the non-interacting electrons move. Making use of the Hohenberg-Kohn theorem (b) and the requirement for the number of electrons N to be conserved, the following Kohn-Sham equations are derived

$$[-\nabla^2 + V_{\text{eff}}(\boldsymbol{r})]\phi_i(\boldsymbol{r}) = \varepsilon_i\phi_i(\boldsymbol{r}), \quad \forall i \tag{2.3}$$

$$n(\boldsymbol{r}) = \sum_{i=1}^{N} |\phi_i(\boldsymbol{r})|^2, \tag{2.4}$$

where V_{eff} is a functional of the density n and the summation runs over the lowest single-electron energy levels.

The effective potential (or Kohn-Sham potential) is expressed in terms of the external potential V_{ext}, the Hartree part of the electron-electron interaction and the so-called exchange-correlation potential V_{xc}

$$V_{\text{eff}}(\boldsymbol{r}) = V_{\text{ext}}(\boldsymbol{r}) + \int d\boldsymbol{r}' \frac{2n(\boldsymbol{r}')}{|\boldsymbol{r} - \boldsymbol{r}'|} + V_{\text{xc}}(\boldsymbol{r}). \tag{2.5}$$

The first two terms in Eq. (2.5) are treated exactly, while the exchange-correlation potential, which is a functional derivative of the exchange-correlation energy functional and depends on the electron density, defined as $V_{\text{xc}}(\boldsymbol{r}) = \delta E_{\text{xc}}[n]/\delta n(\boldsymbol{r})$, is the only

[1] We mention the simple example of an Fe atom with atomic charge $Z = 26$: The determination of its wavefunction solving the Eq. (2.1) on real-space grid with just 10 grid-points per dimension demands the storing of $10^{3N} = 10^{78}$ numbers, which is of the order of the total number of atoms in the universe.

unknown contribution. However, several reasonable approximations for the practical solution of the Kohn-Sham equation, in order to estimate the exchange-correlation potential have been used, such as the local density approximation (LDA) or the generalized gradient approximation (GGA) [61].

The first idea for the determination of the exchange-correlation potential is based on the homogeneous electron gas (HEG), in which the exchange-correlation energy $\varepsilon_{\mathrm{xc}}$ can be calculated accurately. Afterwards, within the LDA, the exchange-correlation energy $E_{\mathrm{xc}}^{\mathrm{LDA}}$ of an inhomogeneous electron gas with density $n(\boldsymbol{r})$, is given considering the contribution of each point $\boldsymbol{r}$ of an HEG with constant density equal to the local density $n(\boldsymbol{r})$

$$E_{\mathrm{xc}}^{\mathrm{LDA}} = \int d\boldsymbol{r}\; n(\boldsymbol{r})\varepsilon_{\mathrm{xc}}(n(\boldsymbol{r})). \tag{2.6}$$

Even if the LDA is expected to be valid for systems with densities that vary slowly in space, it is proved that in practice it provides accurate results for inhomogeneous systems, too [62]. In the calculations of this thesis, the LDA with a parametrization of Vosko, Wilk and Nusair [63] was employed.

In order to describe spin-polarized systems, i.e. systems with external magnetic fields or spin-orbit coupling, the spin-density functional theory need to be used. In this theory, apart from the ground state electron density $n_0(\boldsymbol{r})$, another basic variable is the vector of the spin density $\boldsymbol{m}_0(\boldsymbol{r})$

$$n_0(\boldsymbol{r}) = \sum_{i=1}^{N} \underline{\phi}_i^{\dagger}(\boldsymbol{r})\mathbb{1}_2\underline{\phi}_i(\boldsymbol{r}), \quad \boldsymbol{m}_0(\boldsymbol{r}) = \sum_{i=1}^{N} \underline{\phi}_i^{\dagger}(\boldsymbol{r})\boldsymbol{\sigma}\underline{\phi}_i(\boldsymbol{r}). \tag{2.7}$$

Within the Kohn-Sham formalism which has been extended to take into account the spin degree of freedom [64], the single-particle wavefunction is given by spinors

$$\underline{\phi}_i(\boldsymbol{r}) = \sum_{\sigma=\uparrow,\downarrow} \phi_i^{\sigma}(\boldsymbol{r})\underline{\chi}^{\sigma} = \begin{pmatrix} \phi_i^{\uparrow}(\boldsymbol{r}) \\ \phi_i^{\downarrow}(\boldsymbol{r}) \end{pmatrix}, \tag{2.8}$$

as the basis vectors in spin space correspond to the (2×1)-vectors, $\underline{\chi}^{\uparrow}$ for spin-up and $\underline{\chi}^{\downarrow}$ for spin-down

$$\underline{\chi}^{\uparrow} = \begin{pmatrix} 1 \\ 0 \end{pmatrix}, \quad \underline{\chi}^{\downarrow} = \begin{pmatrix} 0 \\ 1 \end{pmatrix}. \tag{2.9}$$

In the above equation (2.7), the symbol $\boldsymbol{\sigma}$ denotes the Pauli vector $\boldsymbol{\sigma} = (\sigma_x, \sigma_y, \sigma_z)$, consisting of the Pauli matrices

$$\sigma_x = \begin{pmatrix} 0 & 1 \\ 1 & 0 \end{pmatrix}, \quad \sigma_y = \begin{pmatrix} 0 & -i \\ i & 0 \end{pmatrix}, \quad \sigma_z = \begin{pmatrix} 1 & 0 \\ 0 & -1 \end{pmatrix}. \tag{2.10}$$

Here, the exchange-correlation energy is a functional of the electron density, as well as the spin density, $E_{\mathrm{xc}} = E_{\mathrm{xc}}[n, \boldsymbol{m}]$. The Kohn-Sham equation takes the following extended form

$$\Big[\big(-\nabla^2 + V_{\mathrm{eff}}(\boldsymbol{r})\big)\mathbb{1}_2 + \boldsymbol{B}^{\mathrm{xc}}(\boldsymbol{r}) \cdot \boldsymbol{\sigma}\Big]\; \underline{\phi}_i(\boldsymbol{r}) = \varepsilon_i \underline{\phi}_i(\boldsymbol{r}), \tag{2.11}$$

including the exchange-correlation magnetic field $\boldsymbol{B}^{\mathrm{xc}}(\boldsymbol{r})$. This magnetic field is a functional of n_0 and $\boldsymbol{m}_0$, defined as

$$\boldsymbol{B}^{\mathrm{xc}}(\boldsymbol{r}) = \left.\frac{\delta E_{\mathrm{xc}}[n, \boldsymbol{m}]}{\delta \boldsymbol{m}(\boldsymbol{r})}\right|_{n_0, \boldsymbol{m}_0}. \tag{2.12}$$

The $\boldsymbol{B}^{\mathrm{xc}}(\boldsymbol{r})$ can be determined by approximations in order to solve the spin-polarized Kohn-Sham equation, such as the local spin density approximation (LSDA).

2.2 Green functions in non-interacting electron systems

We consider a system of non-interacting electrons which is described by the Kohn-Sham equations (2.3). The Green function is defined as the resolvent of this equation, via the operator equation

$$(E - H)G(E) = \mathbb{1}. \tag{2.13}$$

Therefore, the Green function can be written as the inverse of the operator $G(E) = (E + i\eta - H)^{-1}$, with η a positive infinitesimal real number ($\eta \to 0^+$). In terms of eigenfunctions of H, $|\phi_i\rangle$, which obey the eigenvalue relation $H|\phi_i\rangle = \epsilon_i |\phi_i\rangle$, $G(E)$ can be obtained in the spectral representation of the Green function in real space as follows

$$G(\boldsymbol{r}, \boldsymbol{r'}; E) = \langle \boldsymbol{r}| G(E) |\boldsymbol{r}'\rangle = \sum_i \frac{\underline{\phi}_i(\boldsymbol{r})\underline{\phi}_i^{\dagger}(\boldsymbol{r}')}{E - \epsilon_i + i\eta}, \tag{2.14}$$

representing, in the limit of $\eta \to 0^+$, the propagation of an outgoing wave at $\boldsymbol{r}$ caused by a source term at position $\boldsymbol{r'}$. For spin-polarized systems the Green function is a matrix in spin space, defined as

$$G(\boldsymbol{r}, \boldsymbol{r}', E) = \begin{pmatrix} G^{\uparrow\uparrow}(\boldsymbol{r}, \boldsymbol{r}', E) & G^{\downarrow\uparrow}(\boldsymbol{r}, \boldsymbol{r}', E) \\ G^{\uparrow\downarrow}(\boldsymbol{r}, \boldsymbol{r}', E) & G^{\downarrow\downarrow}(\boldsymbol{r}, \boldsymbol{r}', E) \end{pmatrix}. \tag{2.15}$$

Using the Dirac identity it is easily proven that the spectrally- and space-resolved density of states $n(\boldsymbol{r}, E)$ can be found in terms of the Green function

$$n(\boldsymbol{r}; E) = -\frac{1}{\pi}\mathrm{Im}\mathrm{Tr}[G(\boldsymbol{r}, \boldsymbol{r}, E)]. \tag{2.16}$$

It can be shown that the expectation value A of any observable quantity, represented by an operator $\hat{A}$, is related to the Green function according to the expression

$$A = \left\langle \hat{A} \right\rangle = -\frac{1}{\pi}\mathrm{Im}\int_{-\infty}^{E_{\mathrm{F}}} dE\ \mathrm{Tr}[\hat{A}G(E)], \tag{2.17}$$

with E_{F} the Fermi energy of the system. Hence, the electron density $\rho(\boldsymbol{r})$ can be found as an integral over the energies up to Fermi level

$$\rho(\boldsymbol{r}) = -\frac{1}{\pi}\mathrm{Im}\int_{-\infty}^{E_{\mathrm{F}}} dE\ \mathrm{Tr}[G(\boldsymbol{r}, \boldsymbol{r}, E)], \tag{2.18}$$

and the spin magnetization density $\boldsymbol{m}(\boldsymbol{r})$ can be computed respectively to the electron density (Eq. eq2.18)

$$\boldsymbol{m}(\boldsymbol{r}) = -\frac{1}{\pi}\mathrm{Im}\int_{-\infty}^{E_\mathrm{F}} dE\ \mathrm{Tr}[\boldsymbol{\sigma}G(\boldsymbol{r},\boldsymbol{r},E)]. \tag{2.19}$$

Importantly, the Green function method is a powerful tool for the calculation of the electronic structure perturbed systems, such as systems of defects embedded in periodic crystals.

Relations between perturbed and unperturbed system

A perturbed system is described by the Hamiltonian $H = H_0 + \Delta V$, with ΔV the perturbing potential. The Hamiltonian obeys the Schrödinger equation $(H_0 + \Delta V)\,|\psi\rangle = E\,|\psi\rangle$, while the first part of the Hamiltonian, H_0, obeys the Schrödinger equation for a reference, unperturbed system $H_0\,|\psi_0\rangle = E\,|\psi_0\rangle$, which is known. The eigenfunctions of the perturbed system are connected to the eigenfunctions of the unperturbed by the Lippmann-Schwinger equation [65, 66]

$$|\psi\rangle = |\psi_0\rangle + G_0\,\Delta V\,|\psi\rangle\,. \tag{2.20}$$

According to the definition of the Green function (2.13), we can find a relation between the Green function of interest G and the Green function of the reference system G_0, the so-called Dyson equation [65, 67]

$$\begin{aligned} G &= G_0 + G_0\,\Delta V G && (2.21)\\ &= G_0 + G_0\,\Delta V G_0 + G_0\,\Delta V G_0\,\Delta V G_0 + \cdots && (2.22)\\ &= G_0 + G_0 \mathcal{T} G_0. && (2.23) \end{aligned}$$

The middle line (2.22) is an expression analogous of a Born series expansion for the Green function, which is helpful for the calculation of G in case of a weak perturbation ΔV, as it can be solved repetitively. In the last line (2.23), the transition matrix, or $\mathcal{T}$-matrix is introduced, which is defined by the following relation

$$\Delta V\,|\psi\rangle = \mathcal{T}(E)\,|\psi_0\rangle\,. \tag{2.24}$$

The $\mathcal{T}$-matrix [68] is a fundamental quantity of the scattering theory, since it contains the properties of scattering off a defect. If the Dyson equation is solved, it can be also found, as it can be written in terms of the Green function as follows

$$\begin{aligned} \mathcal{T} &= \Delta V + \Delta V G\,\Delta V && (2.25)\\ &= \Delta V + \Delta V G_0\,\Delta V + \Delta V G_0\,\Delta V G_0\,\Delta V + \cdots && (2.26)\\ &= \Delta V + \Delta V G_0 \mathcal{T}. && (2.27) \end{aligned}$$

2.3 Green function within the KKR formalism

2.3.1 Single-site scattering theory

In a first step, the KKR formalism is applied in order to deal the scattering problem of a finite range potential off a single atom embedded into a reference system, which is chosen as the free space.

Green function of free space

The reference system is considered a free-electron system, of which the solutions are analytically known. The Hamiltonian contains only the kinetic energy term, i.e. $V(\boldsymbol{r}) = 0$, and the eigenfunctions $\varphi_{\boldsymbol{k}}(\boldsymbol{r})$ are just plain waves which are expanded in real spherical harmonics basis $Y_L(\hat{r})$

$$\varphi_{\boldsymbol{k}}(\boldsymbol{r}) = e^{i\boldsymbol{k}\boldsymbol{r}} \tag{2.28}$$

$$= \sum_L 4\pi i^l j_l(\sqrt{E}r) Y_L(\hat{r}) Y_L(\hat{k}), \tag{2.29}$$

with $k = |\boldsymbol{k}| = \sqrt{E}$, $r = |\boldsymbol{r}|$, and j_l denotes the spherical Bessel functions of the first kind. Here, the combined index $L = \{l, m\}$ of the angular momentum indexes l and m is used.

The Green function of a free-electron system is given as [65]:

$$g(\boldsymbol{r}, \boldsymbol{r'}; E) = -\frac{1}{4\pi} \frac{e^{i\sqrt{E}|\boldsymbol{r}-\boldsymbol{r'}|}}{|\boldsymbol{r}-\boldsymbol{r'}|} \tag{2.30}$$

$$= \sum_L \frac{1}{rr'} Y_L(\hat{r}) g_l(r, r'; E) Y_L(\hat{r'}), \tag{2.31}$$

where the expansion coefficients of the Green function g_l are introduced, which are defined as

$$g_l(r, r'; E) = \sqrt{E}\ rr' j_l(\sqrt{E}r_<) h_l(\sqrt{E}r_>). \tag{2.32}$$

$h_l(r)$ are the spherical Hankel functions [2], and $r_{<(>)}$ is the smaller (larger) of the radius r and r', respectively. The Bessel functions j_l are finite as $r \to 0$, while the Hankel diverge. Making use of the abbreviations $J_L(r; E) = r j_l(\sqrt{E}r)$ and $H_L(r; E) = r h_l(\sqrt{E}r)$ the expansion coefficients are expressed in the form

$$g_l(r, r'; E) = \sqrt{E}\ [J_L(r; E) H_L(r'; E)\theta(r' - r) + H_L(r; E) J_L(r'; E)\theta(r - r')], \tag{2.33}$$

with θ the Heaviside step function.[3]

[2] The spherical Hankel functions are defined as $h_l = n_l - i j_l$, and n_l are the Neumann functions.

[3] $\theta(x) = \begin{pmatrix} 0; & x < 0 \\ 1; & x \geq 0 \end{pmatrix}$

Green function of an atomic potential

Next, we want to solve the scattering problem of a perturbed potential $V(\boldsymbol{r})$ of finite range embedded in free space. Then, the wavefunctions $\psi_{\boldsymbol{k}}(\boldsymbol{r})$ can be found in terms of the Green function of the free space g, using the Lippmann-Schwinger equation (2.20)

$$\psi_{\boldsymbol{k}}(\boldsymbol{r}) = e^{i\boldsymbol{k}\boldsymbol{r}} + \int d\boldsymbol{r'} g(\boldsymbol{r}, \boldsymbol{r'}; E) V(\boldsymbol{r'}) \psi_{\boldsymbol{k}}(\boldsymbol{r'}), \tag{2.34}$$

with $E = k^2$, the energy of a free particle of wave vector $\boldsymbol{k}$. The first term represents an incoming plane wave, while the second term determines the scattered wave. The wavefunctions are expanded in real spherical harmonics basis, similarly to Eq. (2.31)

$$\psi_{\boldsymbol{k}}(\boldsymbol{r}) = \sum_L 4\pi i^l R_L(\boldsymbol{r}; E) Y_L(\hat{k}), \tag{2.35}$$

with $R_L(\boldsymbol{r}; E)$ the regular solutions, given by the following expansion in real spherical harmonics

$$R_L(\boldsymbol{r}; E) = \sum_{L'} \frac{1}{r} R_{L'L}(r; E) Y_{L'}(\hat{r}). \tag{2.36}$$

The Green function of this single scattering problem G_S is found in terms of the right-hand regular $R_L(\boldsymbol{r})$ and irregular $S_L(\boldsymbol{r})$ solutions, and the corresponding left-hand side solutions, $\bar{R}_L(\boldsymbol{r})$ and $\bar{S}_L(\boldsymbol{r})$[4]

$$G_S(\boldsymbol{r}, \boldsymbol{r'}; E) = \sqrt{E} \sum_L [\theta(r' - r) R_L(\boldsymbol{r}) \bar{S}_L(\boldsymbol{r'}) + \theta(r - r') S_L(\boldsymbol{r}) \bar{R}_L(\boldsymbol{r'})]. \tag{2.37}$$

The regular and irregular solutions are expanded in real spherical harmonics similarly as (2.36) [69], and its expansion coefficients $R_{L'L}$, $S_{L'L}$ of the right scattering wavefunctions are given by the following Lippmann-Schwinger equations [69]

$$R_{L'L}(r; E) = J_L(r; E)\delta_{L'L} + \sum_{L''} \int dr'' g_{l'}(r, r''; E) V_{L'L''}(r'') R_{L''L}(r''; E) \tag{2.38}$$

$$S_{L'L}(r; E) = H_L(r; E)\beta_{L'L}(E) + \sum_{L''} \int dr'' g_{l'}(r, r''; E) V_{L'L''}(r'') S_{L''L}(r''; E), \tag{2.39}$$

where $V_{L'L''}$ is the expansion coefficient in real spherical harmonics of the atomic potential and β matrix is found by the expression

$$\beta_{L'L}(E) = \delta_{L'L} - \sqrt{E} \int dr' \bar{J}_L(r'; E) \sum_{L''} V_{L'L''}(r') S_{L''L}(r'; E). \tag{2.40}$$

[4] The right-hand solutions, regular $R_L(\boldsymbol{r})$ and irregular $S_L(\boldsymbol{r})$, are 2×1 spinors (column-vectors) in Pauli theory, and the left-hand side solutions, regular and irregular, $\bar{R}_L(\boldsymbol{r})$ and $\bar{S}_L(\boldsymbol{r})$, are 1×2 spinors (row-vectors).

The corresponding expansion coefficients of regular and irregular left scattering wavefunctions $\bar{R}_{LL'}$, are derived by the following Lippmann-Schwinger relations

$$\bar{R}_{LL'}(r;E) = \bar{J}_{L'}(r;E)\delta_{LL'} + \sum_{L''}\int dr''\bar{R}_{LL''}(r'';E)V_{L''L'}(r'')g_{l'}(r'',r;E) \tag{2.41}$$

$$\bar{S}_{LL'}(r;E) = \bar{\beta}_{LL'}(E)\bar{H}_{L'}(r;E) + \sum_{L''}\int dr''\bar{S}_{L''L}(r'';E)V_{L'L''}(r'')g_{l'}(r'',r;E), \tag{2.42}$$

with $\bar{\beta}$ matrix:

$$\bar{\beta}_{LL'}(E) = \delta_{LL'} - \sqrt{E}\int dr'\bar{S}_{LL''}(r';E)\sum_{L''}V_{L''L'}(r')J_{L'}(r';E). \tag{2.43}$$

For a detailed analysis we refer to the work of Bauer [69].

Atomic transition matrix (t-matrix)

As the regular scattering solutions of the reference system into free space are estimated, the atomic transition matrix (t-matrix) is found by the integral

$$t_{LL'}(E) = \sum_{L''}\int_0^{R_{\max}} dr\bar{J}_L(r;E)V_{LL''}(r)R_{L''L'}(r;E), \tag{2.44}$$

with $R_{\max}$ the radius of the atomic sphere. Here, the t-matrix gives the scattering properties of the single atomic potential, but its calculation is important for the treatment of the multiple scattering problem, combining the scattering properties of the single atoms at sites n, as it will be shown in the next step.

2.3.2 Multiple scattering theory

The single scattering theory can deal with the problem of an isolated scatterer. Now, we consider a collection of identical scatterers at lattice positions $\boldsymbol{R}_n$ $(n = 1, .., N)$, in order to take into account the scattering by all atoms within the whole crystal. The KKR Green function G that describes the multiple scattering process is a sum of two terms, the onsite term which gives the solution of the single atomic potential G_S^n (given by Eq. 2.37), and an additional term of the multiple scattering contribution, which describes the scattering between different sites $G_M^{nn'}$

$$G(\boldsymbol{r}+\boldsymbol{R}_n, \boldsymbol{r'}+\boldsymbol{R}_{n'};E) = G_S^n(\boldsymbol{r},\boldsymbol{r'};E)\delta_{nn'} + G_M^{nn'}(\boldsymbol{r},\boldsymbol{r'};E). \tag{2.45}$$

Voronoi construction

In the KKR formalism a tessellation of space in atomic cells is used. The center of each cell is the nucleus position, and the cells are found by a Voronoi construction, as

polyhedron-shaped cells. This Voronoi tessellation allows us the division of the Green function calculation into two parts, a local and a global part. Firstly, the local scattering problem in each cell is solved independently. In a second step, the multiple scattering among atoms problem is treated with the coupling of the local solutions, and the full Green function of the crystal is found.

This is achieved with the introduction of a globally vector $\boldsymbol{x}$ pointing inside a cell n, defined as

$$\boldsymbol{x} = \boldsymbol{r} + \boldsymbol{R}_n, \tag{2.46}$$

where $\boldsymbol{R}_n$ is the lattice site of each scattering center and $\boldsymbol{r}$ is locally defined inside the cell n. Then, the potential is also separated into local potentials

$$V(\boldsymbol{x}) = \sum_n V^n(\boldsymbol{x} - \boldsymbol{R}_n) = \sum_n V^n(\boldsymbol{r}), \tag{2.47}$$

with

$$V^n(\boldsymbol{r}) = \begin{cases} V(\boldsymbol{r} + \boldsymbol{R}_n), & \text{if } \boldsymbol{r} + \boldsymbol{R}_n \in \text{cell } n. \\ 0, & \text{otherwise.} \end{cases} \tag{2.48}$$

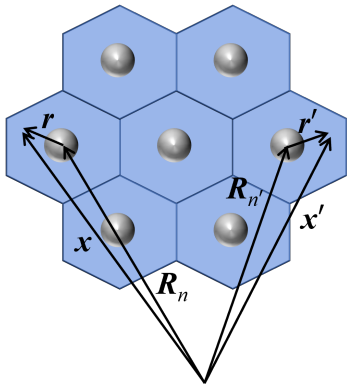

Figure 2.1: Illustration of the division of atomic cells found by the Voronoi construction. The gray spheres represent the positions of atoms in the crystal.

Green function of the free space

The Green function of the free-electron system g is decomposed by a single site part and a multiple scattering part

$$g(\boldsymbol{r}+\boldsymbol{R}_n, \boldsymbol{r'}+\boldsymbol{R}_{n'}; E) = \delta_{nn'}\sqrt{E}\sum_L j_L(\boldsymbol{r}_<; E)h_L(\boldsymbol{r}_>; E) + \sum_{LL'} j_L(\boldsymbol{r}; E)g^{nn'}_{LL'}(E)j_{L'}(\boldsymbol{r'}; E), \tag{2.49}$$

where the abbreviations $j_L(\boldsymbol{x}; E) = j_l(\sqrt{E}x)Y_L(\hat{x})$ for the Bessel function, and similarly for the Hankel function $h_L(\boldsymbol{x}; E) = h_l(\sqrt{E}x)Y_L(\hat{x})$ are used. The expansion coefficients

of the Green function $g_{LL'}^{nn'}$ which are introduced, also called structure constants, are obtained by the relation

$$g_{LL'}^{nn'} = -(1-\delta_{nn'})4\pi\sqrt{E}\sum_{L''} i^{l-l'+l''} C_{LL'L''} h_{L''}(\boldsymbol{R}_n - \boldsymbol{R}_{n'}; E), \tag{2.50}$$

with the Gaunt coefficients defined as $C_{LL'L''} = \int d\Omega\ Y_L(\hat{r})Y_{L'}(\hat{r})Y_{L''}(\hat{r})$.

Green function of atomic potential

In the presence of the periodic potential in the crystal $V(\boldsymbol{r})$, similarly to Eq. (2.49), the Green function which describes the multiple scattering problem (Eq. (2.45)), is finally written

$$G(\boldsymbol{r}+\boldsymbol{R}_n, \boldsymbol{r'}+\boldsymbol{R}_{n'}; E) = G_S(\boldsymbol{r}, \boldsymbol{r'}; E)\delta_{nn'} + \sum_{\Lambda\Lambda'} R_\Lambda(\boldsymbol{r}; E) G_{\Lambda\Lambda'}^{nn'}(E) \bar{R}_{\Lambda'}(\boldsymbol{r'}; E), \tag{2.51}$$

with $G_{\Lambda\Lambda'}^{nn'}(E)$ the expansion coefficients of the Green function, which are called structural Green functions. Here, we introduce the combined index for angular momentum and spin, $\Lambda = (L, s) = (l, m, s)$.

In addition, the Green function obeys the Dyson equation

$$\begin{aligned} G(\boldsymbol{r}+\boldsymbol{R}_n, \boldsymbol{r'}+\boldsymbol{R}_{n'}; E) &= g(\boldsymbol{r}+\boldsymbol{R}_n, \boldsymbol{r'}+\boldsymbol{R}_{n'}; E) + \\ &\sum_{n''} \int d^3r'' g(\boldsymbol{r}+\boldsymbol{R}_n, \boldsymbol{r''}+\boldsymbol{R}_{n''}; E) V_{n''}(\boldsymbol{r''}) G(\boldsymbol{r''}+\boldsymbol{R}_{n''}, \boldsymbol{r'}+\boldsymbol{R}_{n'}; E). \end{aligned} \tag{2.52}$$

Instead of solving the above normal Dyson equation (Eq. (2.52)) which includes the potential, the Green function of the multiple scattering of electrons is found according to Eq. (2.51). In this equation, the structural Green functions $G_{\Lambda\Lambda'}^{nn'}(E)$ can be determined by an algebraic Dyson equation [70]

$$G_{\Lambda\Lambda'}^{nn'}(E) = g_{\Lambda\Lambda'}^{nn'}(E) + \sum_{n''\Lambda''\Lambda'''} g_{\Lambda\Lambda''}^{nn''}(E)\ t_{\Lambda''\Lambda'''}^{n''}(E)\ G_{\Lambda'''\Lambda'}^{n''n'}(E), \tag{2.53}$$

which involves the structure constants $g_{\Lambda\Lambda''}^{nn''}(E)$ and the atomic t-matrix (Eq. (2.44)). By the expansion of the sum on the right-hand side into Born series, we can derive the physical interpretation of this equation. This describes the multiple scattering of electrons in the crystal, as shows that an electron can travel from site n' to n directly, or after multiple scattering events at one site, or two sites, etc.

The calculation of the structural Green functions is simplified in practice, solving the algebraic Dyson equation (2.53) firstly in the reciprocal space. Then, the structure constants $g_{\Lambda\Lambda''}^{\mu\mu'}(\boldsymbol{k}; E)$ and the structural Green functions $G_{\Lambda\Lambda''}^{\mu\mu'}(\boldsymbol{k}; E)$ are only dependent on the geometry of the lattice, and the relative position $\boldsymbol{R}_n - \boldsymbol{R}_{n'}$. The structural Green functions in k-space are written

$$G_{\Lambda\Lambda''}^{\mu\mu'}(\boldsymbol{k}; E) = \sum_{n'} G_{\Lambda\Lambda''}^{n\mu;n'\mu'}(E) e^{i\boldsymbol{k}\cdot(\boldsymbol{R}_n - \boldsymbol{R}_{n'})}, \tag{2.54}$$

and the structure constants of the reference system are given, respectively

$$g^{\mu\mu'}_{\Lambda\Lambda''}(\boldsymbol{k};E) = \sum_{n'} g^{n\mu;n'\mu'}_{\Lambda\Lambda''}(E) e^{i\boldsymbol{k}\cdot(\boldsymbol{R}_n - \boldsymbol{R}_{n'})}. \tag{2.55}$$

The k-dependent Dyson equation is solved by matrix inversion

$$G^{\mu\mu'}_{\Lambda\Lambda''}(\boldsymbol{k};E) = \left[\Big(1 - \boldsymbol{g}(\boldsymbol{k};E)\boldsymbol{t}(E)\Big)^{-1} \boldsymbol{g}(\boldsymbol{k};E)\right]^{\mu\mu'}_{\Lambda\Lambda'}, \tag{2.56}$$

with $G(\boldsymbol{k};E)$, $g(\boldsymbol{k};E)$, and $\boldsymbol{t}(E)$ matrices in (Λ,Λ') and (μ,μ') subspaces. An inverse Fourier transformation is used to calculate the structural Green function

$$G^{nn';\mu\mu'}_{\Lambda\Lambda''}(E) = \frac{1}{V_{\mathrm{BZ}}} \int_{\mathrm{BZ}} d\boldsymbol{k}\; G^{\mu\mu'}_{\Lambda\Lambda''}(\boldsymbol{k};E) e^{i\boldsymbol{k}\cdot(\boldsymbol{R}_n - \boldsymbol{R}_{n'})} e^{i\boldsymbol{k}\cdot(\boldsymbol{\chi}_\mu - \boldsymbol{\chi}_{\mu'})}, \tag{2.57}$$

where the integral is performed over the volume of the Brillouin zone V_{BZ}. Consequently, the full KKR Green function (2.51), including the single, as well as the multiple scattering part, can be calculated and we can proceed with the evaluation of the charge density.

Secular equation

Next, we aim to solve the eigenvalue problem of the electrons in a periodic crystal. This can be dealt by the KKR secular equation, which is solved for certain pairs of $\boldsymbol{k}$ and E, and gives the energy band structure $E(\boldsymbol{k})$ of the crystal

$$\sum_{\Lambda'\mu'} \left[\delta_{\Lambda\Lambda'}\delta_{\mu\mu'} - \sum_{\Lambda''} g^{\mu\mu'}_{\Lambda\Lambda''}(\boldsymbol{k};E) t^{\mu'}_{\Lambda''\Lambda'}(E)\right] c^{\mu'}_{\boldsymbol{k}\Lambda'} = 0, \tag{2.58}$$

which is also expressed as

$$\det\Big(\delta_{\Lambda\Lambda'} - \sum_{\Lambda''} g^{\mu\mu'}_{\Lambda\Lambda''}(\boldsymbol{k};E) t^{\mu'}_{\Lambda''\Lambda'}(E)\Big) = 0. \tag{2.59}$$

Thus, the band structure $E(\boldsymbol{k})$ is determined by scanning all energies for a given path of $\boldsymbol{k}$ in the Brillouin zone.

The knowledge of the coefficient vector $c^{\mu}_{\boldsymbol{k}\Lambda}$ is important for the determination of the Bloch wavefunctions $\psi_{\boldsymbol{k}}$ in the crystal, in terms of the regular scattering solutions $R^{\mu}_{\Lambda}(\boldsymbol{r};E)$ (Eq. (2.36))

$$\psi_{\boldsymbol{k}}(\boldsymbol{r} + \boldsymbol{R}_n + \boldsymbol{\chi}_\mu) = \sum_{\Lambda} c^{\mu}_{\boldsymbol{k}\Lambda} R^{\mu}_{\Lambda}(\boldsymbol{r};E) e^{i\boldsymbol{k}\cdot\boldsymbol{R}_n}. \tag{2.60}$$

The numerical solution of the secular equation is carried out considering the eigenvalue problem

$$\boldsymbol{M}(\boldsymbol{k};E)\boldsymbol{c}_\nu = \lambda_\nu \boldsymbol{c}_\nu, \tag{2.61}$$

where the matrix $\boldsymbol{M}(\boldsymbol{k};E)$, also called *KKR matrix*, represents the term inside the brackets of Eq. (2.58). The problem is solved for the eigenvalues which satisfy the condition $\lambda_\nu = 0$.

In this way, apart from the band structure, we can determine the Fermi surface of a system. This is achieved setting the energy fixed to the Fermi energy, $E = E_{\mathrm{F}}$, and scanning the k-space.

2.3.3 Spin-orbit interaction

The spin-orbit interaction (or spin-orbit coupling) comprises the coupling of the spin degree of freedom $\boldsymbol{\sigma}$ of an electron to its orbital angular momentum $\boldsymbol{L}$ and can be described by the following Hamiltonian for spherically symmetric potentials

$$\hat{H}_{\mathrm{SO}} = \frac{1}{M(r)^2\ c^2}\frac{1}{r}\frac{\partial V(r)}{\partial r}\boldsymbol{L}\cdot\boldsymbol{\sigma}, \tag{2.62}$$

where $M(r)$ is the relativistic mass and c is the speed of light. The potential $V(r)$ is chosen as the average spin-up and spin-down potential, i.e. $V(r) = \frac{(V_\uparrow + V_\downarrow)}{2}$.

The inclusion of the SOI can be achieved, considering this spin-orbit coupling Hamiltonian as an additional term to the Schrödinger equation. In this way, the total Hamiltonian is written as a 2×2 matrix in spin-space

$$\begin{pmatrix} H^{tot}_{\uparrow\uparrow} & H^{tot}_{\uparrow\downarrow} \\ H^{tot}_{\downarrow\uparrow} & H^{tot}_{\downarrow\downarrow} \end{pmatrix} = \begin{pmatrix} H_{\uparrow\uparrow} & 0 \\ 0 & H_{\downarrow\downarrow} \end{pmatrix} + \begin{pmatrix} H^{SOC}_{\uparrow\uparrow} & H^{SOC}_{\uparrow\downarrow} \\ H^{SOC}_{\downarrow\uparrow} & H^{SOC}_{\downarrow\downarrow} \end{pmatrix}. \tag{2.63}$$

Further details regarding the spin-orbit coupling within the KKR method can be found in the Theses by Heers [71] and by Bauer [69].

2.4 Impurity scattering

One of the main concepts of this thesis is the study of the electronic structure of materials in the presence of impurities. The idealized ordered periodic crystal is disturbed by the existence of impurities, as a result its periodicity is broken.

The solution of this scattering problem is carried out in two steps. At first, the electronic properties of the host system, i.e. the periodic crystal without impurities are studied, which obey the Bloch's theorem, and in a second step the scattering of Bloch electrons off impurity atoms is investigated.

The lattice site of the atoms in the impurity cluster is determined by the combined site index $i = (n, \mu)$, defining the atomic site $\boldsymbol{X}_i$ by the lattice vector $\boldsymbol{R}_n$ and the sub-lattice vector $\boldsymbol{\chi}_\mu$. Thus, the general position in the crystal is given in the form

$$\boldsymbol{x} = \boldsymbol{r} + \boldsymbol{X}_i = \boldsymbol{r} + \boldsymbol{R}_n + \boldsymbol{\chi}_\mu. \tag{2.64}$$

Impurity wavefunction

The methodology which was followed for the solution of a periodic potential embedded in free-space is used in analogy here, in order to solve the scattering problem due to the perturbing potential ΔV of the impurities into a periodic host system. The perturbing potential is defined as the difference between the impurity potential and the potential of the host system

$$\Delta V(\boldsymbol{r}) = V^{\mathrm{imp}}(\boldsymbol{r}) - V^{\mathrm{host}}(\boldsymbol{r}). \tag{2.65}$$

The impurity scattering wavefunctions $\psi_{\boldsymbol{k}}^{\mathrm{imp}}(\boldsymbol{r})$ are connected to the radial scattering solutions of the perturbed atomic potentials $R^{\mathrm{imp},i}$ with the expansion coefficients $c_{\Lambda}^{\mathrm{imp},i}$

$$\psi_{\boldsymbol{k}}^{\mathrm{imp}}(\boldsymbol{r}) = \sum_{\Lambda} c_{\Lambda}^{\mathrm{imp},i} R_{\Lambda}^{\mathrm{imp},i}(\boldsymbol{r}; E). \tag{2.66}$$

The regular scattering solutions for the single-site scattering due to the impurity potential, is given by the following Lippmann-Schwinger equation

$$R_{\Lambda}^{\mathrm{imp},i}(\boldsymbol{r}; E) = j_l(\sqrt{E}r) Y_L(\hat{r}) \chi^s + \int d\boldsymbol{r'} g(\boldsymbol{r}, \boldsymbol{r'}; E) V^{\mathrm{imp}}(\boldsymbol{r'}) R_{\Lambda}^{\mathrm{imp},i}(\boldsymbol{r'}; E), \tag{2.67}$$

where the reference system is considered as the free space, and $g(\boldsymbol{r}, \boldsymbol{r'}; E)$ is the single-site Green function of the free space. They are expanded in real spherical harmonics according to the relation

$$R_{\Lambda}^{\mathrm{imp}}(\boldsymbol{r}; E) = R_{L}^{\mathrm{imp},s}(\boldsymbol{r}; E) = \sum_{L'} \frac{1}{r} R_{L'L}^{\mathrm{imp},s'}(\boldsymbol{r}; E) Y_{L'}(\hat{r}). \tag{2.68}$$

The wavefunction of an impurity atom $\psi_{\boldsymbol{k}}^{\mathrm{imp}}(\boldsymbol{x})$, embedded in a periodic host system, are correlated to the eigenstates of the host system $\psi_{\boldsymbol{k}}(\boldsymbol{x})$ (Eq. (2.60)) via the Lippmann-Schwinger equation

$$\psi_{\boldsymbol{k}}^{\mathrm{imp}}(\boldsymbol{x}) = \psi_{\boldsymbol{k}}(\boldsymbol{x}) + \int d\boldsymbol{r'} G(\boldsymbol{x}, \boldsymbol{x'}) \Delta V(\boldsymbol{x'}) \psi_{\boldsymbol{k}}^{\mathrm{imp}}(\boldsymbol{x'}), \tag{2.69}$$

where $G(\boldsymbol{x}, \boldsymbol{x'})$ is the Green function of the host system. In practice, another form of the Lippmann-Schwinger equation is chosen

$$\psi_{\boldsymbol{k}}^{\mathrm{imp}}(\boldsymbol{x}) = \psi_{\boldsymbol{k}}(\boldsymbol{x}) + \int d\boldsymbol{r'} G^{\mathrm{imp}}(\boldsymbol{x}, \boldsymbol{x'}) \Delta V(\boldsymbol{x'}) \psi_{\boldsymbol{k}}(\boldsymbol{x'}), \tag{2.70}$$

where the impurity Green function $G^{\mathrm{imp}}(\boldsymbol{x}, \boldsymbol{x'})$ is included for the evaluation of the impurity wavefunction.

Impurity Green function

The Green function in the impurity region consists of two parts, the single-site term and the back-scattering term.

$$G^{\mathrm{imp}}(\boldsymbol{r} + \boldsymbol{X}_i, \boldsymbol{r'} + \boldsymbol{X}_{i'}) = \delta_{ii'} G_s^{\mathrm{imp},i}(\boldsymbol{r}, \boldsymbol{r'}) + \sum_{\Lambda\Lambda'} R_{\Lambda}^{\mathrm{imp},i}(\boldsymbol{r})\ G_{\Lambda\Lambda'}^{\mathrm{imp},ii'}\ \bar{R}_{\Lambda'}^{\mathrm{imp},i'}(\boldsymbol{r'}), \tag{2.71}$$

The impurity structural Green functions $G_{\Lambda\Lambda'}^{\mathrm{imp},ii'}$ are related to the structural Green functions of the host system by the algebraic Dyson equation

$$G_{\Lambda\Lambda'}^{\mathrm{imp},ii'} = G_{\Lambda\Lambda'}^{\mathrm{host},ii'} + \sum_{\Lambda''\Lambda'''} \sum_{i''} G_{\Lambda\Lambda'}^{\mathrm{host},ii'} \Delta t_{\Lambda''\Lambda'''}^{i''} G_{\Lambda'''\Lambda'}^{\mathrm{imp},i''i'}, \tag{2.72}$$

where $\Delta t^{i''}_{\Lambda''\Lambda'''} = t^{\mathrm{imp},i''}_{\Lambda''\Lambda'''} - t^{\mathrm{host},i''}_{\Lambda''\Lambda'''}$ being the difference between the t-matrix of the impurity atomic potential V^{imp} and the host potential V^{host}, computed according to Eq. (2.44).

The host structural Green function $G^{\mathrm{host},ii'}_{\Lambda\Lambda'}$ is found in reciprocal space and is transformed to the real-space impurity region by a Fourier transformation, as described in previous section, while the previous equation (2.72) for the evaluation of the impurity structural Green function $G^{\mathrm{imp},ii'}_{\Lambda\Lambda'}$, can be directly solved in real space with the following inversion matrix

$$G^{\mathrm{imp},ii'}_{\Lambda\Lambda'} = \left[1 - G^{\mathrm{host},ii'}_{\Lambda\Lambda'} \Delta t^{i''}_{\Lambda''\Lambda'''}\right]^{-1} G^{\mathrm{host},ii'}_{\Lambda\Lambda'}. \tag{2.73}$$

The knowledge of the impurity Green function allows us to calculate the impurity expansion coefficients $c^{\mathrm{imp},i}_{\Lambda}$, i.e., the impurity eigenvectors, which are given in terms of the host coefficients, i.e. of the Bloch states $c^{i'}_{\Lambda'} = c^{\mu'}_{\Lambda'} e^{i\boldsymbol{k}\cdot\boldsymbol{R}_{n'}}$, according to the relation [72]:

$$c^{\mathrm{imp},i}_{\Lambda} = \sum_{\Lambda',i'} \left\{ \delta_{\Lambda\Lambda'}\delta_{ii'} + \sum_{\Lambda''} G^{\mathrm{imp},ii'}_{\Lambda\Lambda''} \Delta t^{\mathrm{imp},i'}_{\Lambda''\Lambda'} \right\} c^{\mu'}_{\Lambda'} e^{i\boldsymbol{k}\cdot\boldsymbol{R}_{n'}}, \tag{2.74}$$

where the $\Delta t^{\mathrm{imp},i}$-matrix elements are introduced, defined by the equation

$$\Delta t^{\mathrm{imp},i}_{\Lambda\Lambda'} = \sum_{\Lambda''\Lambda'''} \int dr \bar{R}^{i}_{\Lambda\Lambda''}(r) \Delta V^{i}_{\Lambda''\Lambda'''}(\boldsymbol{r}) R^{\mathrm{imp},i}_{\Lambda'''\Lambda'}(r). \tag{2.75}$$

Scattering rate

One of the most important quantities in scattering calculations is the scattering transition rate $w_{\boldsymbol{k}\boldsymbol{k}'}$, defined as the electron scattering probability $P_{\boldsymbol{k}\boldsymbol{k}'}$ from an initial state $\psi_{\boldsymbol{k}}$ to a final state $\psi_{\boldsymbol{k}'}$, due to the presence of an impurity, per unit time:

$$w_{\boldsymbol{k}\boldsymbol{k}'} = \frac{\mathrm{d}P_{\boldsymbol{k}\boldsymbol{k}'}}{\mathrm{d}t}. \tag{2.76}$$

The knowledge of the scattering rate is a powerful tool for spin transport phenomena calculations, within the Boltzmann formalism, as will be discussed in the next Chapter. The scattering rate can be computed, expressed in terms of the T-matrix according to Fermi's Golden Rule [68]

$$w_{\boldsymbol{k}\boldsymbol{k}'} = \frac{2\pi}{\hbar} \delta(E(\boldsymbol{k}) - E(\boldsymbol{k}')) |T_{\boldsymbol{k}'\boldsymbol{k}}|^2. \tag{2.77}$$

From the δ-function inserted in the above Eq. (2.77), it is shown that the scattering rate is energy-conserving, i.e. the scattering off impurities is elastic, restricted to states with same energy. Within the Fermi surface calculations for the study of electronic transport properties that we are interested in, the energy is equal to the Fermi level energy.

The transition matrix elements are given in $\boldsymbol{k}$-space representation by the relation [73]

$$T_{\boldsymbol{k}'\boldsymbol{k}} = \int d\boldsymbol{x} \psi^{\dagger}_{\boldsymbol{k}'}(\boldsymbol{x}) \Delta V(\boldsymbol{x}) \psi^{\mathrm{imp}}_{\boldsymbol{k}}(\boldsymbol{x}), \tag{2.78}$$

where $\psi^{\mathrm{imp}}_{\boldsymbol{k}}$ is the initial state and the Bloch state $\psi^{\dagger}_{\boldsymbol{k'}}$ is the final state. Using the relations of the expansions for the host and impurity wavefunctions, according to equations (2.60) and (2.66) respectively, we derive after some algebra another form of T-matrix

$$T_{\boldsymbol{k'k}} = \sum_{\Lambda\Lambda'} \sum_{i} [c^{i}_{\boldsymbol{k'},\Lambda}]^{*} \Delta^{i}_{\Lambda\Lambda'} [c^{\mathrm{imp},i'}_{\boldsymbol{k},\Lambda'}], \tag{2.79}$$

where the Δ-matrix is entered, defined as [71]

$$\Delta^{i}_{\Lambda\Lambda'} = \sum_{\Lambda''\Lambda'''} \int d\boldsymbol{r} [R^{i}_{\Lambda\Lambda''}(r)]^{*} \Delta V^{i}_{\Lambda''\Lambda'''}(\boldsymbol{r}) R^{\mathrm{imp},i}_{\Lambda'''\Lambda'}(r). \tag{2.80}$$

Inserting the impurity expansion coefficients by Eq. (2.74) into above Eq. (2.79), the calculation of the T-matrix is simplified to the following relation

$$T_{\boldsymbol{k'k}} = \sum_{\Lambda\Lambda'} \sum_{i,i'} [c^{i}_{\boldsymbol{k'},\Lambda}]^{*} T^{i,i'}_{\Lambda\Lambda'} c^{i'}_{\boldsymbol{k},\Lambda'}, \tag{2.81}$$

where only the expansion coefficients of the Bloch states are contained. The $\{\Lambda, i\}$ representation of the T-matrix is also introduced in the previous equation, which is written as

$$T^{i,i'}_{\Lambda\Lambda'} = \sum_{\Lambda''} \Delta^{i}_{\Lambda\Lambda''} \left(\delta_{ii'} \delta_{\Lambda''\Lambda'} + \sum_{\Lambda'''} G^{\mathrm{imp},ii'}_{\Lambda''\Lambda'''} \Delta t^{\mathrm{imp},i'}_{\Lambda'''\Lambda'} \right). \tag{2.82}$$

This way of the calculation of the T-matrix is computationally very efficient, as the $\{\Lambda, i\}$ representation of the T-matrix depends only on the energy, therefore needs to be calculated only once per specific energy. Later, it can be easily used for the calculation of the T-matrix for all pairs of $\boldsymbol{k}$ and $\boldsymbol{k'}$.

3 Boltzmann formalism within KKR

A very fruitful approach for the description of transport phenomena of electrons scattered at defects in solids is the semi-classical dynamics described by the Boltzmann transport equation. Within this approach, the electron is represented as a wavepacket determined with Bloch states. The term "semi-classical" is justified, because, within the approximation, the motion of the crystal electrons between scattering events follows the classical equations, while the scattering process is described by quantum-mechanical equations.

The transport theory based on the Boltzmann formalism combined with the KKR method [72, 74] is presented in this Chapter. The KKR formalism for the calculation of Fermi surfaces, impurity scattering and spin transport using the Boltzmann equation [74], has been used in the past for problems related to the present study, e.g. for the investigation of the spin Hall [73, 75] and the spin Nerst effect [76].

3.1 Boltzmann transport equation

The electrons' motion is interrupted by collisions under the influence of external forces, that re-distribute the electrons, and the wavepacket is supposed to occupy a new state, continuing its motion until the next collision, etc. In this way, one can define the non-equilibrium distribution function $f_{n\boldsymbol{k}}(\boldsymbol{r}, t)$, which depends on the position $\boldsymbol{r}$, the crystal momentum $\boldsymbol{k}$ and the time t, and measures the probability of occupation of an

electron state in the energy band n for the crystal momentum $\boldsymbol{k}$ in the region $\boldsymbol{r}$ at time t. The Boltzmann equation describes the rate of change of the distribution function in the presence of external fields and due to electron scattering, given as

$$\frac{\partial f_{\boldsymbol{k}}}{\partial t} + \left.\frac{\partial f_{\boldsymbol{k}}}{\partial t}\right|_{\text{field}} + \left.\frac{\partial f_{\boldsymbol{k}}}{\partial t}\right|_{\text{diffusion}} = \left.\frac{\partial f_{\boldsymbol{k}}}{\partial t}\right|_{\text{sc}} \Rightarrow$$

$$\frac{\partial f_{\boldsymbol{k}}}{\partial t} + \left.\frac{\partial f_{\boldsymbol{k}}}{\partial \boldsymbol{k}}\frac{\mathrm{d}\boldsymbol{k}}{\mathrm{d}t}\right|_{\text{field}} + \left.\frac{\partial f_{\boldsymbol{k}}}{\partial \boldsymbol{r}}\frac{\mathrm{d}\boldsymbol{r}}{\mathrm{d}t}\right|_{\text{diffusion}} = \left.\frac{\partial f_{\boldsymbol{k}}}{\partial t}\right|_{\text{sc}}, \tag{3.1}$$

where the band index n, which denotes the additional degeneracy, has been dropped for simplicity. The second and third term on the left-hand side of the equation determines the change of the distribution function due to external fields and due to diffusion in $\boldsymbol{r}$, respectively. The right-hand side denotes the rate of change of $f_{\boldsymbol{k}}$ through scattering processes. We are interested in the steady state, i.e. $\frac{\partial f_{\boldsymbol{k}}}{\partial t} = 0$, and our analysis is restricted only in the influence of a homogeneous and time-independent external electric field. Thus, in Eq. (3.1) on the left-hand side, only the field term remains and the Boltzmann equation reduces to

$$\left.\frac{\partial f_{\boldsymbol{k}}}{\partial \boldsymbol{k}}\frac{\mathrm{d}\boldsymbol{k}}{\mathrm{d}t}\right|_{\text{field}} = \left.\frac{\partial f_{\boldsymbol{k}}}{\partial t}\right|_{\text{sc}}. \tag{3.2}$$

The semi-classical equations, that describe the motion of an electron in an external electric field $\boldsymbol{\mathcal{E}}$ and magnetic field $\boldsymbol{B}$, according to Ehrenfest's theory are

$$\dot{\boldsymbol{r}} = \boldsymbol{v}(\boldsymbol{k}) = \frac{1}{\hbar}\frac{\partial E(\boldsymbol{k})}{\partial \boldsymbol{k}}, \tag{3.3}$$

$$\dot{\boldsymbol{k}} = \frac{e}{\hbar}\Big(\boldsymbol{\mathcal{E}}(\boldsymbol{r},t) + \frac{1}{c_0}\boldsymbol{v}(\boldsymbol{k}) \times \boldsymbol{B}(\boldsymbol{r},t)\Big), \tag{3.4}$$

where the group velocity $\boldsymbol{v}_{\boldsymbol{k}}$ is introduced. In our study we consider only the application of an electric field $\boldsymbol{\mathcal{E}}$ in the system, as a result only the first term in Eq. (3.4) survives. Thus, replacing the time derivative of momentum $\boldsymbol{k}$, according to Eq. (3.4), in the right-hand side of Eq. (3.2), the Boltzmann equation is written

$$\frac{e}{\hbar}\frac{\partial f_{\boldsymbol{k}}}{\partial \boldsymbol{k}} \cdot \boldsymbol{\mathcal{E}} = \left.\frac{\partial f_{\boldsymbol{k}}}{\partial t}\right|_{\text{sc}}. \tag{3.5}$$

Within the semiclassical approach, the distribution function of the non-equilibrium system $f_{\boldsymbol{k}}$ is separated into two terms

$$f_{\boldsymbol{k}} = f^0(E_{\boldsymbol{k}}) + g_{\boldsymbol{k}}, \tag{3.6}$$

where the first term $f^0(E_{\boldsymbol{k}})$ represents the equilibrium distribution function and the second term $g_{\boldsymbol{k}}$ is the deviation from the equilibrium due to the external field. The distribution function in the equilibrium $f^0(E_{\boldsymbol{k}})$ is given by the Fermi-Dirac distribution function

$$f^0(E_{\boldsymbol{k}}) = \left[1 + \exp\frac{E_{\boldsymbol{k}} - E_F}{k_B T}\right]^{-1}, \tag{3.7}$$

with k_B the Boltzmann constant and T the temperature. Inserting the sum of the distribution function (Eq. (3.6)) into the Boltzmann equation (3.2), as well as using the chain rule for the derivative and the definition of the group velocity (Eq. 3.3), we arrive at the following form of the Boltzmann equation

$$e\frac{\partial f^0(E_{\boldsymbol{k}})}{\partial E_{\boldsymbol{k}}}\boldsymbol{v}_{\boldsymbol{k}}\cdot\boldsymbol{\mathcal{E}} = \left.\frac{\partial f_{\boldsymbol{k}}}{\partial t}\right|_{\text{sc}}. \tag{3.8}$$

We consider that the deviation $g_{\boldsymbol{k}}$ will be linear in the electric field, therefore the term $\nabla_{\boldsymbol{k}} g_{\boldsymbol{k}}\cdot\boldsymbol{\mathcal{E}}$ is higher than first order in the electric field and is neglected.

The scattering term of Boltzmann equation (right-hand side of Eq. 3.8) is expressed in terms of the transition rate $w_{\boldsymbol{k}\boldsymbol{k}'}$ (Eq. (2.77)) for scattering from a state $n\boldsymbol{k}$ into a state $n'\boldsymbol{k}'$. The rate of change of the distribution $f_{\boldsymbol{k}}$ consists of two terms, one increasing the value of f for the electrons that are scattered from occupied states $\boldsymbol{k}'$ to unoccupied states $\boldsymbol{k}$ (scattering-in term) and one decreasing the value of the distribution f for the electrons that are scattered out from the states $\boldsymbol{k}$ to $\boldsymbol{k}'$ (scattering-out term). Thus, the change of the distribution function, because of scattering is written [77] [1]

$$\left.\frac{\partial f_{\boldsymbol{k}}}{\partial t}\right|_{\text{sc}} = \sum_{\boldsymbol{k}'}(f_{\boldsymbol{k}'}w_{\boldsymbol{k}'\boldsymbol{k}} - f_{\boldsymbol{k}}w_{\boldsymbol{k}\boldsymbol{k}'}) \tag{3.10}$$

$$= \sum_{\boldsymbol{k}'}(g_{\boldsymbol{k}'}w_{\boldsymbol{k}'\boldsymbol{k}} - g_{\boldsymbol{k}}w_{\boldsymbol{k}\boldsymbol{k}'}) + f^0(E_{\boldsymbol{k}})\sum_{\boldsymbol{k}'}(w_{\boldsymbol{k}'\boldsymbol{k}} - w_{\boldsymbol{k}\boldsymbol{k}'}) \tag{3.11}$$

$$= \sum_{\boldsymbol{k}'}(g_{\boldsymbol{k}'}w_{\boldsymbol{k}'\boldsymbol{k}} - g_{\boldsymbol{k}}w_{\boldsymbol{k}\boldsymbol{k}'}), \tag{3.12}$$

where on the second term on the rhs of Eq. (3.11), we have used the energy conserving property of the scattering rate, according to Eq. (2.77), which gives us the following property for the equilibrium distribution function $f^0(E_{\boldsymbol{k}}) = f^0(E_{\boldsymbol{k}'})$. Additionally, due to the property[2] $\sum_{\boldsymbol{k}'} w_{\boldsymbol{k}'\boldsymbol{k}} = \sum_{\boldsymbol{k}'} w_{\boldsymbol{k}\boldsymbol{k}'}$, this term vanishes and the scattering term of Boltzmann equation is finally written only in terms of the distribution function of the deviation.

In the limit of a weak electric field $\boldsymbol{\mathcal{E}}$ and assuming a linear response of the system, i.e. $g_{\boldsymbol{k}} \sim \boldsymbol{\mathcal{E}}$, the deviation of the distribution function can be given by the vector mean free math $\boldsymbol{\Lambda}_{\boldsymbol{k}}$. The mean free path $\boldsymbol{\Lambda}_{\boldsymbol{k}}$ denotes the average distance traveled by the

[1] Another form that is usually presented for the determination of the scattering term, includes additional factors in Eq. (3.10) which ensure that the initial state is occupied. Then, one expects the following expression

$$\left.\frac{\partial f_{\boldsymbol{k}}}{\partial t}\right|_{\text{sc}} = \sum_{\boldsymbol{k}'} f_{\boldsymbol{k}'}(1-f_{\boldsymbol{k}})w_{\boldsymbol{k}'\boldsymbol{k}} - f_{\boldsymbol{k}}(1-f_{\boldsymbol{k}'})w_{\boldsymbol{k}\boldsymbol{k}'}. \tag{3.9}$$

However, according to Kohn and Luttinger (Appendix in Ref. [77]), this is not the case.

[2] The left-hand side of the equation $\sum_{\boldsymbol{k}'} w_{\boldsymbol{k}'\boldsymbol{k}} = \sum_{\boldsymbol{k}'} w_{\boldsymbol{k}\boldsymbol{k}'}$ gives the total rate of scattering into the state $\boldsymbol{k}'$ from all other states, while the right-hand side gives the total rate of scattering out of the state $\boldsymbol{k}'$ into all other states. These two terms should be equal, otherwise the weight of the state $\boldsymbol{k}'$ would either increase or decrease with the time even in the equilibrium state, which is unphysical. The property is a weak version of the microreversibility condition.

electron between two successive scattering events. During this scattering process, the electron is accelerated moving from the position of scattering $\boldsymbol{r}_0$ to the position $\boldsymbol{r}$, by the electric field. As a result of its acceleration, the electron gains kinetic energy equal to $-e\boldsymbol{\mathcal{E}} \cdot (\boldsymbol{r} - \boldsymbol{r}_0)$. The average distance $(\boldsymbol{r} - \boldsymbol{r}_0)$ can be replaced by the mean free math $\boldsymbol{\Lambda_k}$, according to its definition. Thus, the energy of the electron changes from $E_{\boldsymbol{k}}$ to

$$E_{\boldsymbol{k}} - e\boldsymbol{\mathcal{E}} \cdot \boldsymbol{\Lambda_k}. \tag{3.13}$$

By the expansion of the distribution function $f_{\boldsymbol{k}}$ around the equilibrium distribution function $f^0(E_{\boldsymbol{k}})$ in powers of the electric field

$$f_{\boldsymbol{k}} = f^0(E_{\boldsymbol{k}}) + \boldsymbol{\mathcal{E}} \cdot \nabla_{\boldsymbol{\mathcal{E}}} f_{\boldsymbol{k}} + \cdots, \tag{3.14}$$

and making use of the chain rule of the derivative

$$\boldsymbol{\mathcal{E}} \cdot \nabla_{\boldsymbol{\mathcal{E}}} f_{\boldsymbol{k}} = \frac{\partial f_{\boldsymbol{k}}}{\partial E_{\boldsymbol{k}}} \boldsymbol{\mathcal{E}} \cdot \nabla_{\boldsymbol{\mathcal{E}}} E_{\boldsymbol{k}} \approx \frac{\partial f^0(E_{\boldsymbol{k}})}{\partial E_{\boldsymbol{k}}} \boldsymbol{\mathcal{E}} \cdot \nabla_{\boldsymbol{\mathcal{E}}} E_{\boldsymbol{k}}, \tag{3.15}$$

we find the following relation for the deviation distribution function

$$g_{\boldsymbol{k}} = f_{\boldsymbol{k}} - f^0(E_{\boldsymbol{k}}) = \frac{\partial f^0(E_{\boldsymbol{k}})}{\partial E_{\boldsymbol{k}}} \boldsymbol{\mathcal{E}} \cdot \nabla_{\boldsymbol{\mathcal{E}}} E_{\boldsymbol{k}}. \tag{3.16}$$

We replace in the above equation (3.16) the energy derivative by Eq. (3.13), and we finally make the following ansatz for the distribution function $g_{\boldsymbol{k}}$, related to the vector mean free path $\boldsymbol{\Lambda_k}$

$$g_{\boldsymbol{k}} = -e \frac{\partial f^0(E_{\boldsymbol{k}})}{\partial E_{\boldsymbol{k}}} \boldsymbol{\mathcal{E}} \cdot \boldsymbol{\Lambda_k}. \tag{3.17}$$

In the low-temperature limit ($T \to 0$), the derivative of the equilibrium distribution function turns into a δ-function ($-\frac{\partial f^0(E_{\boldsymbol{k}})}{\partial E_{\boldsymbol{k}}} \to \delta(E_{\boldsymbol{k}} - E_F)$). Hence, the distribution function $g_{\boldsymbol{k}}$ is given by

$$g_{\boldsymbol{k}} = e\ \delta(E_{\boldsymbol{k}} - E_F) \boldsymbol{\mathcal{E}} \cdot \boldsymbol{\Lambda_k}. \tag{3.18}$$

Substituting Eq. (3.17) into Eq. (3.12), we arrive at another expression of the Boltzmann equation

$$\left.\frac{\partial f_{\boldsymbol{k}}}{\partial t}\right|_{\text{sc}} = -\ e \frac{\partial f^0(E_{\boldsymbol{k}})}{\partial E_{\boldsymbol{k}}} \boldsymbol{\mathcal{E}} \cdot \sum_{\boldsymbol{k'}} (\boldsymbol{\Lambda_{k'}} w_{\boldsymbol{k'k}} - \boldsymbol{\Lambda_k} w_{\boldsymbol{kk'}}), \tag{3.19}$$

written in terms of the vector mean free path $\boldsymbol{\Lambda_k}$, instead of the distribution function. Combining this expression (Eq. (3.19)) with Eq. (3.8), we obtain the following relation for the vector mean free path

$$\begin{aligned} e \frac{\partial f^0(E_{\boldsymbol{k}})}{\partial E_{\boldsymbol{k}}} \boldsymbol{v_k} \cdot \boldsymbol{\mathcal{E}} = -\ e \frac{\partial f^0(E_{\boldsymbol{k}})}{\partial E_{\boldsymbol{k}}} \boldsymbol{\mathcal{E}} \cdot \sum_{\boldsymbol{k'}} (\boldsymbol{\Lambda_{k'}} w_{\boldsymbol{k'k}} - \boldsymbol{\Lambda_k} w_{\boldsymbol{kk'}}) \Rightarrow \\ \boldsymbol{\Lambda_k} \cdot \hat{n}_{\boldsymbol{\mathcal{E}}} = \frac{1}{\sum_{\boldsymbol{k'}} w_{\boldsymbol{kk'}}} \left[\boldsymbol{v_k} \cdot \hat{n}_{\boldsymbol{\mathcal{E}}} + \sum_{\boldsymbol{k'}} w_{\boldsymbol{k'k}} (\boldsymbol{\Lambda_{k'}} \cdot \hat{n}_{\boldsymbol{\mathcal{E}}}) \right]. \end{aligned} \tag{3.20}$$

Eq. (3.20) can be further manipulated, inserting the relaxation time $\tau_{\boldsymbol{k}}$ of a state $\boldsymbol{k}$ for electron scattering off impurities, defined as

$$\tau_{\boldsymbol{k}} = \frac{1}{\sum_{\boldsymbol{k'}} w_{\boldsymbol{k}\boldsymbol{k'}}}. \tag{3.21}$$

Thus, we arrive at the following self-consistent equation for the vector mean free path

$$\boldsymbol{\Lambda}_{\boldsymbol{k}} \cdot \hat{n}_{\boldsymbol{\mathcal{E}}} = \tau_{\boldsymbol{k}} \left[\boldsymbol{v}_{\boldsymbol{k}} \cdot \hat{n}_{\boldsymbol{\mathcal{E}}} + \sum_{\boldsymbol{k'}} w_{\boldsymbol{k'}\boldsymbol{k}} (\boldsymbol{\Lambda}_{\boldsymbol{k'}} \cdot \hat{n}_{\boldsymbol{\mathcal{E}}}) \right], \tag{3.22}$$

which depends only on the direction of the electric field, $\hat{n}_{\boldsymbol{\mathcal{E}}} = \boldsymbol{\mathcal{E}}/|\boldsymbol{\mathcal{E}}|$, as it is expected, since we are only interested in the linear response of the system to the electric field. As a result, setting the field along different directions, we have at hand independent equations, one for each component of the vector mean free path.

The Boltzmann equation is solved self-consistently (as presented in the flow diagram in the next subsection), beyond the relaxation time approximation, thus accounting for the vertex corrections, due to the inclusion of the scattering-in term [73, 78].

As it is known, at the low temperature limit, only the electrons at the Fermi surface may be excited by the electric field. Therefore, the transport properties are studied for the states at the Fermi energy, and as a consequence the mean free path needs to be determined only for the Fermi surface states. Thus, the sum over $\boldsymbol{k}$, which represents the multi-index $\boldsymbol{k} \to (n\boldsymbol{k})$, can be replaced by an integral over the isoenergy surface, Fermi surface (FS), and an integration over the energies (perpendicular direction to the isoenergy surface)

$$\sum_{\boldsymbol{k'}} \longrightarrow \frac{1}{\Omega_{\mathrm{BZ}}} \sum_{n'} \int_{\mathrm{BZ}} d^3k' = \frac{1}{\Omega_{\mathrm{BZ}}} \sum_{n'} \int dE \int_{\mathrm{FS}} \frac{d\boldsymbol{k'}_{\parallel}}{\hbar |\boldsymbol{v}_{\boldsymbol{k'}}|}, \tag{3.23}$$

where Ω_{BZ} is the volume of the Brillouin zone and $d\boldsymbol{k'}_{\parallel}$ denotes the isoenergy-surface element. In Eq. (3.23) we have used the chain rule, and the definition of the group velocity (Eq. (3.3)).

Therefore, Eq. (7.5) can be reformulated to a Fermi surface integral, written as

$$\boldsymbol{\Lambda}_{\boldsymbol{k}} \cdot \hat{n}_{\boldsymbol{\mathcal{E}}} = \tau_{\boldsymbol{k}} \left[\boldsymbol{v}_{\boldsymbol{k}} \cdot \hat{n}_{\boldsymbol{\mathcal{E}}} + \frac{1}{\Omega_{\mathrm{BZ}}} \sum_{n'} \int_{\mathrm{FS}} \frac{d\boldsymbol{k}_{\parallel}}{\hbar |\boldsymbol{v}_{\boldsymbol{k'}}|} w_{\boldsymbol{k'}\boldsymbol{k}} (\boldsymbol{\Lambda}_{\boldsymbol{k'}} \cdot \hat{n}_{\boldsymbol{\mathcal{E}}}) \right]. \quad k \in \mathrm{FS} \tag{3.24}$$

Solution of Boltzmann equation

The linearized Boltzmann transport equation can be solved numerically with iterations (Fig. 3.1). As a starting point, the vector mean free path $\boldsymbol{\Lambda}_{\boldsymbol{k}}$ on the rhs of Eq. (3.24) is replaced by $\boldsymbol{\Lambda}_k^{(\mathrm{in})} = \tau_{\boldsymbol{k}} \boldsymbol{v}_{\boldsymbol{k}}$, following the so-called relaxation time approximation. Then, by the solution of Boltzmann equation a new vector mean free path, $\boldsymbol{\Lambda}_k^{(\mathrm{out})}$, is derived.

The iterations are performed until the self-consistency is achieved, i.e., the average root-mean-square (RMS) be calculated in the order of 10^{-9}. The RMS is given by

$$\mathrm{RMS}_i = \frac{\sqrt{\sum_k (\Lambda_{k,i}^{(\mathrm{out})} - \Lambda_{k,i}^{(\mathrm{in})})^2}}{N_{\boldsymbol{k}} N_n}, \qquad i \in (x, y, z), \tag{3.25}$$

where $N_{\boldsymbol{k}}$ represents the number of k-points and N_n is the degree of degeneracy.

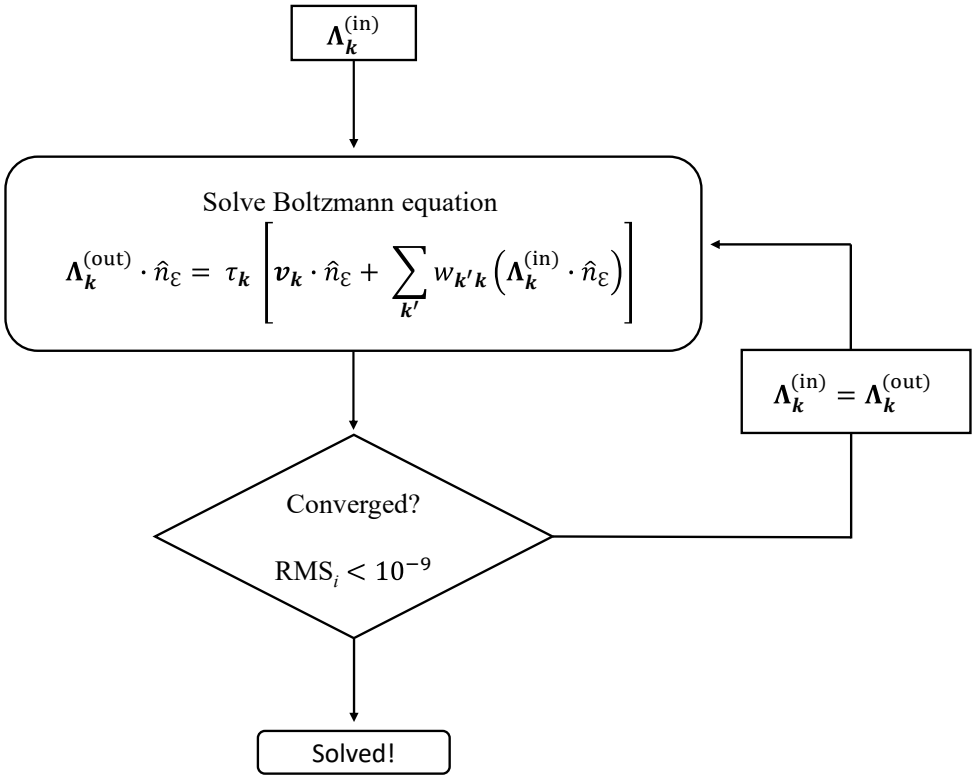

Figure 3.1: The flowchart representing the iterative method used for the self-consistent solution of the linearized Boltzmann transport equation.

3.2 Calculation of the conductivity tensor

The response of electrons under the application of an external electric field $\boldsymbol{\mathcal{E}}$ is described by Ohm's law:

$$\boldsymbol{j} = \boldsymbol{\sigma}\boldsymbol{\mathcal{E}}. \tag{3.26}$$

Once the mean free path has been calculated, the charge current density can be found by means of the distribution function, as follows

$$\begin{aligned}\boldsymbol{j} &= \frac{e}{\Omega}\sum_{\boldsymbol{k}} \boldsymbol{v}_{\boldsymbol{k}} f_{\boldsymbol{k}} = \frac{e}{\Omega}\sum_{\boldsymbol{k}} \boldsymbol{v}_{\boldsymbol{k}}[f^0(E_{\boldsymbol{k}}) + g_{\boldsymbol{k}}] \\ &= \frac{e^2}{\Omega\ \Omega_{\mathrm{BZ}}}\sum_n \int \delta(E_{\boldsymbol{k}} - E_{\mathrm{F}})dE \int_{\mathrm{FS}} \frac{d\boldsymbol{k}_{\parallel}}{\hbar|\boldsymbol{v}_{\boldsymbol{k}}|}\boldsymbol{v}_{\boldsymbol{k}}(\boldsymbol{\Lambda}_{\boldsymbol{k}} \cdot \boldsymbol{\mathcal{E}}) \\ &= \frac{e^2}{\hbar(2\pi)^3}\sum_n \int_{\mathrm{FS}} \frac{d\boldsymbol{k}_{\parallel}}{|\boldsymbol{v}_{\boldsymbol{k}}|}\boldsymbol{v}_{\boldsymbol{k}}(\boldsymbol{\Lambda}_{\boldsymbol{k}} \cdot \boldsymbol{\mathcal{E}}),\end{aligned} \tag{3.27}$$

with $\Omega = 8\pi^3/\Omega_{\mathrm{BZ}}$ the crystal volume. From the first to second line we have used the fact that the equilibrium distribution does not contribute to the current, and the distribution function has been replaced by Eq. (3.18).

The knowledge of the current density $\boldsymbol{j}$ allows us to calculate the conductivity tensor σ_{ij}, as it is easily given as the prefactor to the electric field, according to Ohm's law (Eq. (3.26))

$$\sigma_{ij} = \frac{e^2}{\hbar(2\pi)^3}\sum_n \int_{\mathrm{FS}} \frac{d\boldsymbol{k}_{\parallel}}{|\boldsymbol{v}_{\boldsymbol{k}}|}(\boldsymbol{v}_{\boldsymbol{k}})_i\ (\boldsymbol{\Lambda}_{\boldsymbol{k}})_j, \tag{3.28}$$

with $i, j = x, y, z$.

4 Spin-orbit torque within KKR method

4.1 Spin-orbit torque

The spin-orbit torque (SOT) is related to the field of the electrically controlled spintronics, as it generates a precession of the magnetization in response to an electric current. The possibility of current-induced spin torques has been already shown in the past three decades, at first by Berger [6] and Slonczewski [5], with the prediction of the mechanism of the spin-transfer torque (STT). The physical origin of the STT is the transfer of spin angular momentum between two ferromagnetic layers with noncollinear magnetization direction. This concept of the spin-transfer torque [7] technology is currently used for manipulating the bit states in magnetic random access memories (MRAMs) [8]. The spin polarization arising from an electric current that flows through a ferromagnetic layer ("polarizer"), exerts a magnetic torque causing the precession of the magnetization.

Developments of the past few years, have focused on the replacement of the spin-transfer torque on STT-MRAMs by a new type of current-induced spin torque, the so-called spin-orbit torque (SOT) [9], which allows the control of the magnetization without the need of a polarizer. In contrast to the spin-transfer torques, in these torques the orbital angular momentum of the conduction electrons from the crystal lattice is transferred to the angular momentum of the spin system [11]. The idea of the SOT phenomenon, can be described by the precession of the magnetization due to an electrical

current which flows through a bilayer consisting of a ferromagnet on a substrate of a nonmagnetic material. The electric current flowing parallel to the interface generates a spin accumulation originating from spin-orbit coupling (SOC) of the nonmagnetic material, which acts on the magnetization of the ferromagnetic material, causing the spin precession. As this spin torque phenomenon arises from the SOC, is called spin-orbit torque. Because of the direct link of this effect with the SOC, the nonmagnetic material which is normally used, is a heavy metal which is characterized by strong spin-orbit interaction.

Phenomenological description of SOT

The magnetization dynamics induced by the phenomenon of the spin-orbit torque can be described by the phenomenological Landau-Lifshitz-Gilberg (LLG) equation with an additional term that is related to the torque $\boldsymbol{T}$ [9]

$$\frac{d\hat{\boldsymbol{M}}}{dt} = -|\gamma|\hat{\boldsymbol{M}} \times \boldsymbol{B}^{eff} + \alpha\hat{\boldsymbol{M}} \times \frac{d\hat{\boldsymbol{M}}}{dt} - \frac{|\gamma|}{M_s}\boldsymbol{T}(\boldsymbol{\mathcal{E}}), \tag{4.1}$$

with $\hat{\boldsymbol{M}} = \boldsymbol{M}/M_s$ the magnetization unit vector and M_s the saturation magnetization. Here, $|\gamma|$ is the absolute value of the gyromagnetic ratio of electrons and α is the Gilbert damping parameter. The first term on the right-hand side of Eq. (4.1) represents the precession of the magnetization around the effective field $\boldsymbol{B}^{eff}$, which contains the effect of external magnetic fields. The second term describes the tendency of the magnetization to relax toward its equilibrium position. The third term represents the change of the magnetization due to the torque $\boldsymbol{T}$ which is induced by an electrical current of an applied electric field $\boldsymbol{\mathcal{E}}$.

The torque in its general form consists of two terms, the perpendicular component and the longitudinal component of the torque. The perpendicular torque which acts on the magnetization like an effective magnetic field, is known as field like term. The longitudinal torque which acts as an effective magnetic damping, is called damping like term.

The spin-orbit torque is by definition orthogonal to the magnetization and can be determined as a function of the magnetization direction $\hat{\boldsymbol{M}}$. In analogy to field like and damping like terms of the torque, according to investigations in bilayer systems [13, 20], the SOT is decomposed in two components

$$\boldsymbol{T} = \boldsymbol{T}^{\text{even}} + \boldsymbol{T}^{\text{odd}}. \tag{4.2}$$

The first component is an even function of the magnetization unit vector, given by

$$\boldsymbol{T}^{\text{even}} = T^{\text{even}}\hat{\boldsymbol{M}} \times [(\hat{\boldsymbol{e}}_z \times \boldsymbol{\mathcal{E}}) \times \hat{\boldsymbol{M}}], \tag{4.3}$$

and the second component is an odd function to lowest order of the magnetization direction $\hat{\boldsymbol{M}}$, written as

$$\boldsymbol{T}^{\text{odd}} = T^{\text{odd}}(\hat{\boldsymbol{e}}_z \times \boldsymbol{\mathcal{E}}) \times \hat{\boldsymbol{M}}, \tag{4.4}$$

where $\boldsymbol{e}_z$ indicates the unit vector in the out-of plane direction (perpendicular to the interface), while the direction of the applied electric field $\boldsymbol{\mathcal{E}}$ is considered in-plane (parallel to the interface).

Theory of SOT

The phenomenon of the spin-orbit torque can be treated within local spin density approximation (LSDA) to density functional theory (DFT). Within this approximation, the many-electron system is described by the following non-interacting particle Hamiltonian [9, 14]

$$H = K + V_{\text{eff}} + H_{\text{SO}} + \boldsymbol{\sigma} \cdot \boldsymbol{B}^{\text{xc}}. \tag{4.5}$$

This Hamiltonian contains the kinetic energy K, the crystal potential V_{eff}, the spin-orbit interaction term, and the last term which describes the exchange interaction. $\boldsymbol{\sigma}$ is the vector of Pauli matrices which represents the spin magnetic moment operator and $\boldsymbol{B}^{\text{xc}}$ the exchange field (Eq. (2.12)). The spin-polarized part of the exchange correlation potential $\boldsymbol{B}^{\text{xc}}$, which is expressed in units of energy, is defined as the difference between the potentials of majority and minority electrons in a local frame of reference where the spin density matrix is diagonal.

The torque on the magnetization at point $\boldsymbol{r}$ is represented by the torque operator $\boldsymbol{\mathcal{T}}(\boldsymbol{r})$, defined as the external product of the spin with the magnetic part of the exchange-correlation field [9, 13]

$$\boldsymbol{\mathcal{T}}(\boldsymbol{r}) = -\boldsymbol{\sigma} \times \boldsymbol{B}^{\text{xc}}(\boldsymbol{r}). \tag{4.6}$$

Within linear-response theory, the spin-orbit torque can be related to an applied electric field $\boldsymbol{\mathcal{E}}$ by a linear-response expression [13]

$$\boldsymbol{T} = \boldsymbol{t}\boldsymbol{\mathcal{E}}, \tag{4.7}$$

which defines the torkance tensor $\boldsymbol{t}$. In this work our interest will be focused on the response coefficient of the SOT on the electric field $\boldsymbol{t}$, within DFT-KKR method combined with Boltzmann formalism.

4.2 Expectation value of the spin, spin-orbit torque and spin flux operator

In this Section, the development of the formalism for the calculation of the expectation value of the torque, spin and spin flux operators in KKR formalism is presented. The formalism proposed by Géranton et al. [16], who studied the torque exerted on the atoms of the magnetic host system FePt/Pt, is extended to the calculation of the spin orbit-torque on impurity atoms. This is achieved with the solution of the expressions for the torque, spin and spin flux operators with the impurity scattering wavefunctions $\psi^{\text{imp}}_{\boldsymbol{k}}$ (Eq. (2.66)), instead of the Bloch wavefunctions which are used in Géranton et al. methodology.

Normalization of the wavefunction

The wavefunctions need to satisfy the following condition in order to be normalized

$$\left\langle \psi_{\boldsymbol{k}}^{\mathrm{imp}} \middle| \psi_{\boldsymbol{k}}^{\mathrm{imp}} \right\rangle = 1. \tag{4.8}$$

The left-hand side of Eq. (4.8) is also written in the form

$$\left\langle \psi_{\boldsymbol{k}}^{\mathrm{imp}} \middle| \psi_{\boldsymbol{k}}^{\mathrm{imp}} \right\rangle = \sum_{\mu} \int_{\Omega_\mu} d\boldsymbol{r}\ |\psi_{\boldsymbol{k}}^{\mathrm{imp}}(\boldsymbol{r})|^2 \tag{4.9}$$

$$= \sum_{\mu} \int d\boldsymbol{r}\ \theta^{\mu}(\boldsymbol{r})[\psi_{\boldsymbol{k}}^{\mathrm{imp}}(\boldsymbol{r})]^{\dagger}\psi_{\boldsymbol{k}}^{\mathrm{imp}}(\boldsymbol{r}), \tag{4.10}$$

where Ω_μ is the volume of the atomic site μ. The space integration is extended to the full space by introducing the shape function $\theta^{\mu}(\boldsymbol{r})$ [1] of the atomic cells.

Using the relation which connects the impurity wavefunctions $\psi_{\boldsymbol{k}}^{\mathrm{imp}}$ with the radial solutions $R_L^{\mathrm{imp},s}(r;E)$ and the eigenvectors $c_{\boldsymbol{k}\Lambda}^{\mathrm{imp}}$ (Eq. (2.66)), and expanded the radial solutions in real spherical harmonics (Eq. (2.68)), as well as the shape functions according to relation $\theta^{\mu}(\boldsymbol{r}) = \sum_L \theta_L(r)Y_L(\hat{r})$, the above equation is expressed in the form [71]

$$\left\langle \psi_{\boldsymbol{k}}^{\mathrm{imp}} \middle| \psi_{\boldsymbol{k}}^{\mathrm{imp}} \right\rangle = \sum_{\mu} \sum_{ss'} \sum_{LL'} [c_{\boldsymbol{k}L}^{\mathrm{imp,s},\mu}]^{*}\ \rho_{LL'}^{ss',\mu}\ c_{\boldsymbol{k}'}^{\mathrm{imp},s',\mu}, \tag{4.12}$$

with the matrix elements $\rho_{LL'}^{ss',\mu}$ defined as

$$\rho_{LL'}^{ss',\mu}(E) = \sum_{L_1L_2L_3} C_{L_1L_2L_3} \int dr\ \theta_{L_1}^{\mu}(r)[R_{L_2L}^{\mathrm{imp},s,\mu}(r;E)]^{\dagger} R_{L_3L'}^{\mathrm{imp},s',\mu}(r;E). \tag{4.13}$$

Spin expectation value

The i-th Cartesian component of the expectation value of the spin operator $\boldsymbol{\sigma}$ for the scattering state $\boldsymbol{k}$ integrated in the volume of the atomic cell Ω_μ of the impurity atom μ is determined by

$$\langle \sigma_{i\mu} \rangle_{\boldsymbol{k}} = \left\langle \psi_{\boldsymbol{k}}^{\mathrm{imp}} \middle| \sigma_{i\mu} \middle| \psi_{\boldsymbol{k}}^{\mathrm{imp}} \right\rangle = \int_{\Omega_\mu} d\boldsymbol{r}\ [\psi_{\boldsymbol{k}}^{\mathrm{imp}}(\boldsymbol{r})]^{\dagger}\sigma_i[\psi_{\boldsymbol{k}}^{\mathrm{imp}}(\boldsymbol{r})], \tag{4.14}$$

with σ_i corresponds to Pauli matrices σ_x, σ_y, σ_z, as defined in Eq. (2.10). Following the same scheme, as described for the normalization of the coefficients, i.e. replacing in

[1]
$$\theta^{\mu}(\boldsymbol{r}) = \begin{cases} 1, & \text{if } \boldsymbol{r} \in \text{cell } \mu \\ 0, & \text{otherwise} \end{cases} \tag{4.11}$$

Eq. (4.14) the expression of the impurity wavefunction ($\psi^{\mathrm{imp},\mu}_{\boldsymbol{k}}$), according to Eq. (2.66), the spin expectation value is written

$$\langle\sigma_{i\mu}\rangle_{\boldsymbol{k}} = \sum_{ss'}\sum_{LL'}[c^{\mathrm{imp,s},\mu}_{\boldsymbol{k}L}]^* c^{\mathrm{imp},s',\mu}_{\boldsymbol{k}L'} \int d\boldsymbol{r}\ \theta^{\mu}(\boldsymbol{r})[R^{\mathrm{imp},s,\mu}_{L}(\boldsymbol{r};E)]^{\dagger}\sigma_i R^{\mathrm{imp},s',\mu}_{L'}(\boldsymbol{r};E). \tag{4.15}$$

By the expansion of the radial solutions and the shape function into spherical harmonics, the Eq. (4.15) is transformed into

$$\langle\sigma_{i\mu}\rangle_{\boldsymbol{k}} = \sum_{ss'}\sum_{LL'}[c^{\mathrm{imp,s},\mu}_{\boldsymbol{k}L}]^*\ \Sigma^{ss',\mu}_{LL',i}\ c^{\mathrm{imp},s',\mu}_{\boldsymbol{k}L'}, \tag{4.16}$$

where the spin matrix elements $\Sigma^{ss',\mu}_{LL',i}$ are introduced, given by the relation [71, 79]

$$\begin{aligned}\Sigma^{ss',\mu}_{LL',i}(E) &= \int d\boldsymbol{r}\ \theta^{\mu}(\boldsymbol{r})[R^{\mathrm{imp},s,\mu}_{L}(\boldsymbol{r};E)]^{\dagger}\sigma_i R^{\mathrm{imp},s',\mu}_{L'}(\boldsymbol{r};E)\\ &= \sum_{L_1L_2L_3} C_{L_1L_2L_3}\int dr\ \theta^{\mu}_{L_1}(r)[R^{\mathrm{imp},s,\mu}_{L_2L}(r;E)]^{\dagger}\sigma_i R^{\mathrm{imp},s',\mu}_{L_3L'}(r;E).\end{aligned} \tag{4.17}$$

The spin matrix elements are $\boldsymbol{k}$ independent and are calculated only once per energy. In particular, in order to perform Fermi surface calculations, the spin matrix elements are calculated for the Fermi energy in a first step, and in a second step the eigenvectors are determined for each scattering state $\boldsymbol{k}$. In this way, the spin expectation value can be computed efficiently.

Torque expectation value

According to the definition of the torque operator (4.6), its components $\mathcal{T}_i$ (with $i = x, y, z$), are given by

$$\mathcal{T}_i(\boldsymbol{r}) = -\sum_{pq}\epsilon_{ipq}\sigma_p B^{\mathrm{xc}}_q(\boldsymbol{r}), \tag{4.18}$$

with ϵ_{ipq} the Levi-Civita symbol and the indices i, p, q take the values x, y, and z. The exchange correlation field $B^{\mathrm{xc}}(\boldsymbol{r})$ is determined within the LDA, and it is directed opposite to the local magnetization vector $\boldsymbol{M}$ [13].

Then, the expression of the i-th expectation value of the torque operator for the scattering state $\boldsymbol{k}$ can be obtained by integrating over the impurity atom μ

$$\begin{aligned}\langle\mathcal{T}_{i\mu}\rangle_{\boldsymbol{k}} &= \left\langle\psi^{\mathrm{imp}}_{\boldsymbol{k}}\middle|\mathcal{T}_{i\mu}\middle|\psi^{\mathrm{imp}}_{\boldsymbol{k}}\right\rangle\\ &= -\sum_{pq}\epsilon_{ipq}\int_{\Omega_\mu} d\boldsymbol{r}\ [\psi^{\mathrm{imp}}_{\boldsymbol{k}}(\boldsymbol{r})]^{\dagger}\sigma_p[\psi^{\mathrm{imp}}_{\boldsymbol{k}}(\boldsymbol{r})]B^{\mathrm{xc}}_q(\boldsymbol{r}).\end{aligned} \tag{4.19}$$

In analogy to the previous subsection, Eq. (4.19) can be transformed into a matrix multiplication [16]

$$\langle\mathcal{T}_{i\mu}\rangle_{\boldsymbol{k}} = \sum_{ss'}\sum_{LL'}[c^{\mathrm{imp},s,\mu}_{\boldsymbol{k}L}]^*\ \mathfrak{T}^{ss',\mu}_{LL',i}\ c^{\mathrm{imp},s',\mu}_{\boldsymbol{k}L'}, \tag{4.20}$$

with the torque matrix elements $\mathfrak{T}^{ss',\mu}_{LL',i}$ defined as

$$\mathfrak{T}^{ss',\mu}_{LL',i}(E) = -\sum_{pq} \epsilon_{ipq} \int d\boldsymbol{r}\ \theta^{\mu}(\boldsymbol{r})[R^{\mathrm{imp},s,\mu}_{L}(\boldsymbol{r};E)]^{\dagger}\sigma_p R^{\mathrm{imp},s',\mu}_{L'}(\boldsymbol{r};E)B^{\mathrm{xc},\mu}_{q}(\boldsymbol{r}). \tag{4.21}$$

As it has been mentioned, the scattering solutions $R^{\mathrm{imp},s,\mu}_{L}(\boldsymbol{r})$ and the shape function $\theta_{\mu}(\boldsymbol{r})$ are expanded in real spherical harmonics. The exchange field $B^{\mu}_{k}(\boldsymbol{r})$ can be also expanded, $B^{\mathrm{xc},\mu}_{q}(\boldsymbol{r}) = \sum_L B^{\mathrm{xc},\mu}_{L,q}\ Y_L(\hat{\boldsymbol{r}})$. Thus, the calculation of the torque matrix elements depends on an integral of the product of four spherical harmonics. In order to simplify the computational effort, we define the convoluted exchange field $b^{\mu}_{q}(\boldsymbol{r})$

$$b^{\mu}_{q}(\boldsymbol{r}) = B^{\mathrm{xc},\mu}_{q}(\boldsymbol{r})\theta_{\mu}(\boldsymbol{r}), \tag{4.22}$$

which is calculated firstly, and then in Eq. (4.21) we use the expansion of the convoluted field

$$b^{\mu}_{q}(\boldsymbol{r}) = \sum_{L} b^{\mu}_{L,q} Y_L(\hat{r}). \tag{4.23}$$

The torque matrix elements are finally found in the KKR formalism by the equation

$$\mathfrak{T}^{ss',\mu}_{LL',i}(E) = -\sum_{pq} \epsilon_{ipq} \sum_{L_1L_2L_3} C_{L_1L_2L_3} \int dr\ [R^{\mathrm{imp},s,\mu}_{L_1L}(r;E)]^{\dagger}\sigma_p R^{\mathrm{imp},s',\mu}_{L_2L'}(r;E)b^{\mu}_{L_3,q}(r). \tag{4.24}$$

These matrix elements are also depend only on the energy, as spin matrix elements. Hence, similar manipulations are performed for the computation of the torque, as the ones mentioned in the previous subsection for the spin expectation value.

Spin flux expectation value

The spin flux is used to determine how much of the spin current that enters the impurity atomic sphere contributes to the spin-orbit torque and how much is lost to the spin lattice interaction.

The spin flux operator is analogous to the spin current operator, but represents the integrated spin current that enters the muffin-tin sphere through its surface [2]. The i-th Cartesian component of the expectation value of the spin flux operator $\mathcal{Q}_i$ for the scattering state $\boldsymbol{k}$ integrated in the the atomic cell of the impurity atom μ is given by the relation [13, 16, 80]

$$\begin{aligned}\langle \mathcal{Q}_{i\mu} \rangle_{\boldsymbol{k}} &= \left\langle \psi^{\mathrm{imp}}_{\boldsymbol{k}} \middle| \mathcal{Q}_{i\mu} \middle| \psi^{\mathrm{imp}}_{\boldsymbol{k}} \right\rangle \\ &= \frac{\mu_B \hbar}{2ie} \int_{S_\mu} d\boldsymbol{S} \Big[[\psi^{\mathrm{imp}}_{\boldsymbol{k}}(\boldsymbol{r})]^{\dagger}\sigma_i \nabla \psi^{\mathrm{imp}}_{\boldsymbol{k}}(\boldsymbol{r}) - [\nabla \psi^{\mathrm{imp}}_{\boldsymbol{k}}(\boldsymbol{r})]^{\dagger}\sigma_i \psi^{\mathrm{imp}}_{\boldsymbol{k}}(\boldsymbol{r}) \Big],\end{aligned} \tag{4.25}$$

where $\hbar$ is the reduced Planck constant, $e = -|e|$ is the electron's charge, μ_B is the Bohr magneton, and the integration is performed on the surface S_μ of the muffin-tin sphere of the atom μ.

[2] The muffin-tin radius r_{MT} is equal to the half of the first neighbor distance.

Introducing in Eq. (4.25) the expression of the impurity wavefunction (Eq. (2.66)), the expectation value of the spin flux operator is given by

$$\langle \mathcal{Q}_{i\mu} \rangle_{\boldsymbol{k}} = \sum_{ss'} \sum_{LL'} [c^{\mathrm{imp,s},\mu}_{\boldsymbol{k}L}]^* \; q^{ss',\mu}_{LL',i} \; c^{\mathrm{imp},s',\mu}_{\boldsymbol{k}L'}, \tag{4.26}$$

where the spin flux matrix elements $q^{ss',\mu}_{LL',i}$ are written as

$$q^{ss',\mu}_{LL',i}(E) = \frac{\mu_B \hbar}{2ie} \int_{S_\mu} d\boldsymbol{S} \Big[[R^{\mathrm{imp},s,\mu}_{L}(\boldsymbol{r};E)]^\dagger \sigma_i \nabla R^{\mathrm{imp},s',\mu}_{L'}(\boldsymbol{r};E) - [\nabla R^{\mathrm{imp},s,\mu}_{L}(\boldsymbol{r};E)]^\dagger \sigma_i R^{\mathrm{imp},s',\mu}_{L'}(\boldsymbol{r};E) \Big]. \tag{4.27}$$

The integral over the surface of the muffin-tin can be replaced by an integral over the solid angle Ω, using the expression of the infinitesimal surface element $d\boldsymbol{S} = r^2_{\mathrm{MT}} \boldsymbol{e}_\Omega d\Omega$, where r_{MT} is the radius of the muffin-tin sphere and $\boldsymbol{e}_\Omega$ is the unit vector pointing towards the center of the muffin-tin sphere. Inserting the expansion of radial scattering solutions into real spherical harmonics in Eq. (4.27), the spin flux matrix elements are taken the form

$$q^{ss',\mu}_{LL',i}(E) = \frac{\mu_B \hbar}{2ie} \sum_{L_1} \Big[[R^{\mathrm{imp},s,\mu}_{L_1 L}(r;E)]^\dagger \sigma_i \frac{\partial}{\partial r} \Big(R^{\mathrm{imp},s',\mu}_{L_1 L'}(r;E) \Big) - \frac{\partial}{\partial r} \Big([R^{\mathrm{imp},s,\mu}_{L_1 L}(r;E)]^\dagger \Big) \sigma_i R^{\mathrm{imp},s',\mu}_{L_1 L'}(r;E) \Big]_{r=r_{\mathrm{MT}}}, \tag{4.28}$$

and can be computed similarly to spin and torque matrix elements, as analyzed in the previous subsections.

4.3 Response tensors within the Boltzmann formalism

In the following, we derive the expressions for the current-induced spin-orbit torque, spin accumulation, and spin flux, as a response to the applied electric field, within the KKR Green function method and the semi-classical linearized Boltzmann equation (Chapter 3).

Spin accumulation

Having estimated the deviation distribution function $g_{\boldsymbol{k}}$, one can proceed with the calculation of the spin accumulation on impurity atom μ, $\boldsymbol{s}_\mu$, which is written by means of the deviation distribution function in Boltzmann formalism as

$$\boldsymbol{s}_\mu = \sum_{\boldsymbol{k}} g_{\boldsymbol{k}} \, \langle \boldsymbol{\sigma}_\mu \rangle_{\boldsymbol{k}} \, . \tag{4.29}$$

The spin expectation value $\langle \boldsymbol{\sigma}_\mu \rangle_{\boldsymbol{k}}$ is computed by Eq. (4.16). Replacing the deviation distribution function (Eq. (3.18)) in the above equation we find the following Fermi surface (FS) integral for the spin accumulation

$$\boldsymbol{s}_\mu = -\frac{e\mu_B}{\hbar S_{\mathrm{BZ}}} \int_{\mathrm{FS}} \frac{dk_\parallel}{|\boldsymbol{v}_{\boldsymbol{k}}|} (\langle \boldsymbol{\sigma}_\mu \rangle_{\boldsymbol{k}} \otimes \boldsymbol{\Lambda}_{\boldsymbol{k}}) \cdot \boldsymbol{\mathcal{E}}. \tag{4.30}$$

We define the response tensor of the spin accumulation $\boldsymbol{\chi}_\mu$ to the electric field $\boldsymbol{\mathcal{E}}$

$$\boldsymbol{s}_\mu = \boldsymbol{\chi}_\mu \boldsymbol{\mathcal{E}}, \tag{4.31}$$

which is given, according to Eqs. (4.30), (4.31) by the relation

$$\boldsymbol{\chi}_\mu = -\frac{e\mu_B}{\hbar S_{\mathrm{BZ}}} \int_{\mathrm{FS}} \frac{dk}{|\boldsymbol{v}_{\boldsymbol{k}}|} \langle \boldsymbol{\sigma}_\mu \rangle_{\boldsymbol{k}} \otimes \boldsymbol{\Lambda}_{\boldsymbol{k}}. \tag{4.32}$$

This integral (4.32) can be easily calculated, once the Boltzmann transport equation has been solved (Eq. (3.24)) and the mean free path $\boldsymbol{\Lambda}_{\boldsymbol{k}}$ has been computed.

Torkance

In analogy to the calculation of the spin response tensor, the spin-orbit torque that is exerted on impurity atom μ, $\boldsymbol{T}_\mu$, is written in terms of the deviation distribution function as

$$\boldsymbol{T}_\mu = \sum_{\boldsymbol{k}} g_{\boldsymbol{k}} \langle \boldsymbol{\mathcal{T}}_\mu \rangle_{\boldsymbol{k}}, \tag{4.33}$$

where the torque expectation value is calculated by Eq. (4.20). By the equation of the deviation distribution function (Eq. (3.18)) we obtain the following Fermi surface (FS) integral for the impurity-driven spin-orbit torque

$$\boldsymbol{T}_\mu = -\frac{e}{\hbar S_{\mathrm{BZ}}} \int_{\mathrm{FS}} \frac{dk}{|\boldsymbol{v}_{\boldsymbol{k}}|} (\langle \boldsymbol{\mathcal{T}}_\mu \rangle_{\boldsymbol{k}} \otimes \boldsymbol{\Lambda}_{\boldsymbol{k}}) \cdot \boldsymbol{\mathcal{E}}. \tag{4.34}$$

The linear response of the SOT to an external electric field is represented by the torkance tensor $\boldsymbol{t}_\mu$ [13]

$$\boldsymbol{T}_\mu = \boldsymbol{t}_\mu \boldsymbol{\mathcal{E}}. \tag{4.35}$$

Then, it is easily proved by Eqs. (4.34), (4.35) that the torkance of atom μ is computed by the expression

$$\boldsymbol{t}_\mu = -\frac{e}{\hbar S_{\mathrm{BZ}}} \int_{\mathrm{FS}} \frac{dk}{|\boldsymbol{v}_{\boldsymbol{k}}|} \langle \boldsymbol{\mathcal{T}}_\mu \rangle_{\boldsymbol{k}} \otimes \boldsymbol{\Lambda}_{\boldsymbol{k}}. \tag{4.36}$$

Spin flux

In a similar way, we can determine the spin flux which enters the impurity atom μ, $\boldsymbol{\mathcal{Q}}_\mu$, by means of the deviation distribution function

$$\begin{aligned} \boldsymbol{\mathcal{Q}}_\mu &= \sum_{\boldsymbol{k}} g_{\boldsymbol{k}} \langle \boldsymbol{\mathcal{Q}}_\mu \rangle_{\boldsymbol{k}} \Rightarrow \\ \boldsymbol{\mathcal{Q}}_\mu &= \frac{e}{\hbar S_{\mathrm{BZ}}} \int_{\mathrm{FS}} \frac{dk_\parallel}{|\boldsymbol{v}_{\boldsymbol{k}}|} (\langle \boldsymbol{\mathcal{Q}}_\mu \rangle_{\boldsymbol{k}} \otimes \boldsymbol{\Lambda}_{\boldsymbol{k}}) \cdot \boldsymbol{\mathcal{E}}, \end{aligned} \tag{4.37}$$

with the spin flux expectation value $\langle \boldsymbol{\mathcal{Q}}_\mu \rangle_{\boldsymbol{k}}$ computed according to Eq. (4.26). The response coefficient of the spin flux to the electric field, $\boldsymbol{q}_\mu$, which is defined as

$$\boldsymbol{\mathcal{Q}}_\mu = \boldsymbol{q}_\mu \boldsymbol{\mathcal{E}}, \tag{4.38}$$

is computed by the following Fermi surface integral

$$\boldsymbol{q}_\mu = \frac{e}{\hbar S_{\mathrm{BZ}}} \int_{\mathrm{FS}} \frac{dk}{|\boldsymbol{v}_{\boldsymbol{k}}|} \langle \boldsymbol{\mathcal{Q}}_\mu \rangle_{\boldsymbol{k}} \otimes \boldsymbol{\Lambda}_{\boldsymbol{k}}. \tag{4.39}$$

4.4 New implementations in JuKKR code

One of the main subjects of this thesis is the first-principles calculations of the response functions of the spin, spin-orbit torque, and spin flux on magnetic impurity atoms. In previous implementations, these quantities were computed by the JuKKR code, but only for the host atoms [81]. Therefore, further code development was necessary, in order to extend the pre-existing methodology to the calculation of the spin-orbit torque on impurity atoms. The implementation necessitated several changes in the KKR-host code as well as on the KKR-Fermi surface code.

The expression of the torque expectation value at the atom μ of the host system is given in terms of the host Bloch wavefunctions, expressed by the following equation

$$\langle \mathcal{T}_{i\mu} \rangle_{\boldsymbol{k}}^{\mathrm{host}} = -\sum_{ss'} \sum_{LL'} [c_{\boldsymbol{k}L}^{s,\mu}]^* \Big(\sum_{pq} \epsilon_{ipq} \int d\boldsymbol{r}\ \theta^\mu(\boldsymbol{r}) [R_L^{s,\mu}(\boldsymbol{r}; E)]^\dagger \sigma_p R_{L'}^{s',\mu}(\boldsymbol{r}; E) B_q^{\mathrm{xc},\mu}(\boldsymbol{r}) \Big) c_{\boldsymbol{k}L'}^{s',\mu}. \tag{4.40}$$

In Eq. (4.40), the radial solutions $R_L^{s,\mu}(\boldsymbol{r}; E)$ and the host coefficients $c_{\boldsymbol{k}L}^{s,\mu}$, are determined according to relations (2.36) and (2.58), respectively.

On the other hand, for the computation of the torque expectation value at the impurity atom μ, Eq. (4.40) is modified, including the impurity wavefunctions instead of the Bloch wavefunctions, and takes the following form

$$\langle \mathcal{T}_{i\mu} \rangle_{\boldsymbol{k}} = -\sum_{ss'} \sum_{LL'} [c_{\boldsymbol{k}L}^{\mathrm{imp},s,\mu}]^* \Big(\sum_{pq} \epsilon_{ipq} \int d\boldsymbol{r}\ \theta^\mu(\boldsymbol{r}) [R_L^{\mathrm{imp},s,\mu}(\boldsymbol{r}; E)]^\dagger \sigma_p R_{L'}^{\mathrm{imp},s',\mu}(\boldsymbol{r}; E) B_q^{\mathrm{xc},\mu}(\boldsymbol{r}) \Big) c_{\boldsymbol{k}L'}^{\mathrm{imp},s',\mu}. \tag{4.41}$$

Hence, in Eq. (4.41) the radial solutions of the impurity potential $R_L^{\mathrm{imp},s,\mu}(\boldsymbol{r}; E)$ are given by the Lippmann-Schwinger equation (2.67), and the impurity expansion coefficients $c_{\boldsymbol{k}L}^{\mathrm{imp},s,\mu}$ are determined by Eq. (2.74).

Next, the torkance (Eq. (4.36)) is given in terms of torque expectation value on the defect (Eq. (4.41)). Thus, necessary changes are also applied for the computation of the response coefficient of the torque within the solution of the Boltzmann equation. The expectation values of the spin and spin flux, as well as its response coefficients within Boltzmann formalism were implemented in the JuKKR code, accordingly. The results shown in Chapter 5 have been generated by this new version of the code.

Furthermore, the computation of the response function of the spin-orbit torque on magnetic impurity atoms, including non-collinear magnetization, which was previously absent in the code, has been implemented. The exchange correlation field vector is generalized to have an arbitrary direction. In this way, the torque (Eq. (4.41)) is determined including the magnetization direction.

This is a significant modification which allows the study of the spin-orbit torque on non-collinear structures, like systems with magnetic skyrmions.

5 SOT effect on magnetic defects in the Bi_2Te_3 surface

5.1 Introduction

The topological insulators [23, 24] represent a new special materials class, which can be observed in 2 dimensions (2D) or 3 dimensions (3D). Just like ordinary insulators, they present a band gap in the bulk. In contrast, at the surface they are characterized by metallic surface states with special spin texture, originating from the strong spin orbit coupling. These surface states are topologically protected against non-magnetic disorder. This property accompanied by time-reversal symmetry protection, make these materials very promising for spintronic applications.

A prerequisite for the occurrence of these effects is a strong spin-orbit coupling. Its presence makes the topological insulators optimal materials for the observation of spin-orbit torque on magnetic transition-metal impurities embedded in their surface or in ferromagnet/(topological insulator) bilayers. Our focus is on the surface states of Bi_2Te_3, which is an experimentally and theoretically well characterised topological insulator. The topologically protected surface states of Bi_2Te_3 have been verified theoretically [36] and experimentally using ARPES [38], with the existence of a single Dirac cone at the high-symmetry Γ point in the surface Brillouin zone. When an electrical current flows in the surface, a spin accumulation is generated, which acts on the magnetization of ferromagnetically coupled impurities embedded in Bi_2Te_3. This switching of the

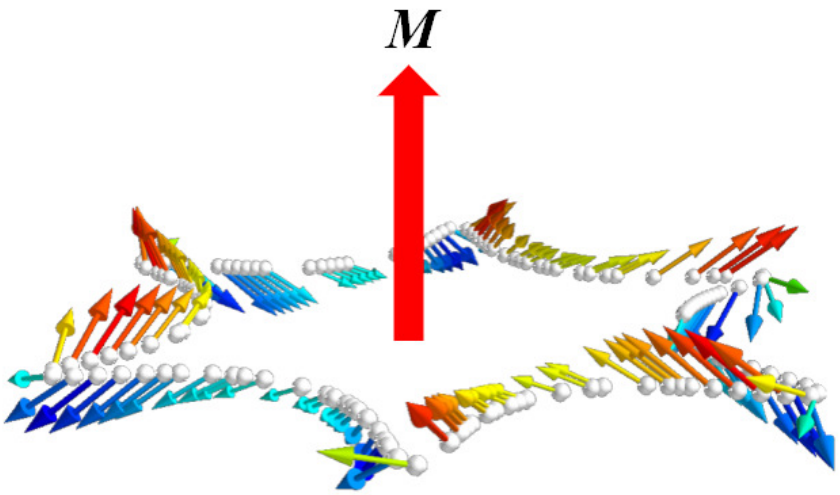

Figure 5.1: The spin polarization of the Fermi surface states of the topological insulator Bi_2Te_3 film (side-view). The red arrow in the middle represents the magnetization $\boldsymbol{M}$ of the magnetic impurity atom.

magnetization by SOT can be used as a new technique in future applications to create MRAMs.

Here, we investigate the spin-orbit torque on (Cr, Mn, Fe, and Co)/Bi_2Te_3 systems. An important characteristic of the studied systems is the existence of the conducting surface states, that leads to the flow of all current through the surface, where the SOT effect is observed, without energy loss in the bulk. In addition, the spin polarization $\boldsymbol{s}$ of the Fermi states is predominantly directed in the plane of the Bi_2Te_3 surface and, consequently, perpendicular to the magnetic impurity spin $\boldsymbol{M}$ which is taken along the surface normal, maximizing the product $\boldsymbol{s} \times \boldsymbol{M}$ that governs the torque. The situation is shown in Fig. 5.1. The preferred out-of-plane orientation of the magnetic moment axis has been established by experiments [82–84] for the Mn/Bi_2Te_3 and Fe/Bi_2Te_3 systems. From the preceding description it is clear that we are after an extrinsic (impurity-mediated) SOT effect. Additionally, our formalism accounts for Fermi-surface but not Fermi-sea contributions.

Because of the aforementioned properties of the proposed system, a much stronger spin-orbit torque effect is expected, compared to the observed phenomenon in ferromagnet/heavy metal bilayers. The spin polarization of the ferromagnet is predominantly parallel to the polarization of the conduction electrons in the bilayer, and, in addition, part of the electric current flows through the bulk of the heavy metal, being far from the interface and not contributing significantly to the SOT.

This Chapter is organized as follows[1]. A short introduction to the discovery of the topological insulators and its special properties, is given in Sec 5.2. In Sec. 5.3 we discuss the electronic structure of Bi_2Te_3 system. Next, in Sec. 5.4 we provide a description of

[1]Parts of this Chapter have been published in Ref. [85].

the studied system, magnetic transition metals embedded in Bi_2Te_3 surface. We consider a collection of magnetic defects on the surface, as it is discussed in Sec. 5.4.1, giving a modification of the usual Boltzmann formalism beyond the independent scattering approximation. Sec. 5.5 includes the results, the correlation of the calculated quantities, and a discussion on the Joule heat as a function of the torque.

5.2 Introduction to topological insulators

Topology is the branch of mathematics concerned with the geometrical properties of spaces, that are invariant through continuous deformations. Two geometrical objects that can be transformed into each other by twisting and stretching, are called topologically equivalent. A popular science example of this concept is a doughnut (i.e. a torus with one hole), which can be smoothly transformed into a coffee mug with a handle through continuous deformations, and vice versa. On the other hand, the moon and a doughnut are topologically inequivalent. The moon is a closed surface without any hole, as a result it can never be smoothly deformed into a doughnut without excluding one point from its surface. These topological spaces are distinguished by an integer topological invariant number, called the genus, g, which can be understood as the number of holes in each shape, i.e. $g = 0$ for the moon and $g = 1$ for the doughnut. In general, the geometrical spaces are classified to topologically equivalent or distinct, according to this invariant.

In analogy, in condensed matter physics, the topological insulators can be defined within the framework of the band theory of solids. A Bloch Hamiltonian $H(\boldsymbol{k})$ with a gapped energy spectrum is considered as topologically equivalent to another Bloch Hamiltonian $H'(\boldsymbol{k})$, if they can be continuously transformed into each other by changing some parameters, without closing the energy gap at any instance during the process of transformation. In Fig. 5.2 a schematic representation of the bulk band structure for a trivial and a topological insulator, is depicted. In a trivial insulator the occupied valence-band states are separated from the empty conduction-band states by a large energy gap. In a topological insulator, at first the gap closes, due to the strong spin-orbit interaction, and the bands are inverted near to the special points, the so-called time reversal invariant momenta (TRIM) points of the first Brillouin zone. Then, this hybridization between the shifted bands leads to the reopening of the band gap. As a consequence, because of the intermediate closing of the gap, a trivial and a topological insulator are determined as topologically inequivalent. The presence of the band inversion in the band structure of the topological insulator is the analog of the presence or absence of holes in the mathematically defined space, as discussed in the previous paragraph. The corresponding topological invariant Z_2 in the 3D topological insulators, that distinguishes the two types of insulating band structures of the trivial and topological insulator, can be evaluated for the TRIM points. The colors in bands represent the parity of the wavefunction.

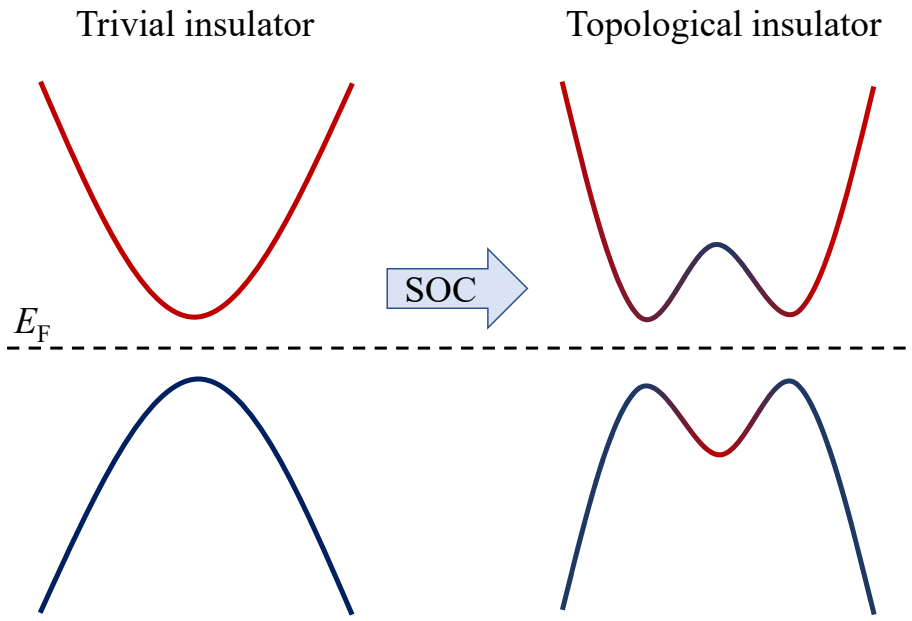

Figure 5.2: Schematic representation of the band structure, for the transition from a trivial insulator to a topological insulator induced by the spin-orbit coupling (SOC). The band inversion in the topological insulator is shown at the center of the bands, indicated by the blue and red colors.

Quantum Hall effect

The quantum Hall effect (QHE) [86, 87] paved the way for the discovery of the topological insulators, as correlates the topological properties of the electronic band structure to physical observables, such as the quantized Hall conductivity. The QHE is observed in 2-dimensional (2D) systems, in which electrons that are subjected to a perpendicular strong magnetic field, are forced into circular orbits. At the edges of the sample, electrons have to bounce off the edge, performing skipping orbits. These edge electronic states propagate only in one direction, and because of this are also known as chiral states. During this mechanism, the Hall conductivity is quantized and proportional to a topological invariant n, which is called Chern number. Thus, the quantized Hall conductivity σ_{xy} for the anomalous QHE, according to Thouless, Kohmoto, Nightingale, and den Nijs [88], can be computed using the Kubo formula, by the following expression

$$\sigma_{xy} = \frac{e^2}{h} n. \tag{5.1}$$

The Chern number is an integer quantity that connects the quantized Hall conductivity with the topology of the system via the Berry curvature $\boldsymbol{\Omega_k}$. This is considered a topological invariant, in the sense that it cannot be changed via a smooth variation of the Hamiltonian. The Chern number n can be expressed as an integral of the Berry curvature

$$\begin{aligned} n &= \frac{1}{2\pi} \int_{\mathrm{BZ}} dk_x dk_y \; \boldsymbol{\Omega_k} \\ &= \frac{1}{2\pi} \int_{\mathrm{BZ}} dk_x dk_y \; \boldsymbol{\nabla_k} \times \boldsymbol{A_k}, \end{aligned} \tag{5.2}$$

where the integral is performed over the surface of the Brillouin zone. $\boldsymbol{A_k}$ is the Berry connection which is expressed in terms of derivatives of the wavefunction $\psi_{\boldsymbol{k}}$ of a Bloch Hamiltonian $H(\boldsymbol{k})$, i.e., $\boldsymbol{A_k} = -i \langle \psi_{\boldsymbol{k}} | \nabla_{\boldsymbol{k}} | \psi_{\boldsymbol{k}} \rangle$. The Berry connection determines the Berry phase [89], which is a phase factor of the wavefunction acquired under an adiabatic cycle in k-space [2]. The Berry phase γ can be evaluated by the line integral

$$\begin{aligned} \gamma &= \oint d\boldsymbol{k} \; \boldsymbol{A_k} \\ &= -i \oint d\boldsymbol{k} \, \langle \psi_{\boldsymbol{k}} | \nabla_{\boldsymbol{k}} | \psi_{\boldsymbol{k}} \rangle \, . \end{aligned} \tag{5.3}$$

Haldane [90] first introduced the concept of the QHE to systems without the application of an external magnetic field. These systems are called Chern insulators, which are non-trivial insulators with broken time-reversal symmetry. Many years later, the quantum anomalous Hall effect observed also experimentally [91] in this kind of insulators.

[2] The Berry phase is $\gamma = \pi$ for the topological insulators [24]. This is determined by the spin texture in the Fermi surface states.

In analogy to QHE in Chern insulators, the quantum spin Hall effect (QSHE) was suggested in graphene [22] and in 2D semiconductor systems [92, 93], arising from the spin orbit coupling in the absense of an external magnetic field. It is established that the spin-orbit coupling plays an important role in the existence of the quantum spin Hall state. These systems are the first prediction of 2D topological insulators, also known as quantum spin Hall insulators.

According to the quantum spin Hall effect (QSHE), along the edge states the electrons with spin up propagate in one direction with crystal momentum $\boldsymbol{k}$ while the electrons of the opposite spin propagate only in the opposite direction with crystal momentum $-\boldsymbol{k}$. Such states are also known as helical states, due to this correlation between spin and momentum. The spin-momentum locking is one of the main characteristics of topological insulators.

The topological properties of 2D QSH states has been generalized in three dimensions [94, 95]. For these types of insulators, the term "topological insulator" is used. The first experimental discovery of a 3D topological insulator phase was established with angle resolved photoemission spectroscopy (ARPES) experiments in $Bi_{1-x}Sb_x$ material [96]. In this material, the topologically non-trivial surface states were observed in its electronic band structure.

The topological classification of materials is related to a fundamental principle according to which the existence of robust surface states is related to the topological nature of the bulk band structure. This is known as bulk-boundary correspondence. Considering a non-trivial insulator, which is characterized by a non-zero Chern number, and a trivial insulator with zero Chern number, at the interface between the two, where the Chern number (i.e. the topological invariant) changes, the gap closes by the appearance of the edge states.

The surface of a topological insulator is its boundary with vacuum, and vacuum (at energies below the onset of free-electron states) is considered as a trivial insulator in the topological sense, thus a topological insulator surface necessarily hosts surface states.

3D topological insulators

In this work, we are interested in the properties of the surface of a 3D topological insulator. The 3D topological insulator is an insulating material in the bulk, while its surface electronic states is gapless, metallic-like states. The topological surface states can be described by a 2D massless Dirac Hamiltonian [24]

$$H_0(\boldsymbol{k}) = v_{\mathrm{F}}(\boldsymbol{k} \times \boldsymbol{\sigma}) \cdot \hat{z}, \tag{5.4}$$

where v_{F} is the Fermi velocity. These surface states are topologically protected against perturbations that preserve the time-reversal symmetry, i.e. in presence of non-magnetic disorder (surface reconstruction, non-magnetic impurities, etc.). Additionally, the coupling of the crystal momentum with the spin in the surface of the topological insulator, i.e. the spin-momentum locking of the topological surface state, combined with the time reversal symmetry, leads to the absence of backscattering (from $\boldsymbol{k}$ to $-\boldsymbol{k}$) in the surface states [97].

In contrast, the topological protection of the conducting surface states on topological insulators breaks in case of attendance of magnetic disorder in the system. The internal magnetic fields of such impurities break the time-reversal symmetry, allowing back scattering. In that case, the transport properties of the system are also affected.

Additionally, the topological insulator provides strong spin-orbit coupling, as mentioned in Sec 5.1. The SOC is essential for the emergence of spin accumulation, and therefore for the existence of the phenomenon of the SOT, that will be investigated in this Chapter.

5.3 Electronic structure of Bi_2Te_3

In a first step, we perform simulations based on KKR Green function method, for the self-consistent convergence of the host crystal structure, which is a Bi_2Te_3 film, and we investigate its electronic properties.

Host system

The surface of Bi_2Te_3 [98], i.e. the structure of the host system, is modeled by a film of six quintuple layers of Bi_2Te_3 oriented in the (111) direction, as it is shown in Fig. 5.3(a), including nine vacuum layers on top and bottom to ensure a proper embedding into the vacuum, i.e. 78 atomic layers in total. Each quintuple layer is consisted of three Te and two Bi atoms, and five empty spheres placed between Te and Bi layers [3]. The atoms in the quintuple layer interact with strong covalent bonds, while the interactions between quintuple layers are of a weaker, Van der Vaals nature. The thickness of the film is chosen so as to ensure the robustness of the bulk band gap and the surface states.

Band structure

At first, we carry out calculations for the study of the band structure of Bi_2Te_3 for the surface crystal structure, in order to confirm the existence of its topological surface states. The surface energy bands structure of Bi_2Te_3 computed along the directions of the time reversal invariant momenta (TRIM) points of the first Brillouin zone, i.e. along $M \rightarrow \Gamma$ and $\Gamma \rightarrow K$ path is given in Fig. 5.4.

The topological insulator Bi_2Te_3 may be classified as a narrow-gap semiconductor, since a small band gap (< 1 eV) has been found in the study of its band structure. This is not the case in the surface, where the gap is closed by the conducting states created across the gap. According to our computations, as is presented in the resulting band structure diagram (Fig. 5.4), we observe the existence of a single Dirac cone around the Fermi level. The Dirac cone intersects the Γ high-symmetry point on the so-called Dirac

[3] Bi_2Te_3 is considered as an open structure, due to the large distance between neighboring quintuple layers. In systems like these, the Voronoi cell which is constructed around an atom may be present a large deviation from sphericity, that may affect the computed Green function within the KKR-based calculations. Because of this, empty spheres (with no nuclear charge), considered as "virtual atoms", are included to the unit cell in open systems in order to improve the sphericity of the Voronoi cells.

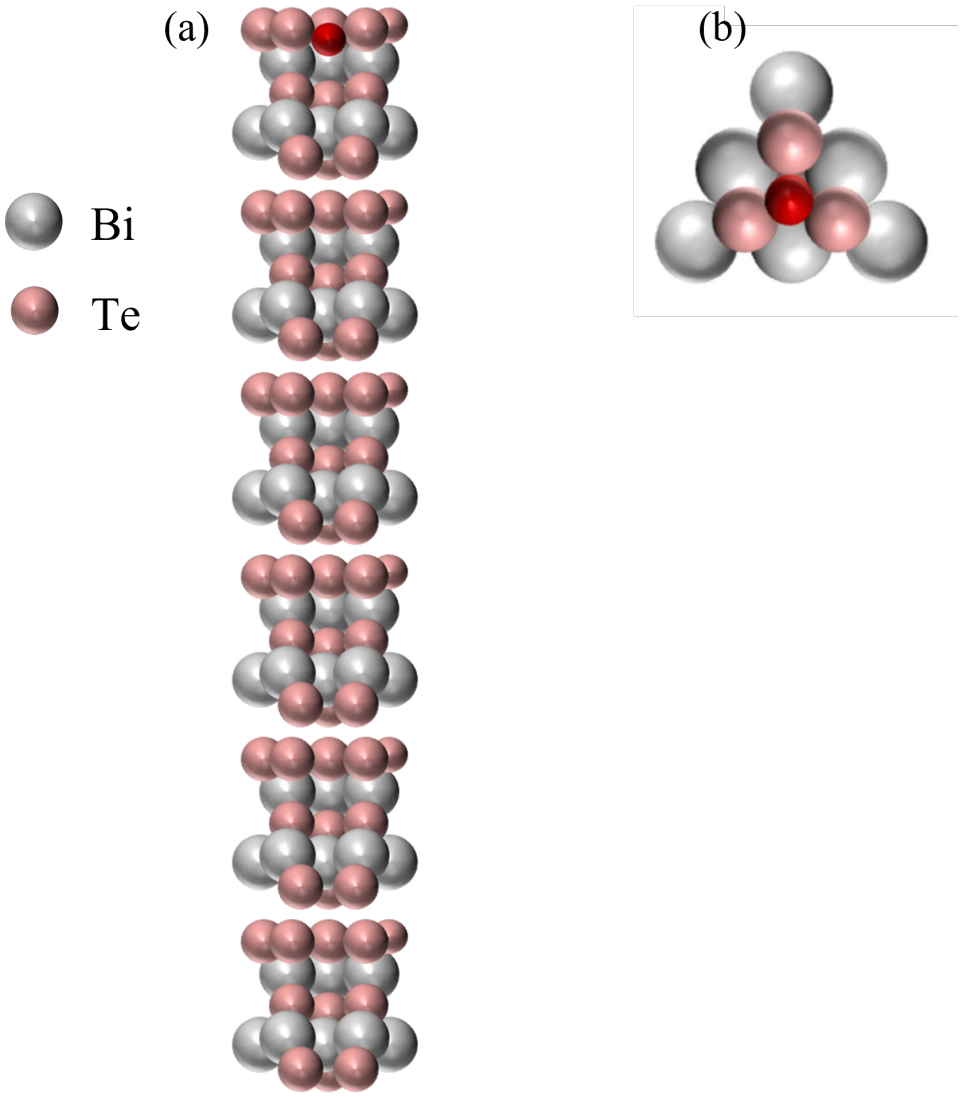

Figure 5.3: (a) Illustration of the first quintuple layer of Bi_2Te_3 in side-view and (b) top-view. The pink (medium-sized) and the gray (large) spheres represent the Te and Bi atoms, respectively. The magnetic impurity atom is depicted in red (small sized sphere). The impurity shows an inward relaxation with respect to the surface Te layer with vertical distance of 0.9Å, as has been found for Fe impurities by Eelbo et al. [84].

point, which, in the case of Bi_2Te_3, is within the bulk valence band, approximately 0.2 eV below the Fermi level. As expected from the bulk-boundary correspondence principle, conducting, metallic-like states are found in the surface.

We find that the dispersion of the Dirac cone is linear near the Γ point along Γ → K direction, whereas along Γ → M direction, a non-linear dispersion is shown. This non-linearity is observed because of the hexagonal warping effects in the Bi_2Te_3 Fermi surface [39].

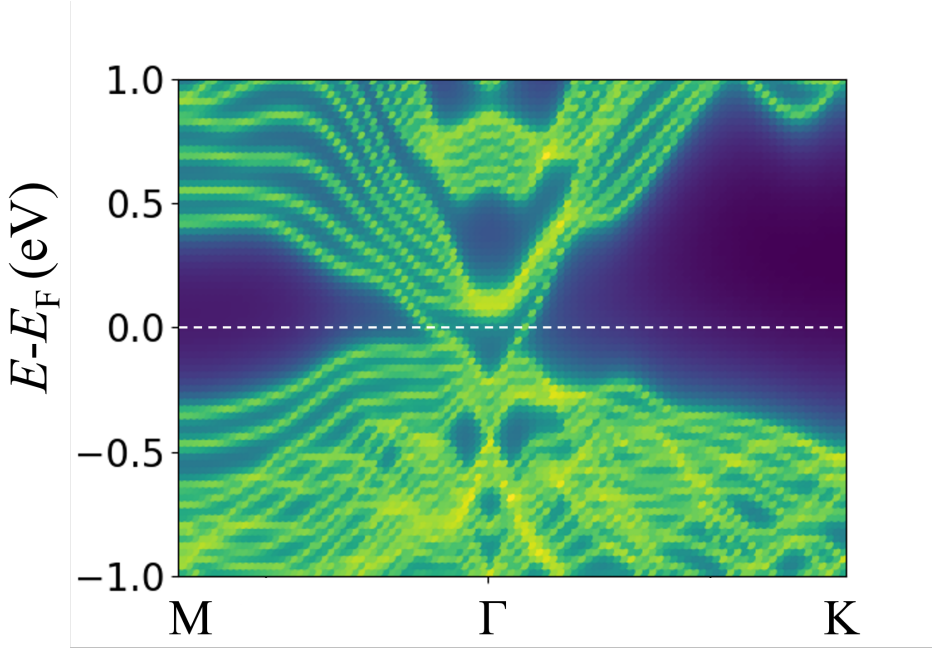

Figure 5.4: Surface-projected band structure of Bi_2Te_3 thick film along ΓM and ΓK directions. The Fermi level is $E_F = 8.6$ eV. [99]

Computational details

The density functional theory calculations for the electronic structure of the Bi_2Te_3 film were carried out with the Jülich full potential relativistic KKRhost code [100]. For the computation of the Green functions a finite angular momentum cutoff of $l_{max} = 3$ was assumed. The thickness of the film which is chosen such that, on the one hand it is thick enough to ensure the decoupling of the wavefunctions of electron states on the top and bottom surfaces, while on the other hand it is thin enough to be numerically manageable. It has been shown that the chosen thickness can give reliable results [98] by ab initio calculations. The Fermi level was firstly determined in the valence band, and is shifted into the middle of the band gap to correct the error caused by the truncation to the finite angular momentum cutoff ($l_{max} = 3$) in the calculations. The correction of the Fermi level was performed by applying Lloyd's formula [101, 102] for the convergence of

the final potential of the host system. The lattice constant of the host crystal structure, which is used, is a = 10.47 Å.

For the computation of the band structure diagram (Fig. 5.4), we used 100 energy points and 51 k-points along each direction, $\Gamma \to$ M and $\Gamma \to$ K.

5.4 Bi_2Te_3 with magnetic defects

Here, we consider the doping of the surface of Bi_2Te_3 [98] with magnetic transition-metal impurities. We study the four different defects systems Cr/Bi_2Te_3, Mn/Bi_2Te_3, Fe/Bi_2Te_3, and Co/Bi_2Te_3.

The impurity atoms are embedded in the interstitial position between the first Te and Bi layer, in fcc hollow site according to the experiments [84], as it is shown in Figs. 5.3(a,b), where the position of the defect in the first quintuple layer is shown from a side-view and in a top-view, respectively. In particular, the impurity position layer is shifted inward by 0.9Å with respect to the first Te layer [84]. For sure, in experiment, the exact position can change for different impurity types. This should have no qualitative consequences on our conclusions, which are related primarily to the simple form of the spin scattering of the Fermi-surface states, as we elaborate in the following Sections.

In the context given in Sec. 5.4.1, we consider two different defects concentrations in Bi_2Te_3 surface: 2%, corresponding to $N_{\text{def}} = 51$ defects, randomly placed within a disk of $N_{\text{disk}} = 2539$ positions (Fig. 5.5), and 5%, corresponding to $N_{\text{def}} = 51$ defects within a disk of $N_{\text{disk}} = 1027$ positions. A statistical averaging is achieved by considering $N_{\text{conf}} = 20$ different random configurations, which were generated by a random number generator. For comparison with the conventional Boltzmann formalism, we also calculate results using the scattering rate from a single defect (neglecting multiple scattering).

We take the defect magnetic moments to be perpendicular to the surface, in accordance to findings [82–84] for the Mn/Bi_2Te_3 and Fe/Bi_2Te_3 systems. Furthermore, we assume a ferromagnetic alignment of the magnetic defects, as has been observed experimentally at 2% concentration for Mn defects and at $> 3\%$ for Co defects [83]. The aforementioned assumptions have not been experimentally verified for all considered defect types at all concentrations (e.g., for Co, antiferromagnetic interactions appear at 2% concentration [83]). Extending the assumptions of out-of-plane orientation and ferromagnetism to all cases should be considered a numerical experiment. A qualitative argument for ferromagnetic interactions at not too low concentrations is that the Fermi wavelength in the Bi_2Te_3 surface is longer than the average distance between defects, so that the Ruderman-Kittel-Kasuya-Yosida (RKKY) interaction does not change sign. Moreover, we know from previous studies [83] that ferromagnetic interactions can be engineered by appropriate doping that shifts the Fermi level of the system and could conceivably be achieved in all four types of defects. Analogous engineering is conceivable for the magnetic anisotropy. In addition, by treating all types of defects on the same footing, we gain understanding of the chemical trends of the SOT mechanism.

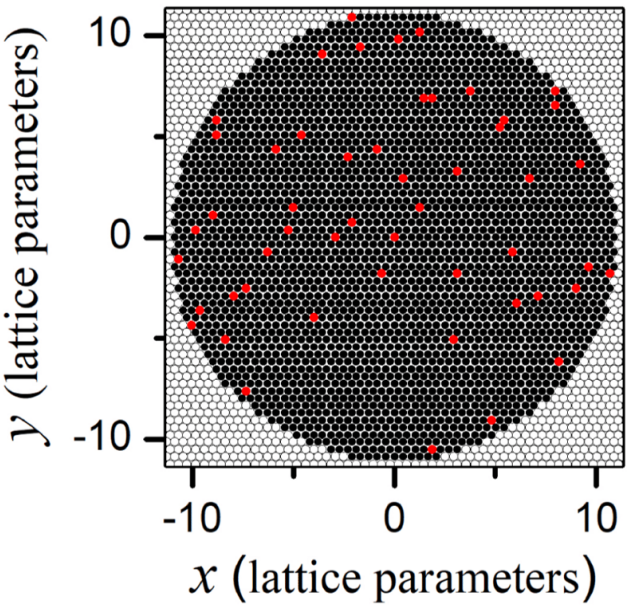

Figure 5.5: Schematic representation of the random positions of the defects on the surface in one of the random configurations. The filled red (gray-colored in gray-scale) circles represent the magnetic transition metal defects. The filled black and empty circles depict unoccupied surface impurity sites (threefold hollow positions with fcc stacking with respect to the surface layer), respectively inside and outside the disk in which the 51 impurities are embedded.

We carried out first-principles calculations for the impurity systems. The computed spin magnetic moments m_{at} of the impurity atoms are presented in Table 5.1. We find large spin magnetic moment for Mn and Cr impurities, while we observe a decrease for Fe and Co atoms. This result is in agreement with Hund's rule, as according to the electron configuration of Cr and Mn, they have half filled d-shells, while for Fe and Co are more than half-filled.

Impurity type	m_{at} (μ_B)
Cr	3.331
Mn	3.456
Fe	2.382
Co	1.027

Table 5.1: The computed spin magnetic moments m_{at} of the magnetic defects, embedded in Bi_2Te_3 surface.

The scattering process that will be discussed in following Sections, depends directly on the electronic structure of the impurity in the system. For this reason, we study the local density of states of the impurity atoms Cr, Mn, Fe and Co in Bi_2Te_3 surface, which is depicted in Fig. 5.6. The magnetic moment of the impurity atom is perpendicular to the plane of the surface. We observe that the majority-spin channel ($\uparrow$) is occupied for all impurity atoms. In contrast, the minority-spin channel ($\downarrow$) is partially occupied for Fe, and Co, while for Mn and Cr is unoccupied. We also find the Fe atom presents resonance at the Fermi level, that may affect the scattering process.

5.4.1 Multiple scattering and averaging over configurations

The Fermi wavevector in Bi_2Te_3 is of the order of $k_F \approx 0.2\text{Å}^{-1}$, which gives an estimated Fermi wavelength of $\lambda_F = 2\pi/k_F \approx 50\text{Å} \approx 12a_{\text{NN}}$, where $a_{\text{NN}} = 4.38\text{Å}$ is the nearest-neighbor distance in the surface. At the surface concentrations of 2% and 5%, that we wish to study, the average distance between impurities is of the order of $7a_{\text{NN}}$ and $4.5a_{\text{NN}}$. Clearly, many defects will be present within a radius of one wavelength around the impurity. Therefore, the approximation of independent impurity scattering, that is conventionally used in the Boltzmann equation, becomes questionable. In other words, the scattering rate $w_{\boldsymbol{kk'}}$ cannot be approximated by the rate of a single impurity, scaled by the concentration.

Hence, we take a different approach, that bears an analogy with the explicit supercell averaging used for SOT calculations in a Co/Pt bilayer (see Ref. [103]). We explicitly consider a collection of $N_{\text{def}} = 51$ defects, randomly placed within a circular disc of a radius of a few λ_F, while outside the disk we consider boundary conditions of the pristine host (see Fig. 5.5). The radius is adjusted so that the number of defects in the disk corresponds to the concentration. Formally, this collection is treated as a single super-impurity, for which the Green function G^{imp}, the scattering states (Eq. (2.66)) and the transition matrix (Eq. (2.78)) are calculated. The resulting scattering states and

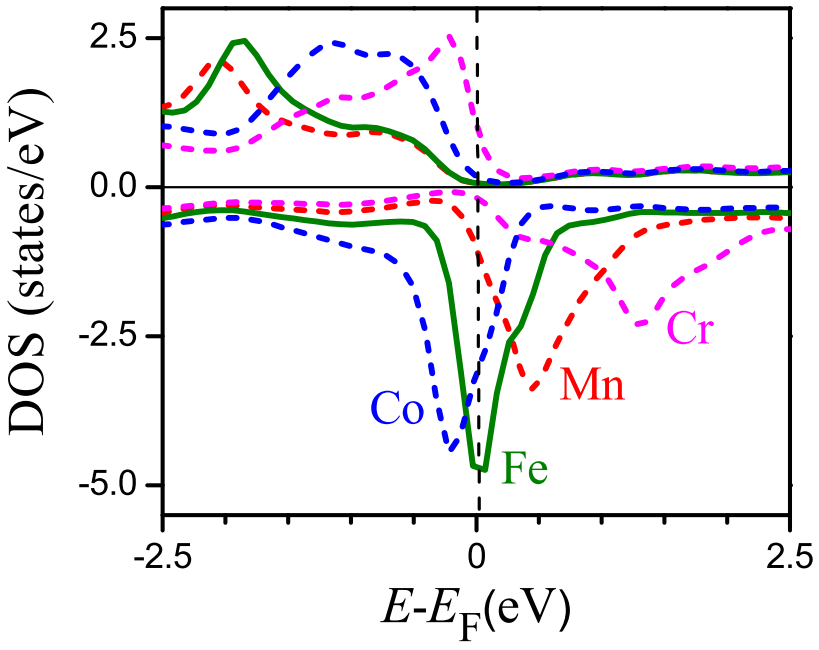

Figure 5.6: The local spin-resolved density of states (DOS) of the Cr, Mn, Fe and Co impurity atoms. The positive y axis corresponds to majority spin (↑) and the negative y axis to minority spin (↓).

scattering rate include the amplitudes and phases of all multiple scattering events off defects within this radius, summed to all orders. In a second step, the scattering rate is scaled by an appropriate concentration of super-impurities, so that the physically correct concentration of defects is matched. Thus, if c is the wished defect concentration, then the disk radius is adjusted to enclose $N_{\mathrm{disk}} = N_{\mathrm{def}}/c$ surface atoms. If the calculated scattering rate by the super-impurity of N_{def} atoms is $w_{\boldsymbol{kk'}}$, then we set a concentration of $x_{\mathrm{imp}} = c/N_{\mathrm{def}}$ in the Boltzmann equation (3.24)

$$(x_{\mathrm{imp}}\boldsymbol{\Lambda_k} \cdot \hat{n}_{\boldsymbol{\mathcal{E}}})N_{\mathrm{cr}} = \tau_{\boldsymbol{k}}\left[\boldsymbol{v_k} \cdot \hat{n}_{\boldsymbol{\mathcal{E}}} + N_{\mathrm{cr}} \sum_{\boldsymbol{k'}} w_{\boldsymbol{kk'}}(x_{\mathrm{imp}}\boldsymbol{\Lambda_{k'}} \cdot \hat{n}_{\boldsymbol{\mathcal{E}}})\right],$$

with N_{cr} the total number of atoms in the crystal. The problem of finding the Green function of a system with 51 defects poses no numerical difficulty (see Subsection 5.4.4).

In a third step, we calculate a number of $N_{\mathrm{conf}} = 20$ different random defects configurations, but always fixing one defect at the center of the disk. We consider this central defect as the most representative of the situation of a homogeneously doped surface. In the results we show the torque acting on the moment of the central defect only.

Computational details

The self-consistent potential of the single impurity atom was computed using the Jülich KKR impurity-embedding code KKRimp [69] in a cluster around the impurity including

the 14 nearest neighboring sites of the impurity for solving the Dyson equation, which is sufficient for the correct charge screening, due to the metallic surface states [4]. The calculations for the convergence of the potential were performed including the Lloyd's formula [101, 102]. In the calculations of the many impurities system, this converged impurity-atom potential is then placed in the respective 51 random impurity positions. This approximation saves computational time compared to a fully self-consistent calculation of the system of 51 impurities together. Tests have shown that the approximation is adequate for the description of the potential, if the impurities occupy farther than nearest-neighbour positions, which holds for the great majority of cases at low concentration. The multiply scattered wavefunction and the scattering rate for the spin-transport calculations (Sec. 5.5) are calculated in this way.

5.4.2 Validity of the independent scattering approximation

In order to investigate the validity of the independent scattering approximation, we analyze the inverse relaxation time $\tau_{\boldsymbol{k}}^{-1}$ (Eq. (3.21)), which represents the k-resolved scattering rate. Within the KKR method we can compute the scattering rate in terms of the T-matrix with the help of the Green functions, as mentioned in Chapter 2.4. By the integration of equation (2.77) over the Fermi surface, we obtain the inverse relaxation time of each state by the expression

$$\tau_{\boldsymbol{k}}^{-1} = 2\pi x_{\mathrm{imp}} N_{\mathrm{cr}} \frac{1}{\Omega_{\mathrm{BZ}}} \int_{\mathrm{FS}} d\boldsymbol{k}' |T_{\boldsymbol{k}'\boldsymbol{k}}|^2. \tag{5.5}$$

In this way, the approximation of independent scattering behind the Boltzmann equation is critically examined, by comparing the calculated scattering rate off single impurity versus multiple defects system. In Table 5.2 the ratio of the average scattering rate of the many defects system for the different configurations to the scattering rate of the single defect system is presented. We find that there is no linear scaling of the scattering rate with the number of impurities in the system. This is consistent with the observation that the Fermi wavelength is longer than the average distance between the impurities. Loosely speaking, after a scattering event of a wavepacket off a defect, there is not enough space for a new wavepacket to be formed, before it is scattered from another impurity. As a result, the consideration of the multiple scattering among impurities becomes important.

5.4.3 Simple model calculations

In addition, we examine the approach of the independent impurity scattering on the 3D topological insulators surface, investigating analytically and numerically the scattering off magnetic impurities on the surface. As it has been mentioned, the surface electrons

[4] Tests have been carried out for a larger cluster (considering up to the third shell of neighbors), as well as for a smaller cluster, considering the single-site approximation (taking into account no neighbors in the defect cluster), which has proven that the single-site limit is not enough [104].

Impurity type	$\tau_{51\text{imp}}^{-1}/\tau_{1\text{imp}}^{-1}$
Cr	141.3
Mn	248
Fe	68.5
Co	260.6

Table 5.2: The average scattering rate of the many impurities systems for the 20 different configurations $\tau_{51\text{imp}}^{-1}$ divided by the scattering rate of the single impurity system $\tau_{1\text{imp}}^{-1}$, in the presence of 2% defects concentration in the (Cr, Mn, Fe, Co)/Bi_2Te_3 systems. Within the independent scattering approximation, the ratio should be equal to 51.

are characterized by spin-momentum locking. Because of this, we apply a model based on $\boldsymbol{k}\cdot\boldsymbol{p}$ theory in order to calculate the relaxation time.

The surface states electrons on the surface Dirac cone of topological insulators, can be described by the following $\boldsymbol{k}\cdot\boldsymbol{p}$ Hamiltonian [39, 105].

$$H_0(\boldsymbol{k}) = v(\boldsymbol{k}\times\boldsymbol{\sigma})\cdot\hat{z}, \tag{5.6}$$

with the parameter v=2.55 eV·Å, taken from Ref. [39], which depends on the dispersion of the surface state. The spin matrices are replaced in Eq. (5.6) and the Hamiltonian is expressed as the following 2×2 matrix

$$H_0(\boldsymbol{k}) = v\begin{pmatrix} 0 & -ik_- \\ ik_+ & 0 \end{pmatrix}, \tag{5.7}$$

where the abbreviations $k_- = k_x - ik_y$ and $k_+ = k_x + ik_y$ have been used. Then, the eigenvalue problem

$$H_0\psi_{\boldsymbol{k}} = E_0\psi_{\boldsymbol{k}}, \tag{5.8}$$

with $\psi_{\boldsymbol{k}}^T = (w_1(\boldsymbol{k}), w_2(\boldsymbol{k}))$, can be solved. We find the following eigenenergies

$$E_\pm(\boldsymbol{k}) = \pm v\boldsymbol{k} \tag{5.9}$$

and the following eigenvectors

$$w_1(\boldsymbol{k}) = \frac{1}{\sqrt{2}}\begin{pmatrix} -ie^{-i\phi_k} \\ 1 \end{pmatrix}, \qquad w_2(\boldsymbol{k}) = \frac{1}{\sqrt{2}}\begin{pmatrix} ie^{i\phi_k} \\ 1 \end{pmatrix}, \tag{5.10}$$

where the angle $\phi_k = \tan^{-1}\frac{k_y}{k_x}$ is introduced, which is defined as the ΓK direction, i.e. represents the angle between the $\boldsymbol{k}$-vector and the $\hat{x}$-axis. The diagonalization of this Hamiltonian can be achieved applying the transformation from global to local spin frame, which is expressed in terms of the unitary ($U^\dagger = U^{-1}$) operator

$$\hat{U}_{\boldsymbol{k}} = \begin{pmatrix} \frac{1}{\sqrt{2}}ie^{-i\phi_{\boldsymbol{k}}} & -\frac{1}{\sqrt{2}}ie^{-i\phi_{\boldsymbol{k}}} \\ \frac{1}{\sqrt{2}} & \frac{1}{\sqrt{2}} \end{pmatrix}. \tag{5.11}$$

The knowledge of the eigenenergies allows us to write the Green function of the non-perturbing surface, in the local spin frame

$$G^{\text{host}}(\boldsymbol{k}; E) = \begin{pmatrix} (E + i0 - E_+(\boldsymbol{k}))^{-1} & 0 \\ 0 & (E + i0 - E_-(\boldsymbol{k}))^{-1} \end{pmatrix}. \tag{5.12}$$

Next, we consider the presence of an impurity on the topological insulator surface. The scattering off an impurity can be approximated by a δ-scatterer, considering a short-ranged scatterer [5]. The impurity Hamiltonian H_{imp} contains a scalar part V_0, which describes the scattering strength of the scattering center, and a magnetic part $\boldsymbol{m} \cdot \boldsymbol{\sigma}$ with $\boldsymbol{m}$ represents the relative strength of the impurity's magnetic moment.

$$H_{\text{imp}} = V_0[\mathbb{1} - \boldsymbol{m} \cdot \boldsymbol{\sigma}] \tag{5.13}$$

Using the unitary operator (5.11), the impurity Hamiltonian is transformed into the local spin frame of the host's electrons according to the relation $\hat{U}^{-1} H_{\text{imp}} \hat{U}$, where $\boldsymbol{\sigma} \parallel \hat{z}$. In the local spin frame the impurity Hamiltonian is given as

$$H_{\text{imp}} = V_0(\sigma_0 + m \cdot \sigma_x), \tag{5.14}$$

with $m = \boldsymbol{m} \cdot \hat{z}$. Thus, in the k-representation the impurity Hamiltonian is expressed as [65]

$$H_{\text{imp}}(\boldsymbol{k}, \boldsymbol{k}') = \int d\boldsymbol{r} V_0(\sigma_0 + m \cdot \sigma_x) e^{-i(\boldsymbol{k} - \boldsymbol{k}') \cdot \boldsymbol{r}}. \tag{5.15}$$

The knowledge of the Hamiltonian of the perturbed system and the Green function of the host system, as we discussed in Chapter 2.2, allows us to estimate the electronic properties of scattering off an impurity by the transition matrix (T-matrix):

$$T(\boldsymbol{k}, \boldsymbol{k}') = H_{\text{imp}}(\boldsymbol{k}, \boldsymbol{k}') + \sum_{\boldsymbol{k}'' \boldsymbol{k}'''} H_{\text{imp}}(\boldsymbol{k}, \boldsymbol{k}'') G^{\text{host}}(\boldsymbol{k}'', \boldsymbol{k}''') T(\boldsymbol{k}''', \boldsymbol{k}'), \tag{5.16}$$

which is computed in the iterative approach of a Born series

$$T = H_{\text{imp}} + H_{\text{imp}} G^{\text{host}} H_{\text{imp}} + H_{\text{imp}} G^{\text{host}} H_{\text{imp}} G^{\text{host}} H_{\text{imp}} + \cdots. \tag{5.17}$$

Finally, we can calculate the relaxation rate:

$$\tau_{\boldsymbol{k}}^{-1} = 2\pi \frac{1}{\Omega_{\text{BZ}}} \frac{1}{v} \int_{\text{FS}} d\boldsymbol{k}' |T_{\boldsymbol{k}'\boldsymbol{k}}|^2 \tag{5.18}$$

Numerical results

Eq. (5.18) for the computation of the inverse relaxation time is solved numerically and the results, which are presented in Fig 5.7, are compared with the corresponding findings

[5] We can consider a short-ranged scatterer, since the Fermi surface is close to the Brillouin zone center, i.e., the Fermi wavelength is quite long.

of the simulations based on KKR Green function method combined with Boltzmann formalism for the topological insulator Bi_2Te_3 with impurities on its surface (presented in Table 5.2).

The model calculations were performed for the k-points which correspond to the Fermi energy of the computed Bi_2Te_3 Fermi surface within KKR Green function method. A strong magnetic scatterer is considered, setting its strength of the magnetic moment $m = 2$. The T-matrix was calculated taking into account the first four terms of the Born series ($T = H_{\mathrm{imp}}+H_{\mathrm{imp}}G^{\mathrm{host}}H_{\mathrm{imp}}+H_{\mathrm{imp}}G^{\mathrm{host}}H_{\mathrm{imp}}G^{\mathrm{host}}H_{\mathrm{imp}}+H_{\mathrm{imp}}G^{\mathrm{host}}H_{\mathrm{imp}}G^{\mathrm{host}}H_{\mathrm{imp}}G^{\mathrm{host}}H_{\mathrm{imp}}$.)

In Fig. 5.7 the ratio of the scattering rate of a system with Nimp impurities to the scattering rate of a single impurity system as a function of the number of impurities (Nimp) on the surface, is shown. The impurities are randomly placed, as described in detail in the beginning of Section 5.4 with respect to the configuration of magnetic impurities in the Bi_2Te_3 surface. We observe that the dependence of scattering rate with the number of impurities in the system is not linear.

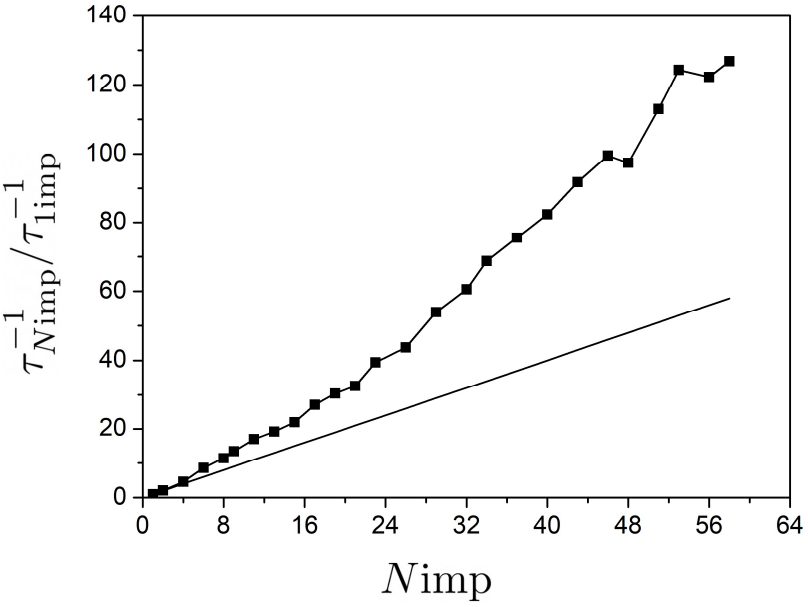

Figure 5.7: The scattering rate of a system with many impurities $\tau^{-1}_{N\mathrm{imp}}$ divided by the scattering rate of the single impurity system $\tau^{-1}_{1\mathrm{imp}}$, as a function of the number of impurities Nimp on the topological insulator surface. The solid straight line represents the expected linear scaling ($\tau^{-1}_{N\mathrm{imp}} = \tau^{-1}_{1\mathrm{imp}}N\mathrm{imp}$) of the independent scattering approximation.

As a result, we found reasonable qualitative agreement between the model calculations based on $\boldsymbol{k} \cdot \boldsymbol{p}$ theory with our findings based on Boltzmann formalism within KKR method, concerning the scattering rate off multiple impurities.

5.4.4 Numerical considerations on the Green function of the system with defects

The Green function of the impurity system is calculated in the KKR method by means of the algebraic Dyson equation

$$G_{LL'}^{\mathrm{imp,nn'}} = G_{LL'}^{nn''} + \sum_{n''L''L'''} G_{LL''}^{nn'}(t_{L''L'''}^{\mathrm{imp,n''}} - t_{L''L'''}^{n''}), G_{L'''L'}^{\mathrm{imp,n''n'}} \tag{5.19}$$

where n, n', n'' are atom-site-indices and $L, L', \ldots$ are indices combining the angular-momentum and spin of an atom at a site. $t(E)$ and $t^{\mathrm{imp}}(E)$ are the T-matrices of the host and impurity atoms, respectively. $G^{\mathrm{imp}}(E)$ is the unknown matrix for the Green function of the system with impurities and $G(E)$ is the known matrix of the host system. This linear set of equations has a dimension proportional to the number of sites for which $t_{L''L'''}^{\mathrm{imp,n''}}(E) \neq t_{L''L'''}^{n''}(E)$, i.e., to the number of defects. In this way the problem at hand becomes numerically tractable, since the number of defects (51) that we place in the disk results in a linear system of dimension $N_{\mathrm{def}} \times 2(l_{\max}+1)^2 = 1632$, where the number of spin and angular-momentum components at a cutoff of $l_{\max} = 3$ has been accounted for $[2(l_{\max}+1)^2 = 32]$.

5.5 Response coefficients to the electric field

We follow up our analysis, with the main purpose of this Chapter, the investigation of the linear response of the spin-orbit torque exerted on the magnetic moment of the impurity atoms embedded in Bi_2Te_3, under the application of an external electric field in the system.

For this study, we apply the KKR Green function method combined with the Boltzmann transport equation. The formalism which is used is given in details in Chapter 4. The development of the formalism is based on the work of Géranton et al. [16], who studied the spin-orbit torque effect on the atoms of the magnetic host system FePt/Pt. We extend this methodology to the spin orbit-torque effect on the impurity atoms. In particular, we perform the calculations for the impurity scattering wavefunctions $\psi_{\boldsymbol{k}}^{\mathrm{imp}}$ (Eq. (2.66)) instead of the host Bloch wavefunctions $\psi_{\boldsymbol{k}}$. In addition, the multiple scattering of electrons off impurities is included in our study.

In a first step, we find the states of the host system $\psi_{\boldsymbol{k}}$ on the Fermi surface, which obey the Bloch's theorem, making use of the KKR secular equation. Then, multiple scattering problem due to the existence of the impurities in the surface of Bi_2Te_3, is solved. Thus, the impurity scattering wavefunctions are determined by the Lippmann-Schwinger equation. The knowledge of the impurity wavefunctions on the scattering states on the Fermi surface, allows us to determine the expectation values of the spin

$\langle \sigma_{i\mu} \rangle_{\boldsymbol{k}}$ (Eq. (4.14)), torque $\langle \mathcal{T}_{i\mu} \rangle_{\boldsymbol{k}}$ (Eq. (4.19)) and spin flux $\langle \mathcal{Q}_{i\mu} \rangle_{\boldsymbol{k}}$ (Eq. (4.25)) based on the formalism outlined in Section 4.2.

In a second step, we investigate the scattering properties in the non-equilibrium state, considering the application of an external magnetic field in the system. Having solved the multiple scattering problem in KKR representation, first-principle calculations are performed for the solution of the self-consistent Boltzmann equation (5.4.1). Thus, by the determination of the mean free path combined with the calculated spin accumulation, spin-orbit torque and spin flux in the equilibrium state, we can compute the spin accumulation $\boldsymbol{\chi}$ (Eq. (4.32)), the spin-orbit torque $\boldsymbol{t}$ (Eq. (4.36)) and the spin flux $\boldsymbol{q}$ (Eq. (4.39)) in response to the application of an external electric field in the system, as analytically given in Section 4.3.

Fermi surface of Bi_2Te_3

The secular equation (2.58) is solved for the converged system of the topological insulator Bi_2Te_3 and its computed Fermi surface is shown in Fig. 5.8. We observe a hexagonal snowflake-shaped form of the Fermi surface, which has also been determined experimentally [38].

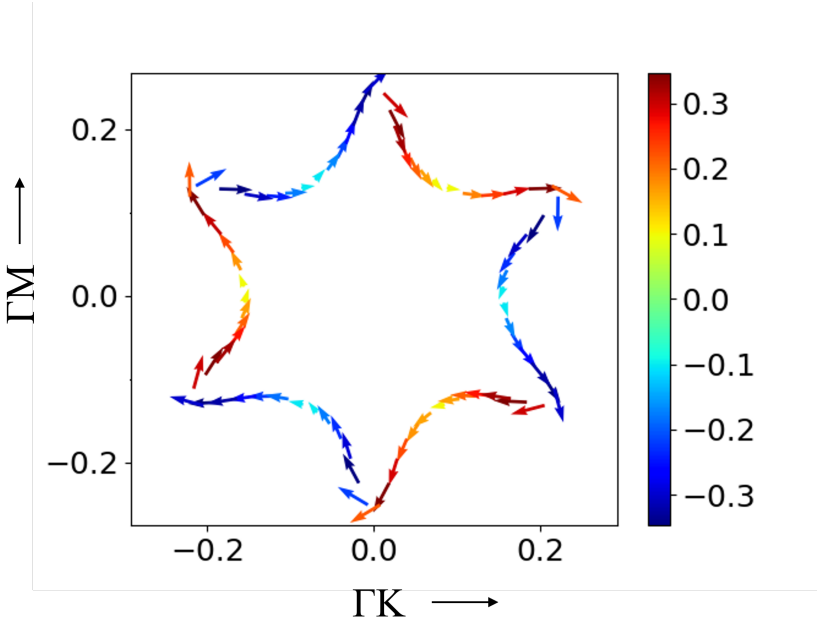

Figure 5.8: The spin-polarization of the Fermi surface states of Bi_2Te_3 film. The arrows represent the spin direction on the xy plane. The color code corresponds to the z component of the spin σ_z.

In Fig. 5.8 each arrow indicates the spin-polarization of each surface state. Each state is characterized by a certain spin-polarization, as there is no degeneracy on these metallic topological surface states. We observe that the rotation of the projection of electron spin, σ_x, σ_y, on xy plane is clockwise.

Spin-orbit torque

We follow up our analysis with the results of the spin-transport calculations. Here, the results of the tensor components in response to the electric field in y direction $\mathcal{E}_y$, which respects the reflection symmetry over the $y-z$ plane in the host structure, are presented. The corresponding results of the tensor components in response to the electric field in the x direction are omitted, since we found that the results do not change appreciably. Obviously, the z component of the torkance is zero, since the moments point along the z axis. Testing the simple, single-defect case, we found that the torkance is odd with respect to reversal of the impurity magnetic moment, i.e., the SOT is field-like. Thus, in the following, the response coefficients of the spin-orbit torque, the spin accumulation $\boldsymbol{\chi}$ and the spin flux $\boldsymbol{q}$, are investigated for the different impurities systems, Cr, Mn, Fe and Co in Bi_2Te_3 surface.

At first, we study the computed coefficient of the spin-orbit torque $\boldsymbol{t}$. In Fig. 5.9(a-d) each point represents the torque acting on the spin moment of the impurity atom. We examine the solution of the Boltzmann transport equation, within the approximation of the independent scattering approximation. We consider a single impurity atom in Bi_2Te_3 surface, neglecting the multiple scattering, which is depicted in Fig. 5.9(a-d) with black rectangular. We find that this system, the single impurity system is not representative in general, comparing the results of the single defect system with the corresponding results for the central atom of the many impurities system for the 20 different configurations (red circles), as it is shown in Figs. 5.9(a-d). This is anticipated, as the independent scattering approximation is not valid in this system, in other case the average torkance over the many impurities systems would correspond to the single impurity system (The detailed analysis can be found in Sec. 5.4.2). Instead, we observe that the torkance presents a spread for all different types of impurities systems. Comparing the different impurities systems, we also find that the largest value of the torkance is exerted on the Mn moment.

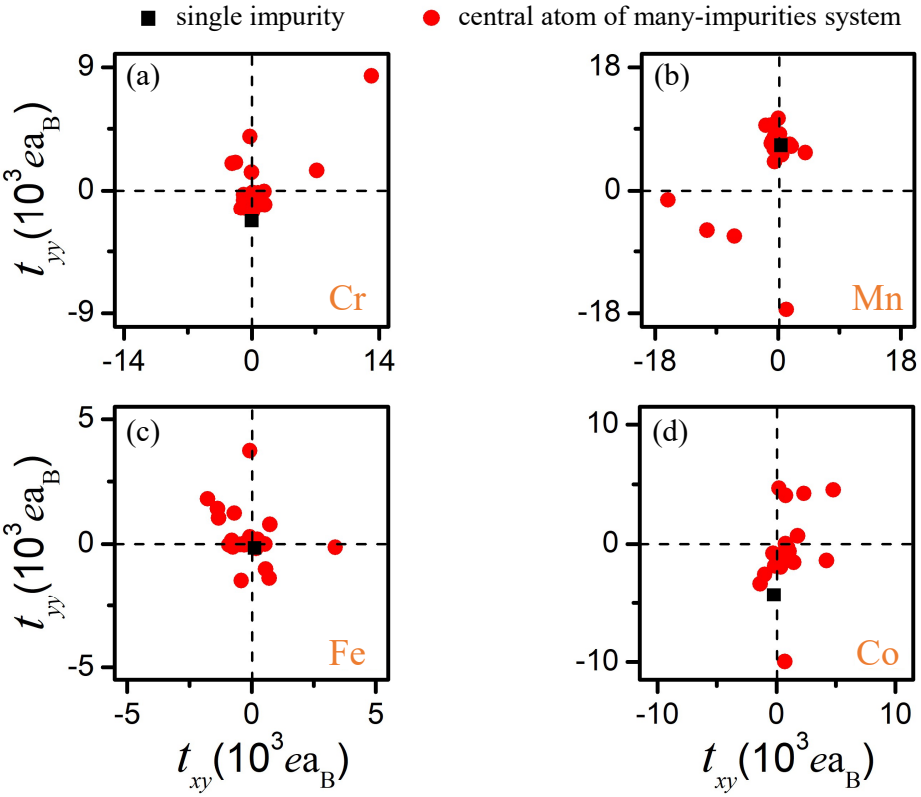

Figure 5.9: The y component of the torkance t_{yy} as a function of the x component of the torkance t_{xy}, on the central (a) Cr, (b) Mn, (c) Fe, and (d) Co impurity atom in the presence of 1 defect (black squares) and 2% defects concentration for 20 different distributions (red circles), embedded in Bi_2Te_3 surface. The results are scaled to a 2% concentration of defects. The electric field is taken in y direction. The torkance is given in units of $ea_B = 9 \times 10^{-5} \mu_B T/(V/cm)$.

Spin accumulation

In Figs. 5.10(a-d), the torkance versus the response coefficient of the spin accumulation is plotted. We observe that there is no linear dependence of the spin-orbit torque with the spin accumulation. Although, from simple models one might except a linear correlation between the spin of the conduction electrons and the spin-orbit torque, we find this absence of linear correlation due to the certain atom size. Because of this the torkance is calculated by a convolution involving one integral which includes the external product (see Eq. (4.19)), and it is not a product of the total spin and magnetic field.

Spin flux

In the following, the response coefficient of the spin flux is investigated, in order to examine if the current which enters in the impurity atomic sphere all contributes to create the torque. In Figs. 5.11(a,b,d) we observe that the torque has almost a linear dependence on the spin flux for the system of Bi_2Te_3 doped with Cr, Mn, and Co impurities. This demonstrates that the SOT exerted on the impurity moment is essentially mediated by spin currents in these systems, while the spin-lattice contribution due to the spin-orbit coupling in the impurity atomic sphere is negligible. On the contrary, there is still a correlation between the SOT and the spin flux, but not as strong as the other impurities systems, as it is shown in Fig. 5.11(c), as a result the spin-lattice interaction is significant on the Fe impurities system. The latter indicates that in the Fe/Bi_2Te_3 system a part of the current contributes to the spin precession of the Fe impurity, while the rest is lost to the spin-lattice interaction. From the density of states (DOS) of the impurity atoms (Fig. 5.6), it is observed that the Fe impurity presents a resonance exactly on the Fermi level, whereas the resonance of the other impurity atoms (Co, Mn, Cr) is somewhat shifted with respect to the Fermi level. Therefore, a longer delay time [68] of the scattered conduction electron in the Fe system is expected. The Wigner delay time t_{D} determines the time that the electron interacts with the impurity atom during the scattering process before it leaves the impurity again, i.e. describes the delay of the scattered wave compared the unperturbed, and is defined by the following equation [71]

$$t_{\mathrm{D}} = 2\frac{d\delta_l}{dE}, \tag{5.20}$$

where δ_l is the phase shift. Thus, we find that the electron interact a longer time with the spin-orbit field of the nucleus. As a consequence, there is a strong interaction of the spin with the lattice in the Fe/Bi_2Te_3 system.

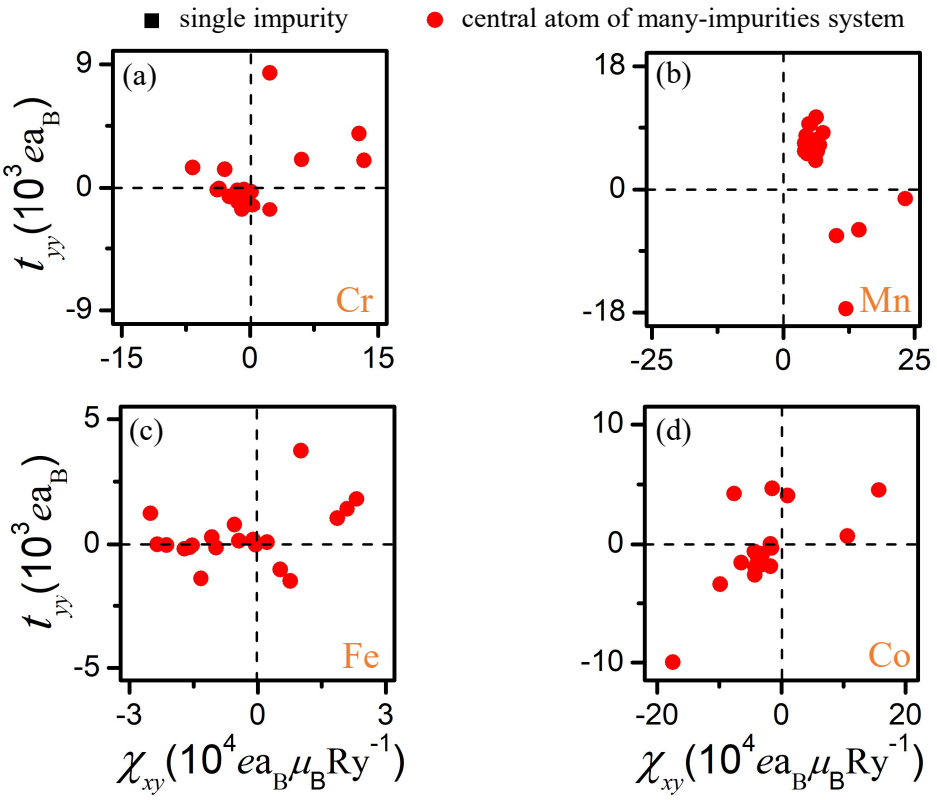

Figure 5.10: The y component of the torkance t_{yy} as a function of the response coefficient of the spin accumulation χ_{xy} on the central (a) Cr, (b) Mn, (c) Fe, and (d) Co impurity atom in the presence of 1 defect (squares) and 2% defects concentration for 20 different distributions (circles), embedded in Bi_2Te_3 surface. The results are scaled to a 2% concentration of defects. The electric field is taken in y direction. The torkance is given in units of $ea_B = 9 \times 10^{-5} \mu_B T/(V/cm)$. The spin accumulation is given in units of $ea_B \mu_B Ry^{-1} = 3 \times 10^{-10} \mu_B/(V/cm)$.

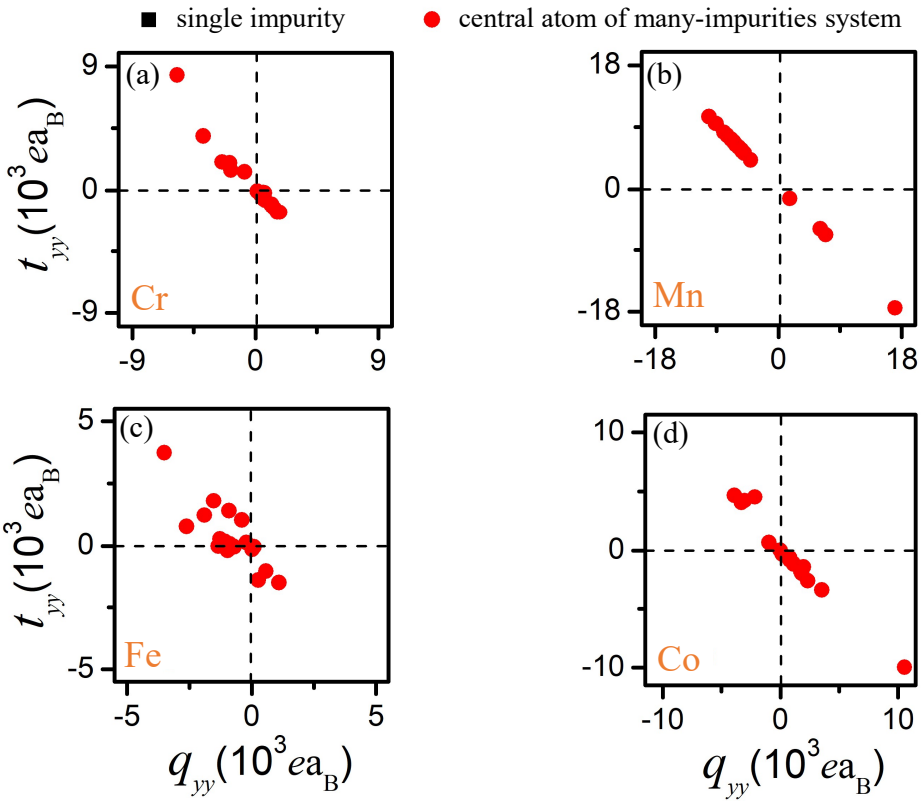

Figure 5.11: The y component of the torkance t_{yy} as a function of the response coefficient of the spin flux q_{yy}, on the central (a) Cr, (b) Mn, (c) Fe, and (d) Co impurity atom in the presence of 1 defect (squares) and 2% defects concentration for 20 different distributions (circles), embedded in Bi_2Te_3 surface. The results are scaled to a 2% concentration of defects. The electric field is taken in y direction. The torkance and the spin flux are given in units of $ea_B = 9 \times 10^{-5} \mu_B T/(V/cm)$.

Systems with different impurities concentration

Next, we compare the results of the systems with 2% and 5% defects concentration, in order to find how the impurities concentration affects the spin, the spin-orbit torque, and the spin flux. The absolute response coefficients of the averaged spin-orbit torque t, the spin flux q, and the spin accumulation χ in an applied electric field $\mathcal{E}_y$, determined as

$$t = \frac{\sum_i t^i}{i}, \quad t^i = \sqrt{(t^i_{xy})^2 + (t^i_{yy})^2} \tag{5.21}$$

$$q = \frac{\sum_i q^i}{i}, \quad q^i = \sqrt{(q^i_{xy})^2 + (q^i_{yy})^2} \tag{5.22}$$

$$\chi = \frac{\sum_i \chi^i}{i}, \quad \chi^i = \sqrt{(\chi^i_{xy})^2 + (\chi^i_{yy})^2}, \tag{5.23}$$

where i represents the configuration, are presented for the two different defect concentrations in Fig. 5.12. Comparing Figs. 5.12(a) and 5.12(b), we find that the magnitude of the torkance, the spin flux and the spin accumulation is greater in the case of the lower concentration 2% for all types of impurities. This observation is consistent with the fact that a lower concentration leads to a less perturbed topological surface state. This case is closer to the ideal situation, where the electron states incident on the defects have their spin in-plane, perpendicular to the defect magnetization, and produce maximal torque. We also observe that the Mn/Bi_2Te_3 system displays the largest torkance at both concentrations, in agreement with the results of Fig. 5.9. The lowest torkance is found in the Fe/Bi_2Te_3 system, for which we expect the strongest resonant scattering.

Important quantities for practical applications

For practical applications we are also interested in the time needed for a reversal of the impurity moment direction. We can estimate this by means of the angular rotation velocity per unit electric field which normalises the torkance to the impurity moment modulus m_{at}:

$$\begin{aligned} \omega &= \frac{1}{\mathcal{E}}\dot{\theta} \\ &= \frac{2\mu_B}{\hbar m_{\mathrm{at}}} t. \end{aligned} \tag{5.24}$$

Moreover, having computed the conductivity tensor, according to Eq. (3.28), we can find the longitudinal resistivity of the impurity atoms, in the application of an electric field in y-direction. This is calculated as the inverse of the conductivity tensor, i.e., $\rho_{yy} = \sigma^{-1}_{yy}$. By the knowledge of the torkance and the resistivity, the torque for a given current density j_y can be derived. We define the linear-response coefficient

$$\begin{aligned} \tilde{t} &= \frac{T}{j_y} \\ &= t \cdot \rho_{yy}. \end{aligned} \tag{5.25}$$

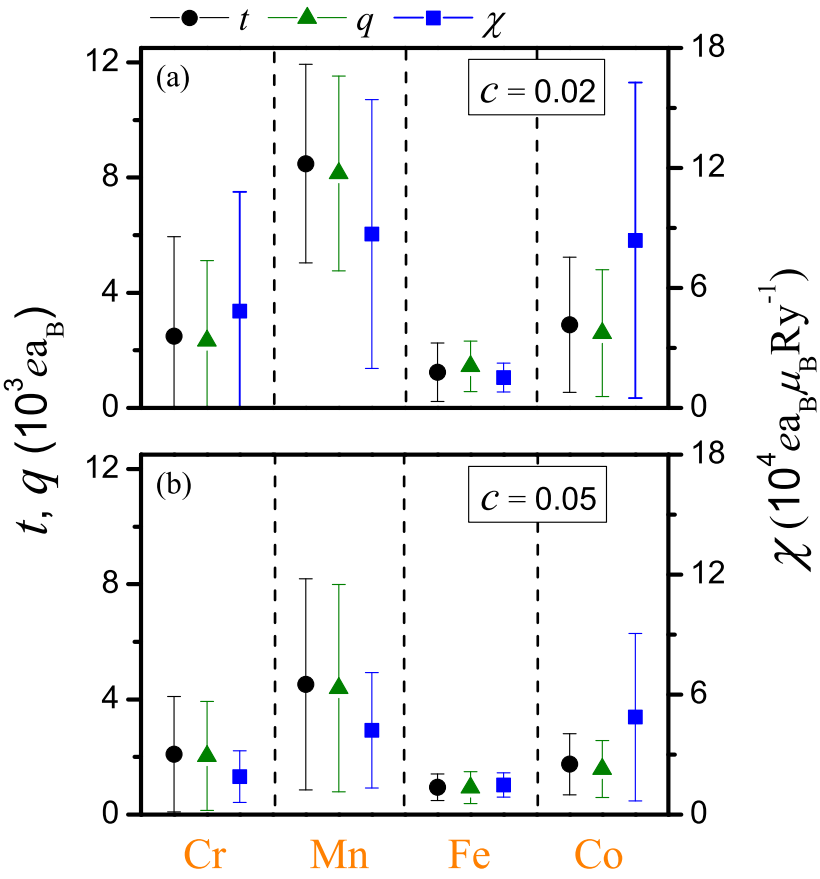

Figure 5.12: (a) The average torkance t (circles), spin flux q (triangles) and spin accumulation χ (squares) on the central atom in the presence of 2% and (b) 5% concentration of Cr, Mn, Fe, and Co impurities embedded in the Bi_2Te_3 surface. The values are averaged over the 20 different configurations and the error bars indicate the standard deviation of the values.

In the above equation (5.25) we have used the definition of the SOT (4.35) and Ohm's law (3.26), from the first to the second line. This quantity $\tilde{t}$ is important, because its knowledge serves two purposes. First, it promotes the viewpoint of the torque resulting as a response to the current, instead of the electric field. This picture is convenient especially in magnetic-impurity systems: we have the spin of the current-carrying electronic states of the host, on the one hand, and the electronic and magnetic structure of the impurity, on the other hand. The interaction of the two, due to spin scattering, produces the torque. The electric field does not enter the above picture, even though in reality it is the cause of the current.

The second purpose of introducing $\tilde{t}$, is that its product with the torkance, $(\tilde{t}\,t)$, is related to the Joule heat produced per unit time and volume, $\dot{Q}$, in order to achieve a given torque value T:

$$\dot{Q} = \rho_{yy}\, j_y^2 \tag{5.26}$$

$$= \frac{T^2}{\tilde{t}\,t}. \tag{5.27}$$

The Eq. (5.26) represents the Joule's first law, according to which the Joule heating, i.e., the power of heating generated by a conductor, is expressed in terms of its resistance ρ_{yy} and current j_y. The equation (5.27) was obtained using the Ohm's law (3.26) and the definition of the linear response of the torque (4.35). What we calculate here is actually a lower bound to the Joule heat, assuming that the magnetic-impurity scattering is the dominant source of resistivity.

The results of the resistivity (ρ_{yy}), the ratio of the SOT to the current density ($\tilde{t}$), and the rotation velocity (ω) for Cr, Mn, Fe and Co impurity atoms are depicted in Fig. 5.13. One can easily observe that the Mn/Bi_2Te_3 system presents the lowest resistivity, a large spin-orbit torque for a given current, and large rotation velocity. In this system the magnetic moment of the Mn impurity atom is the largest, compared to other impurity types systems (Table 5.1). As a consequence, this system is optimal for applications. Although a large torque for a given current is calculated in the Fe/Bi_2Te_3 system, this system presents the largest resistivity due to the resonant scattering of the Fe atoms, rendering it less optimal for applications.

The factor $\langle(\tilde{t}\,t)^{-1}\rangle$, averaged over the 20 configurations, is presented in Table 5.3. We find that the Joule heat for a given spin-orbit torque is much smaller in Mn/Bi_2Te_3 than the other impurity types systems, that results in fastest and energetically most efficient switching, i.e., has the lowest resistivity and the Joule heat production.

Impurity type	$\langle(\tilde{t}\,t)^{-1}\rangle$ (S/($e^2 a_B^2$))
Cr	2497.407
Mn	51.207
Fe	1160.321
Co	175.831

Table 5.3: The computed Joule heat factor $\langle(\tilde{t}\,t)^{-1}\rangle$ of the magnetic defects.

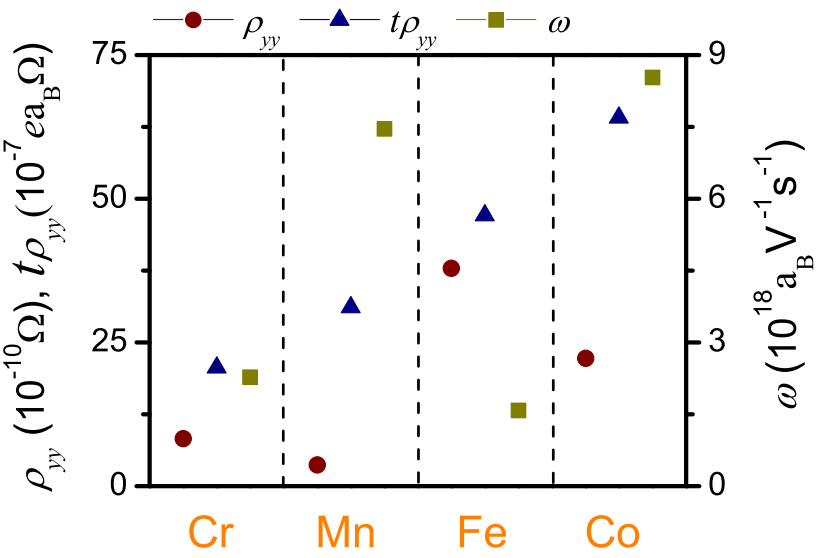

Figure 5.13: The resistivity ρ_{yy} (circles), the torkance on the central impurity atom multiplied by the resistivity $\tilde{t} = t\rho_{yy}$ (Eq. (5.25)) (triangles), and the angular rotation velocity ω per unit electric field (Eq. (5.24)) (squares), averaged over the 20 different configurations, in the presence of 2% defects concentration in the (Cr, Mn, Fe, Co)/Bi_2Te_3 systems. The electric field is taken in y direction.

Computational details

The self-consistent potential of the host system and the potential of the impurity atoms, that is found as described in previous Sections, are used for the solution of the scattering problem on the Fermi surface states, performing first-principles calculations with the JuKKR-KKRhost code [100]. The calculations for the expectation values of the spin, spin-orbit torque and spin flux on impurity atoms, in the absence of an electric field on the system, are also carried out with the modified JuKKR-KKRhost code.

The calculations for the charting of Fermi surface and the Boltzmann transport computations were performed with the highly parallelized JuKKR-PKKR code [79]. The existing code was improved, to include the calculations of the response coefficients of the spin, spin-orbit torque, and spin flux on the impurity magnetic moment. For these calculations 78 k-points in the full Fermi surface of Bi_2Te_3 were used, which is adequate, since the FS consists of only a single closed loop near the center of the Brillouin zone surface.

6 Magnetic skyrmions in Pd/Fe/Ir(111)

6.1 Introduction

The first theoretical prediction of magnetic skyrmions came about twenty years ago [106, 107] in ferromagnetic materials in the B20 structure [107], while a few years later they were experimentally detected [49, 108]. Concerning technological applications, significant attention is given to two-dimensional skyrmions in thin ferromagnetic layers deposited on heavy metal substrates [41, 109].

The unique properties of magnetic skyrmions make them very promising for applications in spintronic devices. They have nanoscale size, ideally the skyrmions used in applications should be individual small skyrmions of $\simeq$ 10nm size at room temperature. Another special characteristic of skyrmions is that they are topologically protected, as they cannot be continuously transformed into the ferromagnetic state by a rotation of the magnetization direction, while keeping the magnetization modulus constant. Because of this, stable skyrmions are expected even at small sizes above room temperature, making them ideally as carriers of information in future racetrack memory devices. In addition, their formation and their detection is possible, assisted by their non-coplanar texture.

Here, our target is the skyrmions formation in a transition-metal ferromagnetic (FM) layer on a heavy metal (HVM) substrate characterised by a strong spin-orbit coupling [46, 110]. In particular, we focus in the investigation of the electronic structure of small

magnetic skyrmions in the magnetic thin film Pd/Fe/Ir(111).

This Chapter is structured as follows. In Section 6.2 we give the theoretical foundation of magnetic skyrmions. An introduction on the topological nature of skyrmions and the theoretical model which can describe the skyrmion formation is presented. The electronic structure of Pd/Fe/Ir(111) system is studied in Section 6.3, as this film will be used as the host system in our calculations for the skyrmions formation. The effect of the breaking of time-reversal symmetry in the Fe/Ir interface is also discussed, and the Fermi surface of this system, in which spin transport properties can be investigated, is presented. Finally, we present the results of our ab-initio simulations for the formation of stable magnetic skyrmions of different sizes in Pd/Fe/Ir(111) film in Section 6.4.

6.2 Introduction to magnetic skyrmions

The magnetic skyrmion is a spin texture, which is formed in the midst of a ferromagnetic state by a swirl of the magnetization direction toward a center, where the magnetization takes an opposite direction to the ferromagnetic surroundings and is separated from them by a circular domain wall (Fig. 6.1). This topologically non-trivial spin texture, that behaves like a particle, is localized in space. Due to its topological protection, the skyrmion cannot be transformed to a different magnetic state (e.g., to the ferromagnetic state) by continuous rotations of the magnetization rotation field. For the transition to the ferromagnetic state, skyrmions need to overcome a high energy barrier. Because of this, skyrmions are described as stable magnetic excitations and are also called 2-dimensional topological solitons.

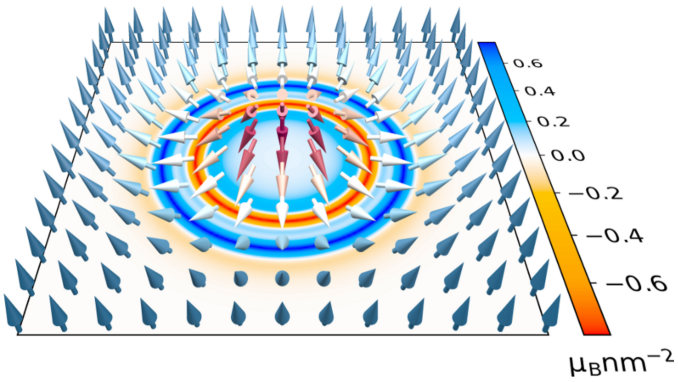

Figure 6.1: Schematic representation of a magnetic skyrmion formed by a swirl of the magnetization on a ferromagnetic state. Figure from Lux et al. [111].

Skyrmion Topology

The topological nature of skyrmions is defined by the topological charge Q_{sk} (also called skyrmion number) [109], which is a measure of the winding of the normalized local magnetization, $\boldsymbol{m}$. The different types of magnetic skyrmions, which are characterized

by different spin structures, can be classified based on their topological nature. The topological charge Q_{sk} is found according to the relation [112, 113]

$$Q_{\mathrm{sk}} = \frac{1}{4\pi} \int \boldsymbol{m}(\boldsymbol{r}) \cdot \left(\frac{\partial \boldsymbol{m}(\boldsymbol{r})}{\partial x} \times \frac{\partial \boldsymbol{m}(\boldsymbol{r})}{\partial y} \right) \mathrm{d}^2 r. \tag{6.1}$$

The integration is performed over the area of the skyrmion and the unit vector $\boldsymbol{m}$, which points towards the direction of the local magnetization can be expressed in spherical coordinates according to the symmetry of the skyrmion. It is written in terms of the polar angle θ and the azimuthal angle ϕ, $\boldsymbol{m} = (\sin\theta\cos\phi, \sin\theta\sin\phi, \cos\theta)$, and the vector $\boldsymbol{r}$ is expressed in polar coordinates $\boldsymbol{r} = r(\cos\alpha, \sin\alpha)$. Then, the topological charge takes the form

$$\begin{aligned} Q_{\mathrm{sk}} &= \frac{1}{4\pi} \int_0^{\infty} \mathrm{d}r \int_0^{2\pi} \mathrm{d}\alpha \frac{\partial\theta(r)}{\partial r} \frac{\partial\phi(\alpha)}{\partial\alpha} \\ &= -\frac{1}{2} \cos\theta(r)\Big|_{r=0}^{\infty} \cdot \frac{1}{2\pi}\phi(\alpha)\Big|_{\alpha=0}^{2\pi}. \end{aligned} \tag{6.2}$$

Thus, the integral is simplified to a product of the polarity p, which defines the reversion of the out-of-plane magnetization of a skyrmion comparing to its center, with the vorticity v that determines the wrap of the angle [114]

$$Q_{\mathrm{sk}} = p \cdot \mathrm{v}. \tag{6.3}$$

Therefore, the topological charge takes only integer numbers for different types of skyrmions, i.e., $Q_{\mathrm{sk}} = \pm 1, \pm 2, \ldots$

As an example, for the skyrmion depicted in Fig. 6.1 the vorticity is $\mathrm{v} = +1$ and the polarity $p = -1$, corresponding to the topological charge $Q_{\mathrm{sk}} = -1$, considering the ferromagnetic background parallel to the z-axis. The skyrmion which is shown in this Figure is called Néel-type skyrmion, and is mostly observed at interfaces [57, 110], favored by the interfacial Dzyaloshinskii-Moriya interaction of multilayers. There are numerous different configurations of magnetic skyrmions, however, the most widely existing are Néel- and Bloch-type skyrmions. Bloch skyrmions are typically found in bulk materials and are characterized by the same topological charge as Néel-type, $Q_{\mathrm{sk}} = -1$. The Néel-type is distinguished by the Bloch-type skyrmions according to the progression of magnetization across the diameter, which is cycloidal in Néel (Fig. 6.2(a)), while at the Bloch skyrmion is helical (Fig. 6.2(b)). Another well-known skyrmion category is the antiskyrmions [115], with opposite skyrmion number, $Q_{\mathrm{sk}} = 1$.

Skyrmion description

The underlying mechanism for the skyrmion formation is a competition between three types of interactions, a ferromagnetic interaction between atomic spins, an anisotropic Dzyaloshinskii-Moriya (DM) interaction promoting an angle of 90° between them, and a magneto-crystalline anisotropy developing an out-of-plane direction for the spins. Then, an atomistic spin-lattice model for the capture of skyrmion formation can be described by

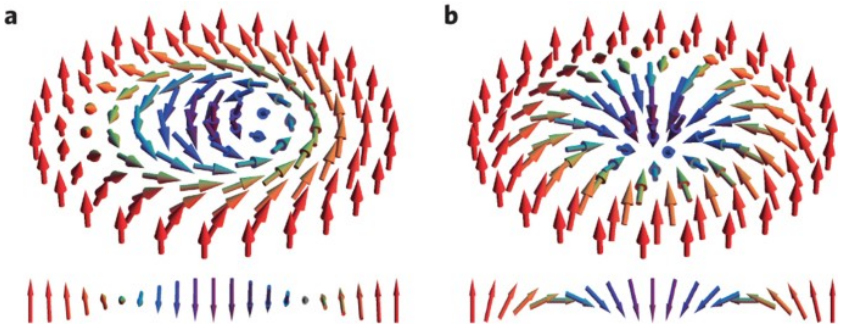

Figure 6.2: Schematic representation of (a) Néel and (b) Bloch skyrmion. Fig. from Kézmárki et al. [116].

the following spin Hamiltonian [49, 108], consisting of the Heisenberg exchange interaction, the DM interaction, the magnetic anisotropy and an external magnetic field term:

$$H = -\sum_{ij} J_{ij}\boldsymbol{m}_i\boldsymbol{m}_j - \sum_{ij} \boldsymbol{D}_{ij}(\boldsymbol{m}_i \times \boldsymbol{m}_j) - \sum_{i} \boldsymbol{m}_i \cdot \boldsymbol{K}_i \cdot \boldsymbol{m}_i - \sum_{i} \boldsymbol{B}_{\text{ext}}\boldsymbol{m}_i + \cdots \quad (6.4)$$

Here, $\boldsymbol{m}_i$ and $\boldsymbol{m}_j$ represent the atomic magnetic moments at sites i and j, respectively. The parameter J_{ij} is the symmetric Heisenberg exchange that aligns the spins in parallel, $\boldsymbol{D}_{ij}$ is the Dzyaloshinskii-Moriya (DM) interaction vector which gives a tendency for the perpendicular mutual orientation of spins and can be considered as an antisymmetric exchange interaction, i.e., $\boldsymbol{D}_{ij} = -\boldsymbol{D}_{ji}$. $\boldsymbol{K}_i$ is the on-site single-ion anisotropy constant, and $\boldsymbol{B}_{\text{ext}}$ is an external magnetic field. The easy axis (z-direction) is assumed to be out-of-plane in thin magnetic films. The ellipsis at the end of Eq. (6.4) stands for possible higher-order terms that may be needed, such as the four-spin interaction [110]. These parameters define the skyrmion size and its stability.

In many cases, such as in our studied system, the magnetic anisotropy, as well as the external magnetic field are not essential interactions for the skyrmion formation, in contrast with the DM interaction, which is necessary condition for the skyrmion stability. This interaction is responsible for the existence of the high energy barrier, that favors the formation of stable skyrmions. The DM interaction is caused by the spin-orbit interaction under a broken inversion symmetry, because of this it arises in ferromagnets on top of a heavy metal [117–119]. The strength of the energy barrier depends on the material and the interactions, nevertheless in a realistic case it can be about 40 meV [120]. As a consequence, the formation of stabilized skyrmions is expected even at room temperature in many systems. The lifetime of a skyrmion, i.e., its formation-annihilation rate, according to which the stability of the skyrmion can be controlled, at a finite temperature for an energy barrier ΔE can be found according to Arrhenius law $\tau \sim \tau_0 \exp\left(\frac{\Delta E}{k_B T}\right)$.

Because of their magnetic texture, skyrmions can be also described by a micromagnetic model. Considering the simplest case, in which only the Heisenberg exchange and the DM interactions contribute to the stabilization of skyrmions, the energy functional is

written in the form

$$E(\boldsymbol{m}) = \int_{R^2} d\boldsymbol{r} \Big[J|\nabla \boldsymbol{m}|^2 + \boldsymbol{D}[\boldsymbol{m}(\nabla \cdot \boldsymbol{m}) - (\boldsymbol{m} \cdot \nabla)\boldsymbol{m}] \Big]. \tag{6.5}$$

According to Eq. (6.5) it becomes clear that the Dzyaloshinskii-Moriya interaction determines the preferred energy state of a material. Thus, the Néel-type skyrmions can be classified in two categories according to the handedness (or rotational sense). The first one Néel-type skyrmion is characterized by counter-clockwise magnetization rotation, which corresponds to positive sign of DM interaction ($D > 0$), while on the other type the whirling of the magnetization is clockwise, and the sign of the DM interaction is negative ($D < 0$) (Fig. 6.3).

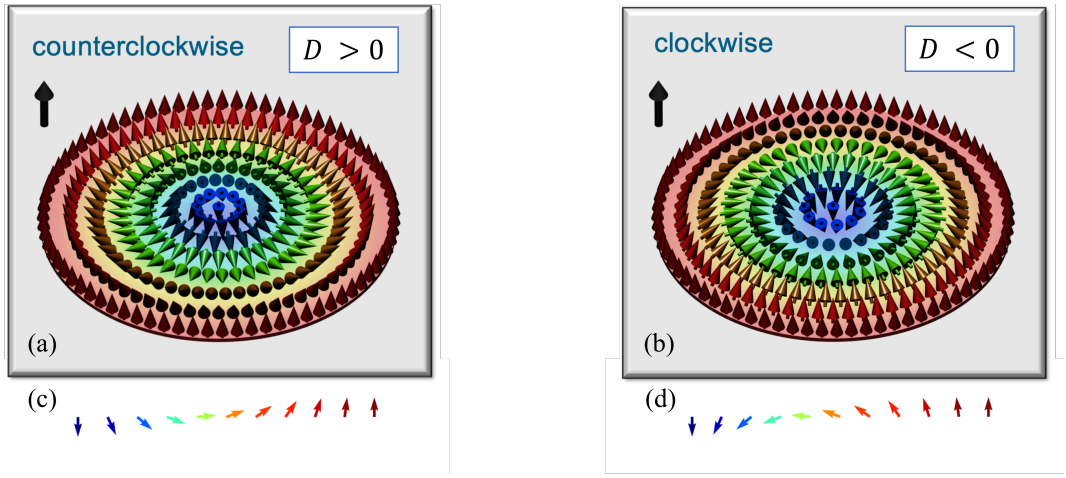

Figure 6.3: Néel-type magnetic skyrmion schematically shown with (a) a counterclockwise and (b) a clockwise spin rotation. (c,d) Cross sections of the spin textures of the magnetic skyrmions shown in (a), (b), respectively. Fig. adapted from [S. Blügel, *2D Materials for Spin-Orbitronics*, ICTP virtual meeting (2021)].

6.3 Electronic structure of Pd/Fe/Ir

At first, density functional theory calculations employing the full-potential relativistic Korringa-Kohn-Rostoker (KKR) Green function method including spin-orbit interaction [69, 100], were performed for the study of the electronic structure of the host system, the magnetic thin film heterostructure Pd/Fe/Ir(111), in which stable magnetic skyrmions will be formed.

Studied system

More specifically, the system is a magnetic thin film consisting of one atomic layer of ferromagnetic Fe, deposited on metallic, non-magnetic heavy metal Ir substrate, and

then covered by a monolayer of the magnetically susceptible Pd metal (Fig. 6.4(a)). This heterostructure is chosen for the magnetic skyrmions formation, as the Ir substrate provides the necessary strong spin-orbit coupling, which combined with the inversion-symmetry broken at the Fe/Ir(111) interface, leads to a large DM interaction $\boldsymbol{D}$ within the Fe layer. As it is mentioned in the previous Section 6.2, the DM interaction is precondition for the formation of stabilized skyrmions. The Pd metal layer on top of Fe/Ir(111) strengthens the Heisenberg exchange J. The size and the chirality of stabilized skyrmions depends on the conflict between the DM interaction and the ferromagnetic isotropic Heisenberg exchange interaction (Eq. (6.4)). This system has been well studied experimentally [46, 47, 121], as well as in simulations [57, 58], and has been shown that the formation of stabilized skyrmions is feasible.

In the host system, the atoms of Fe layer are in the ferromagnetic state, as it is illustrated in Fig. 6.4(b), and in a next step we carry out calculations for the relaxation of the magnetic moments in the non-collinear texture (Fig. 6.4(c)), achieving the skyrmion formation, as will be described in the following Section.

In Table 6.1, the computed electronic charge n, and the spin magnetic moment m_s of the near-surface layers of Ir, Fe and Pd are given. We find a large spin magnetic moment of Fe atom ($m_s = 2.53\mu_{\mathrm{B}}$). We also observe a non-negligible spin magnetic moment of Pd atom ($m_s = 0.29\mu_{\mathrm{B}}$). The spin moment is induced from Fe to Pd atom, because Pd is known as having a sizeable Stoner-enhanced susceptibility, thus it is easily polarized. The strength of the isotropic exchange constant J between the Fe atoms is significantly affected by the Pd layer. In particular, the absolute value of the constant J rises in this system, i.e., Pd favors the ferromagnetic state of Fe atoms.

	Z	n	m_s (μ_{B})
Ir	77	76.8	0.04
Fe	26	26.2	2.53
Pd	46	45.7	0.29

Table 6.1: The atomic number (Z), the computed electronic charge (n) and the spin magnetic moment (m_s) of the near-surface atomic layers of Ir, Fe and Pd, in the ferromagnetic state of Pd/Fe/Ir(111), within our first-principles calculations.

In Figs. 6.4(d-e), the fcc crystal structure of Pd/Fe/Ir(111) film is depicted in a perspective-view, and in a top-view, respectively. More specifically, the three layers represent the Pd layer, the Fe layer, and its nearest Ir layer. As it is shown in Fig. 6.4(e) the system presents 120° rotation symmetry, and 3 equivalent reflection planes perpendicular to the surface, depicted with dashed lines. For example, the $x = 0$ plane is a reflection plane, but the $y = 0$ plane is not, due to the fcc(111) structure. The absence of this reflection symmetry is expected to influence the electronic structure properties of the system.

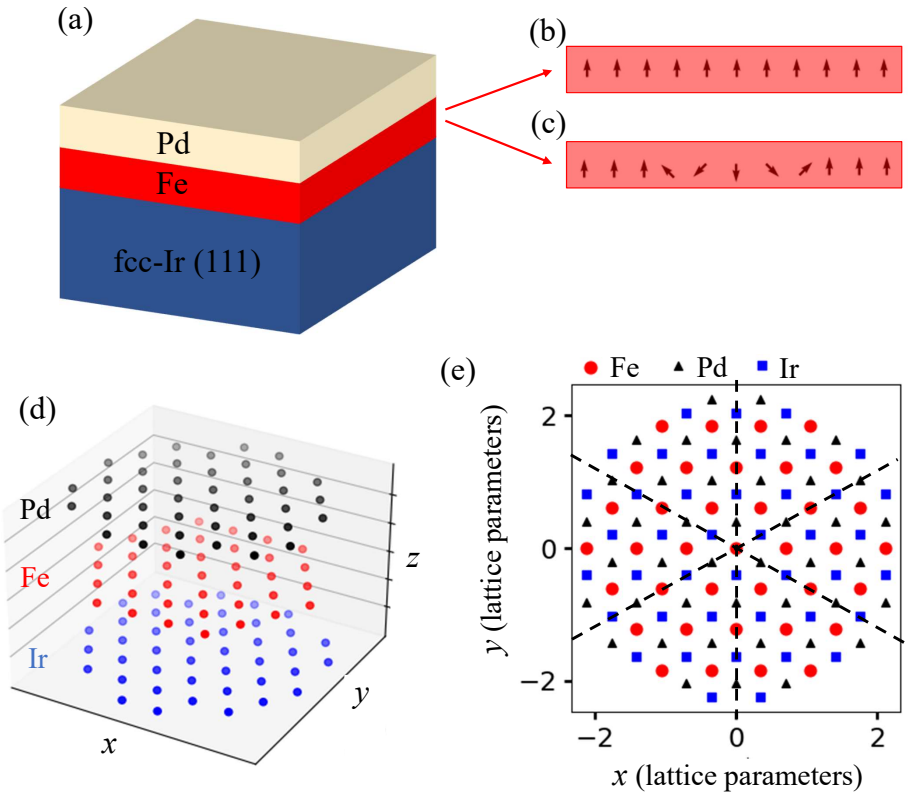

Figure 6.4: (a) Schematic representation of the heterostructure Pd/Fe/Ir(111). (b) Spin texture of atoms in Fe layer in the ferromagnetic state, and (c) in the non-collinear state, after the skyrmion formation. (d) Illustration of the crystal structure of the near-surface atomic layers of Pd/Fe/Ir(111) film in a perspective-view. The red, black, and blue circles represent the Fe layer, the above Pd layer and the below Ir layer, respectively. (e) Similar representation as (d) in a top-view. The red circles represent the sites of Fe atoms in the crystal, the black triangles the sites of Pd atoms and the blue rectangular depict the Ir atoms. The dashed lines show reflection planes perpendicular to the surface.

Band structure

We follow up our analysis, investigating the electronic properties of the host system. Regarding the band structure, we must consider some symmetries which, if present, enforce the relation $E_{\boldsymbol{k}} = E_{-\boldsymbol{k}}$. One such symmetry is time reversal symmetry, which is defined by the anti-unitary operator

$$i\sigma_y K = \begin{pmatrix} 0 & 1 \\ -1 & 0 \end{pmatrix} K,$$

where $i\sigma_y$ is a spin-flip operator and K is the operation of complex conjugation, $K\Psi = \Psi^*$ [122]. In ferromagnets, the spin-flip operation is absent, but if the spin-orbit coupling is absent, then the complex conjugation operation is present and is enough to enforce $E_{\boldsymbol{k}} = E_{-\boldsymbol{k}}$. In ferromagnets with spin-orbit coupling, also the complex conjugation is absent, but $E_{\boldsymbol{k}} = E_{-\boldsymbol{k}}$ is enforced if space-inversion is a symmetry of the system. In the present case, also space-inversion is absent, thus the relation $E_{\boldsymbol{k}} = E_{-\boldsymbol{k}}$ is expected to hold only in certain directions that are connected by reflection symmetry over a reflection plane.

In Fig. 6.5(a) the band structure of the states which are projected to spin down in the Fe layer of Pd/Fe/Ir(111) film is shown, in the high symmetry $\Gamma \to \mathrm{K}$ and $\Gamma \to -\mathrm{K}$ directions. We can observe that the energy bands in $\Gamma \to \mathrm{K}$ are not identical to the energy bands in $\Gamma \to -\mathrm{K}$ direction. This asymmetry is justified due to the coexistence of the spin-orbit interaction, magnetism, and lack of reflection symmetry about the $y = 0$ plane in the Fe/Ir(111) interface. The broken symmetry is also confirmed by the k-resolved density of states (DOS) at the Fermi energy in the corresponding directions in the Fe layer, as it is depicted in Fig. 6.5(b). As we discussed in the previous Section 6.2, the breaking of the $E_{\boldsymbol{k}} = E_{-\boldsymbol{k}}$ symmetry promotes a DM interaction. The latter indicates that the formation of stabilized skyrmions is expected in this system.

On the contrary, according to Fig. 6.5(c) we find that the energy bands in $\Gamma \to \mathrm{M}$ and $\Gamma \to -\mathrm{M}$ directions are equal. These symmetric energy bands are also shown in the density of states (DOS) diagram of the corresponding directions (Fig. 6.5(d)). This symmetry that appears in ΓM direction can be explained by the symmetries of the crystal structure of the system, and in particular the reflection symmetry over the $x = 0$ plane, as has been discussed above.

Fermi surface states

After the formation of stabilized skyrmions in this system, we aim to investigate spin transport properties solving the Boltzmann equation. Because of this, we are interested in the Fermi surface states.

In Fig. 6.6 the projection of the Fermi surface in the Fe layer, in which the skyrmion is formed, is presented, for the states projected to spin down and spin up. Here, the breaking of the conjugation symmetry is also noticed, as we distinguish in Figs. 6.6(left and right) that the density of states in k_x differs from the corresponding density on $-k_x$ states. On the other hand, we observe the $k_y \to -k_y$ reflection symmetry.

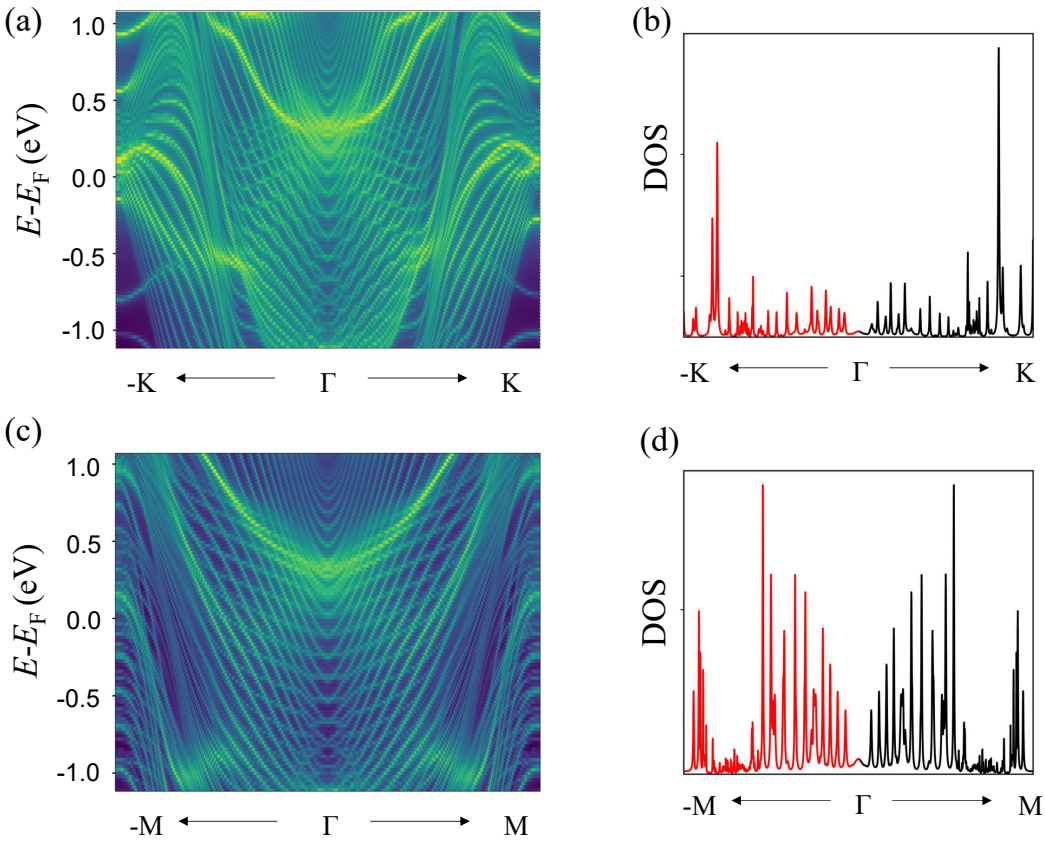

Figure 6.5: (a), (c) The band structure of Pd/Fe/Ir film, for the states which are projected to spin down in $\Gamma \to \mathrm{K}$ and $\Gamma \to -\mathrm{K}$ directions, as well as in $\Gamma \to \mathrm{M}$ and $\Gamma \to -\mathrm{M}$ directions, respectively. The line density defines the projection of the density in Fe layer. (b), (d) The density of states (DOS) of Fe layer in the corresponding directions. The Fermi level is $E_\mathrm{F} = 12.5$ eV.

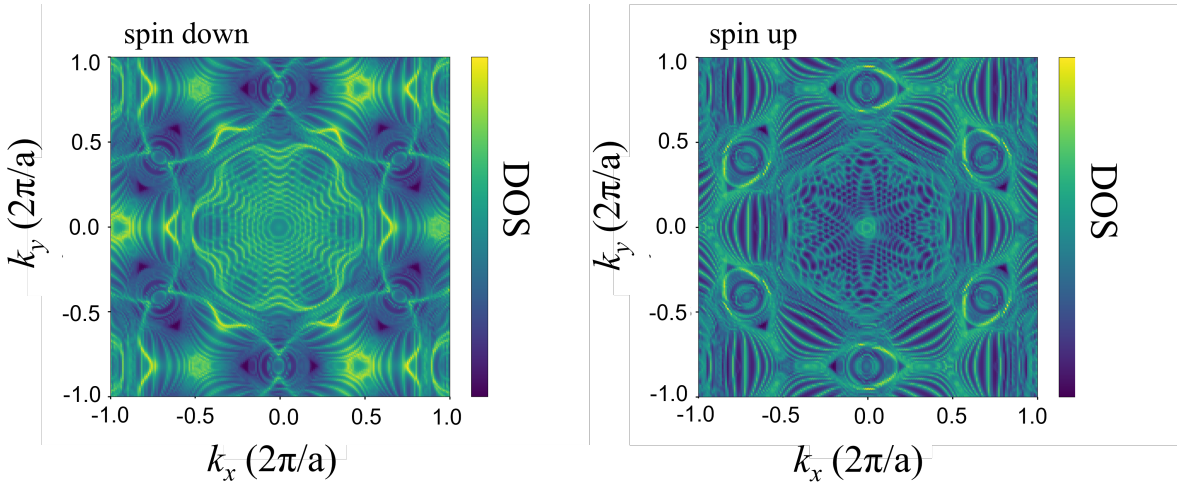

Figure 6.6: The projection of the Fermi surface states in Fe layer, for the states which are projected to spin down (left) and spin up (right).

Computational details

The host crystal structure is simulated by a thin film of 42 layers in total, 34 Ir, 1 Fe and 1 Pd, including 3 vacuum layers on top and bottom, considering a fcc-stacking [1]. The thickness of the film is chosen to ensure the complete decoupling from top to bottom surface states [57]. The parameters of the relaxed interlayer distances in the film that are used, are presented in Table 6.2, as have been found by Dupé et al. [123]. The lattice constant which is used, is equal to a = 3.793 Å, and is found according to the relation $d_{\mathrm{Ir-Ir}} = \mathrm{a}\sqrt{3}/3$, where $d_{\mathrm{Ir-Ir}}$ is the distance between consecutive atomic planes. Thus, the direct lattice vectors are given as

$$\boldsymbol{u}_1 = (0.707107, 0)\mathrm{a} \tag{6.6}$$
$$\boldsymbol{u}_2 = (0.353553, 0.612372)\mathrm{a} \tag{6.7}$$
$$\tag{6.8}$$

and the reciprocal lattice cell vectors are found as

$$\boldsymbol{b}_1 = (1.414214, -0.816497)\mathrm{a} \tag{6.9}$$
$$\boldsymbol{b}_2 = (0, 1.632993)\mathrm{a} \tag{6.10}$$

The self-consistent calculations for the electronic structure of the ferromagnetic Pd/Fe/Ir(111) host system, were performed considering the local density approximation (LDA) for the exchange-correlation potential [63]. A finite angular momentum cutoff of $l_{\max} = 2$ is used, for the orbital expansions of the Green function, and a Brillouin zone mesh of 30×30 k-points.

[1] It has been found that the fcc-stacking is energetically favorable compared to hcp-stacking [123].

Pd/Fe/Ir(111)	
$d_{\mathrm{Ir-Ir}}$	2.19Å
$d_{\mathrm{Fe-Ir}}$	2.06Å
$d_{\mathrm{Pd-Fe}}$	2.02Å

Table 6.2: The relaxed interlayer distances in the Pd/Fe/Ir(111) thin film, according to Dupé et al. [123].

For the calculations of the bandstructure (Figs. 6.5(a), 6.5(c)), a k-mesh of 100×100 k-points was used in each direction. The high symmetry points Γ, K and M are defined as $\Gamma = (0,0)$, $\mathrm{K} = \left(\frac{\sqrt{3}|\boldsymbol{b}_1|}{6}, \frac{|\boldsymbol{b}_2|}{2}\right)$, and $\Gamma\vec{\mathrm{M}} = \frac{\boldsymbol{b}_1}{2}$. The density of states diagrams (Figs. 6.5(b), 6.5(d)) were obtained by considering a k-mesh of 1000 points in each symmetry direction. The Fermi surface calculations, as presented in Fig. 6.6 were carried out within a mesh of 200×200 k-points. The aforementioned first-principles calculations were performed with the Jülich KKRhost code [100].

6.4 Formation of stabilized skyrmions

The state-of-the-art way to predict skyrmion formation from microscopic theory is to calculate the parameters of a spin Hamiltonian from first principles, i.e., from quantum mechanical calculations of the electronic structure of the material, based on density-functional theory (DFT) without adjustable parameters. The interaction parameters are calculated by considering a number of different magnetic states and fitting the energy differences to a model Hamiltonian [110, 124]. However, beyond the state of the art, large-scale simulations [57, 58] have made possible the prediction of skyrmion stability in fully ab-initio calculations, for skyrmions of a few nanometers in diameter, without resorting to a model Hamiltonian. Such simulations are achievable only by using Green function methods (in particular, the Korringa-Kohn-Rostoker (KKR) Green function method), so that the self-consistent calculation is confined only in the skyrmion region of a few hundreds of atoms, instead of thousands of atoms that would be minimally required by wave-function methods.

Calculation of stable skyrmions within KKR Green function method

Here, we apply the KKR Green function method to form three different sizes skyrmions in Pd/Fe/Ir from first-principles calculations. Within this approach, we consider the skyrmion as a defect cluster embedded into the ferromagnetic host system Pd/Fe/Ir(111). Then, the following Dyson equation is solved self-consistently, including the non-collinear magnetism

$$G^{\mathrm{def}} = G^{\mathrm{host}} + G^{\mathrm{host}} \Delta V G^{\mathrm{def}}, \tag{6.11}$$

which relates the Green function of the ferromagnetic host system G^{host} to the Green function of the perturbed non-collinear system G^{def} through a perturbing potential V.

The Green function is a matrix in spin space, as defined in Eq. (2.15). Thus, the Green function of the non-collinear state at site i, G_{ii}^{NC}, can be found via the Dyson equation [69, 125]

$$G_{ii}^{\mathrm{NC}} = G_{ii}^{\mathrm{FM}} + \sum_{j} G_{ij}^{\mathrm{FM}} \Delta V_j G_{ji}^{\mathrm{NC}}, \tag{6.12}$$

where G_{ii}^{FM} is the Green function of the corresponding ferromagnetic state i, in which the spin moments are oriented along the z direction. The perturbed potential ΔV determines the change of the potential due to the rotation of the magnetic moments, therefore depends on the difference between the skyrmion magnetization and the magnetization in the ferromagnetic state. In a simple approximation, it is expressed just by a rotation as

$$\Delta V_i = B_i(\boldsymbol{\sigma} \cdot \hat{\boldsymbol{e}}_{\boldsymbol{M}_i} - \boldsymbol{\sigma} \cdot \hat{\boldsymbol{e}}_z), \tag{6.13}$$

where B_i, which acts as a magnetic field, is the difference of the spin up and spin down components of the potential in the ferromagnetic state, i.e., $B_i = (V_i^{\uparrow} - V_i^{\downarrow})$, $\boldsymbol{\sigma}$ is the Pauli vector, and $\hat{\boldsymbol{e}}_z$ the unit vector in z direction. In practice, beyond the simple approximation, the atom-dependent change of the magnetic moment angle induces a change of the potential as a function of position, $V_i^{\uparrow}(\boldsymbol{r}) - V_i^{\downarrow}(\boldsymbol{r})$, as well as the non-magnetic part of the potential, $(V_i^{\uparrow}(\boldsymbol{r}) + V_i^{\downarrow}(\boldsymbol{r}))/2$, which is also accounted for in the self-consistent calculations. The magnetization $\boldsymbol{M}$ rotation direction in the skyrmion region is defined by the unit vector $\hat{\boldsymbol{e}}_{\boldsymbol{M}_i}$

$$\hat{\boldsymbol{e}}_{\boldsymbol{M}_i} = (\sin\theta(r)\cos\phi(r), \sin\theta(r)\sin\phi(r), \cos\theta(r)). \tag{6.14}$$

The skyrmion defect cluster consists of a disk of Fe atoms, including the first neighbors of the Ir-layer below and the Pd-layer above. The size of the skyrmion is defined by the number of atoms in the disk, which is biased by a boundary condition in the rim of this disk, setting the atoms outside in the ferromagnetic state. The central atom is also spin flipped ($\theta = 180°$) as a boundary condition. The skyrmions formation is established by the relaxation of the magnetization of the atoms in the defect cluster, in size and direction, as well as the convergence of their potentials. We carry out DFT calculations increasing the impurity atoms in the skyrmion disk until the relaxation of the magnetization in the rim of this disk in the skyrmionic state (the ferromagnetic state) is achieved.

More specifically, we consider three different sizes of skyrmion profiles. The smaller skyrmion is formed within a disk consisting of 25 atoms in the defect cluster (1st, 2nd, and 3rd Fe neighbors of the central Fe atom, i.e., 19 Fe atoms, including the first neighbors of Ir and Pd atoms). For the formation of the second skyrmion we consider a disk of 121 atoms in the defect cluster (1st, ..., 5th Fe neighbors of the central Fe atom, i.e., 37 Fe atoms, including the neighboring atoms of the Ir substrate and Pd capping in the region of the skyrmion). The third, largest skyrmion consists of 349 atoms in the defect cluster (1st, ..., 14th Fe neighbors of the central Fe atom, i.e., 121 Fe atoms, including the nearest Ir and Pd atoms), that are allowed to relax their spin direction.

In Fig. 6.7, the spin structure of the three different skyrmions sizes, which are obtained by our ab-initio calculations, are shown. We observe that the non-collinearity is more

intense near the skyrmion core (the center of the skyrmion), independently of the skyrmion size. We find that the direction of the magnetization and its deviation of the ferromagnetic state is strongly dependent on the skyrmion size. In Fig. 6.7(c), we observe that the magnetization in the rim has been relaxed in angle $\theta = 1.8°$, i.e. very close to the ferromagnetic state. As a consequence, the relaxation of the magnetization in the skyrmionic state with respect to skyrmionic size has been achieved in this largest skyrmion.

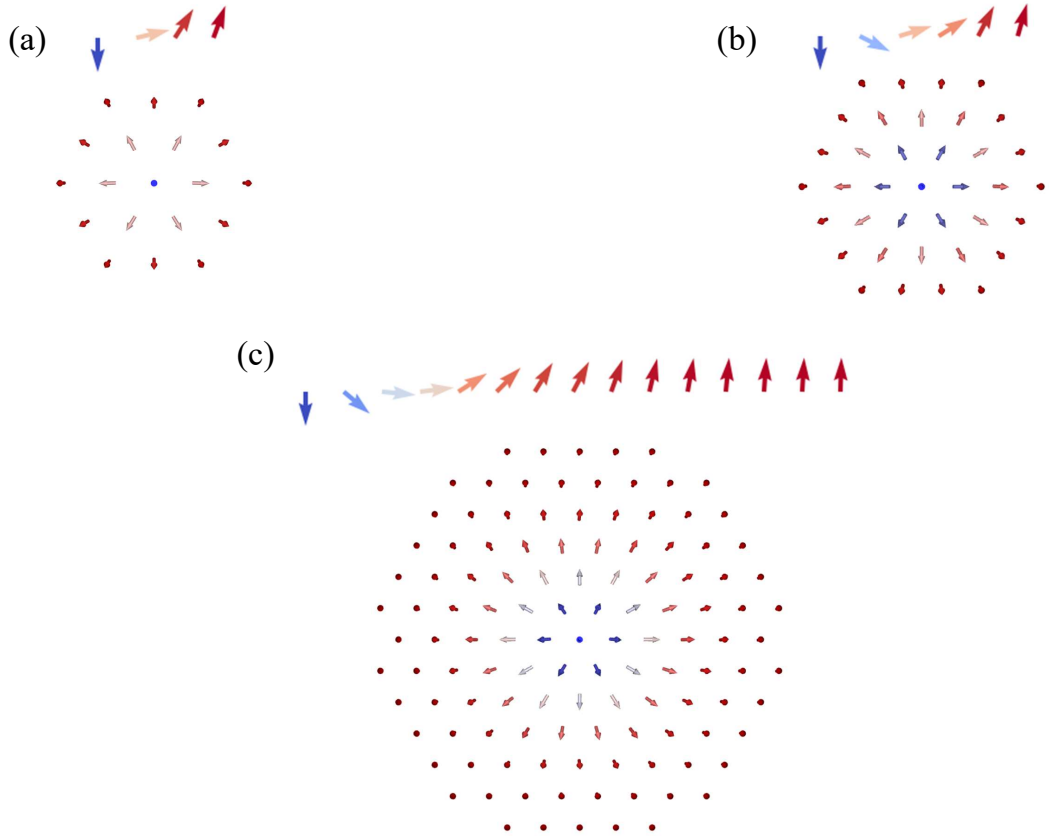

Figure 6.7: Down: The magnetization after the relaxation of Fe spins in the corresponding positions in the crystal surface, for the formation of different sizes of magnetic skyrmions in Pd/Fe/Ir(111) film, consisting of (a) 19 Fe atoms, (b) 37 Fe atoms and (c) 121 Fe atoms. Up: The angle θ is depicted for the central Fe atom, and for the 1st, 2nd, etc., neighbors. The color code represents the magnitude of the magnetization in z direction.

The size of the skyrmion is of pivotal importance for its experimental observation, as well as for potential applications. The skyrmion profile is determined by the skyrmion radius r_{sk}, which is defined as the distance in the crystal surface at which the z component of the magnetization $\boldsymbol{M}$ changes sign, i.e., $M_z(r_{\mathrm{sk}}) = 0$, or respectively $\theta(r_{\mathrm{sk}}) = 90°$ [126, 127]. In Fig. 6.8 the magnetization profile $\theta(r)$ is depicted for the studied skyrmions. Therefore, we can determine the skyrmion radius by the intersection of the skyrmion profile with the horizontal dashed line at $\theta = \pi/2$. Having estimated the radius of the three different skyrmion sizes, we present the diameter d_{sk} of the three different skyrmion profiles in Table 6.3. Comparing our results with corresponding experimental study [47], we calculate smaller skyrmions formed in Pd/Fe/Ir. It is known that in the local spin density approximation, Pd shows an overestimated spin susceptibility compared to experiment. In the present system, this means that the Pd capping shows an overestimated strengthening of the exchange interaction between Fe atoms, i.e., an increased spin stiffness and therefore a reduced skyrmion radius, according to [128].

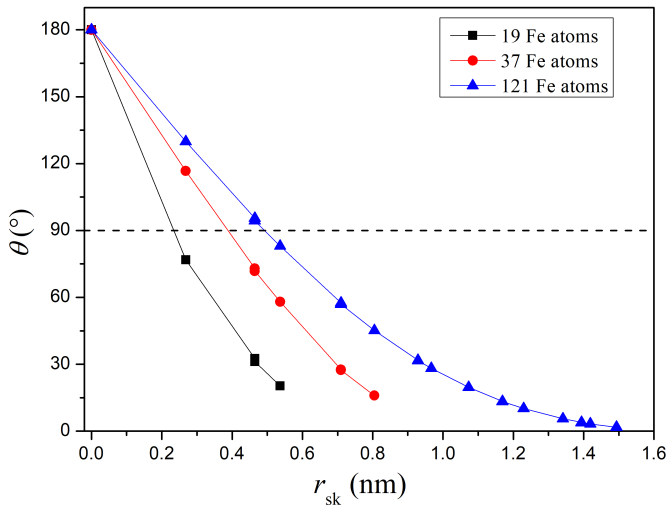

Figure 6.8: Illustration of the magnetization profile of skyrmions $\theta(r)$. The angle θ as a function of the distance r from the center of the skyrmion at $r = 0$ is represented with black rectangular, red circles and blue triangles for the skyrmions containing 19 Fe, 37 Fe and 121 Fe atoms, respectively. The symbols refer to the distance of the corresponding atomic centers from the skyrmion center. The intersection of the skyrmion profile with the horizontal dashed line at $\theta = 90°$ determines the skyrmion radius r_{sk}.

skyrmion of	d_{sk}
19 Fe atoms	0.47 nm
37 Fe atoms	0.77 nm
121 Fe atoms	0.99 nm

Table 6.3: The skyrmion diameter d_{sk} of the three different skyrmion sizes, as it is determined by the magnetization profile of skyrmions (Fig. 6.8).

We also observe that the skyrmions which are formed in the studied system are Néel-type skyrmions, as its spin texture is cycloidal (Fig. 6.7), as predicted for magnetic thin films [129]. The progression of the magnetization of these Néel-type skyrmions is counterclockwise. Consequently, the stabilized magnetic skyrmions which are finally formed in Pd/Fe/Ir(111) film, based on our ab-initio calculations, are in agreement with nano-skyrmions which have been detected with scanning tunneling microscopic experiments [46], as well as with corresponding computational study [57].

Computational details

The formation of stable skyrmions, after the convergence of the Pd/Fe/Ir(111) film, based on spin density functional theory calculations, was performed in two steps. At first, a real space defect cluster is created and the Green function of the film was obtained with the Jülich KKRhost code. In a second step, the impurity-embedding technique was used, within the Jülich KKRimp code [100]. Setting as initial condition the spin-flipping of Fe central atom in the defect cluster, i.e., $(\theta,\, \phi) = (\pi, 0)$, the magnetic moments of atoms within the defect cluster were allowed to relax its size and direction, and the self-consistent potential of the impurity atoms was computed.

7 Topological Hall effect from magnetic skyrmions

7.1 Introduction

The ab-initio calculation of spin-transport phenomena in collinear magnetic systems has been established in a number of works, e.g., [14, 16, 130]. These are based either on the Kubo/Berry-phase formulation, the coherent potential approximation for alloys, or on the Boltzmann equation. The ab-initio approach is superior to model-based calculations, since it accounts for the full electronic structure of the material, but is computationally much heavier. Because of this, there are no reports of ab-initio simulations on spin transport phenomena on skyrmions, since skyrmions entail a higher degree of complexity, as they are non-collinear magnetic structures (i.e., the magnetization direction is position-dependent in the system) without symmetry of periodic displacement (they are localized in space).

Motivated by the potential application of skyrmions detection on spintronic devices [41], the study of the topological Hall effect is pivotal. In this chapter the results of ab-initio computational study of the Topological Hall effect in magnetic skyrmion systems are included. Our focus is on the scattering properties of electrons spins off skyrmions formed in Pd/Fe/Ir film, and in particular on the topological Hall effect, which is a means of experimental detection of skyrmions in thin-film heterostructures [54, 131–135].

This Chapter is structured as follows. In Sec. 7.2 we give a short introduction to

the Ordinary and Anomalous Hall effect, and we describe the Topological Hall effect. The results of the spin-transport calculations are presented in Sec. 7.3. The dependence of the longitudinal resistivity and the topological Hall effect on an additional electron scattering, which represents the disorder of the sample, is discussed.

7.2 Hall effects

Ordinary and Anomalous Hall effect

The ordinary Hall effect was proposed by E.H. Hall in 1879 [136], who discovered that a transverse force is exerted on the electrons, when an electric current j_y flows through a conductive material in the presence of an external perpendicular magnetic field H_z, deflecting the current toward one side of the conductor and producing a transverse voltage.

A few years later Hall discovered a much stronger Hall effect in ferromagnetic materials, the Anomalous Hall Effect (AHE) [56, 137, 138]. The description of this anomalous contribution to Hall effect was proposed by Smith and Sears, by the following experimentally established relation for the (off-diagonal) Hall resistivity in ferromagnets

$$\rho_{xy}^{\mathrm{H}} = \rho^{\mathrm{OHE}} + \rho^{\mathrm{AHE}} = R_0 H + 4\pi R_s M. \tag{7.1}$$

The first term, which is proportional to an external magnetic field H, corresponds to the ordinary Hall resistivity ρ^{OHE}. The second term, with ρ^{AHE} the anomalous Hall resistivity, describes the anomalous Hall effect, that depends on the presence of the magnetization M, and can be observed even in the absence of an external magnetic field. The spin-orbit interaction is a prerequisite for the existence of the anomalous Hall effect [139], which as a result can be observed only in materials with broken conjugation symmetry, $HK \neq KH$ (see Sec. 6.3). In most of materials, the anomalous (spontaneous) Hall coefficient R_s is one of magnitude greater than the ordinary Hall coefficient R_0.

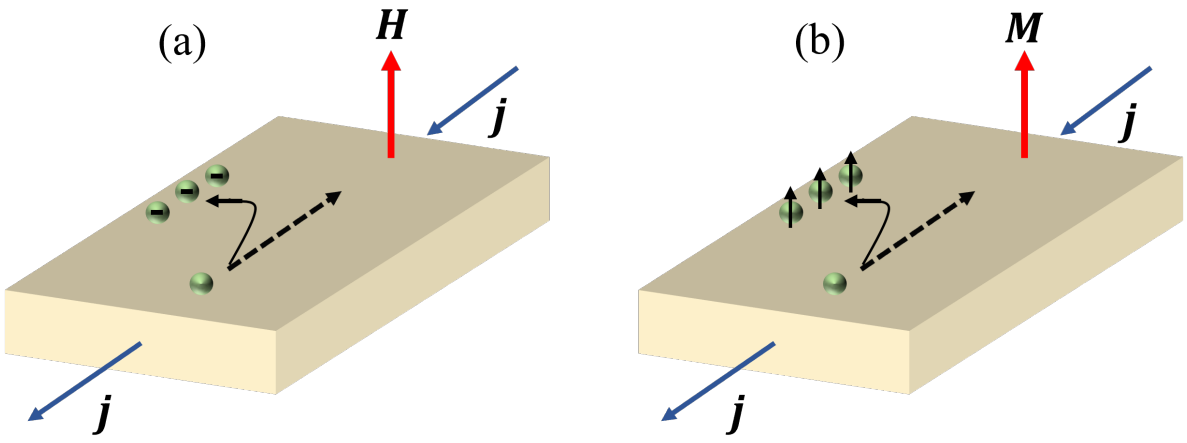

Figure 7.1: Schematic representation of the (a) Ordinary and (b) Anomalous Hall effect.

Topological Hall effect

The Hall effect in ferromagnetic materials with a nontrivial (chiral) spin texture is called Topological Hall Effect (THE). This phenomenon is caused by the scalar spin chirality $\boldsymbol{S}_i \cdot (\boldsymbol{S}_j \times \boldsymbol{S}_k)$ which becomes nonzero when the spin configuration is noncoplanar. This mechanism is described by the Berry phase concept: a fictitious magnetic flux proportional to the spin chirality is created, as the noncoplanar magnetization texture is related to the Berry curvature [140–142]. As a result, the spin-orbit coupling is not vital for the existence of this mechanism on the contrary to the AHE. Then, the total Hall resistivity in ferromagnets is given as the sum of the individual contributions of OHE, AHE and THE:

$$\rho_{xy} = \rho^{\mathrm{OHE}} + \rho^{\mathrm{AHE}} + \rho^{\mathrm{THE}}. \tag{7.2}$$

The topological Hall effect [51, 55] is observed when a lateral current is formed by an applied electric field in a layered magnetic system with a skyrmion, caused by the deflection of the moving electrons off the skyrmion's non-collinear magnetic texture.

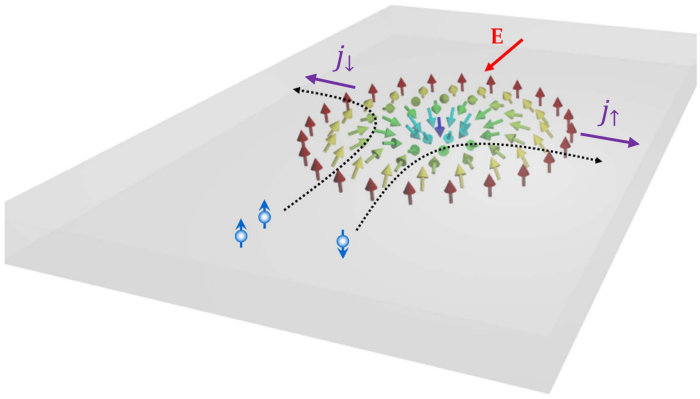

Figure 7.2: Schematic representation of the Topological Hall effect in a ferromagnetic thin film when an external electric field is applied, caused by the non-collinear spin configuration of a Néel-type skyrmion in a ferromagnetic thin film when an external electric field is applied. Fig. by Zhang et al. [143].

7.3 Hall effect caused by magnetic skyrmions

Having already established the formation of stable magnetic skyrmions in Pd/Fe/Ir film, as described in Chapter 6, we now focus on the study of spin-transport properties in the presence of these skyrmions, based on first-principles calculations.

At first, non-collinear spin density functional theory calculations, employing the KKR Green function method were performed for the solution of the scattering problem of the surface electrons off skyrmions in Pd/Fe/Ir(111) film. Thus, we calculate the scattering amplitude on the Fermi surface states. Next, combining the KKR method with the

Boltzmann formalism, the semi-classical Boltzmann transport equation is solved based on quantities given by ab-initio calculations. In this way, we compute the conductivity tensor $\boldsymbol{\sigma}$ (Sec. 3.2). Therefore, the knowledge of the conductivity allows us to estimate the resistivity, and the topological Hall angle, which are given by the conductivity tensor.

In order to examine the effect of the skyrmion size on spin-transport phenomena, we perform the spin-transport calculations for two differently sized magnetic skyrmions, which are formed in Pd/Fe/Ir film, as they are described in Chapter 6. The smaller skyrmion which is investigated, is of the order of 37 Fe atoms in the defect cluster and its diameter is found equal to 0.77 nm. The larger skyrmion consists of 121 Fe atoms in the defect cluster, and its diameter is calculated 0.99 nm (Table 6.3).

At first, we study the scattering properties of the two different sizes of magnetic skyrmions. In Fig. 7.3 the scattering rate off the skyrmions is presented for the states at $E = E_{\mathrm{F}}$, integrated over the Fermi surface. The scattering rate is observed to be higher in the larger skyrmion system.

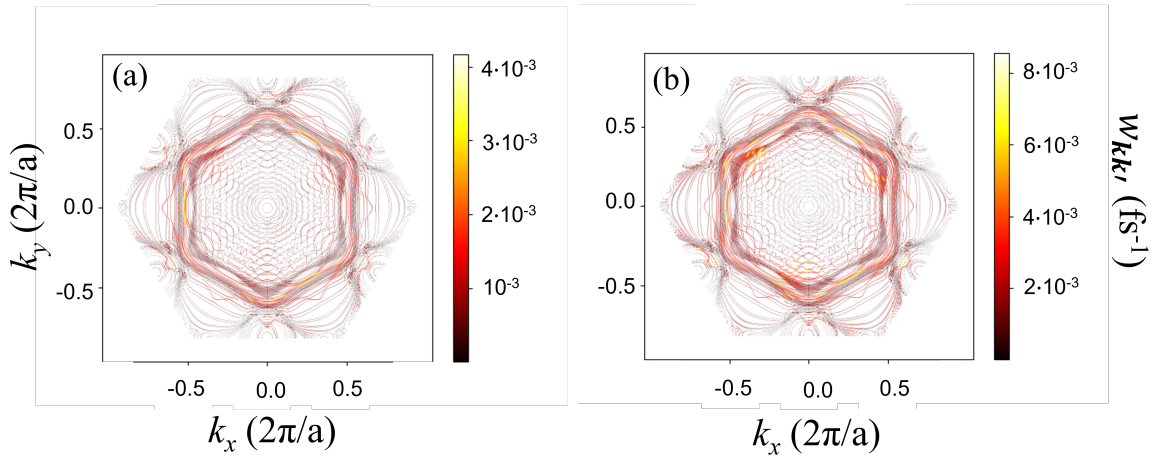

Figure 7.3: The integrated scattering rate $\tau_{\boldsymbol{k}}^{-1} = \Omega_{\mathrm{BZ}}^{-1} \int_{\mathrm{FS}} v_{\boldsymbol{k}'}^{-1} w_{\boldsymbol{k}\boldsymbol{k}'} dk'$ off the skyrmion of diameter (a) $d = 0.77$ nm and (b) $d = 0.99$ nm on the Fermi surface.

Disorder induced band broadening

An additional electron scattering, due to the existence of other sources of scattering (such as disorder by other defect types), is expected to affect experimental measurements.

In order to make our simulations more realistic, this scattering contribution is added in our study, in analogy to a band broadening by the disorder. More specifically, an additional constant energy term to the calculation of the relaxation time and the scattering rate is inserted. The relaxation time $\tau_{\boldsymbol{k}}$ (Eq. (3.21)) is reformulated to $\tilde{\tau}_{\boldsymbol{k}}$ according to the following relation

$$\frac{1}{\tilde{\tau}_{\boldsymbol{k}}} = \frac{1}{\tau_{\boldsymbol{k}}} + \frac{2\Gamma}{\hbar}, \tag{7.3}$$

where the parameter Γ is a constant band broadening, which has energy dimensions of the order of meV. This constant parameter indicates the disorder strength.

The matrix elements of the scattering rate $w_{\boldsymbol{k'k}}$ must be also reformed in a consistent way, in order to ensure that $\tilde{\tau}_{\boldsymbol{k}} = 1/\sum_{k'} \tilde{w}_{\boldsymbol{k'k}}$. Then, the scattering rate $\tilde{w}_{\boldsymbol{k'k}}$ is calculated by the equation

$$\tilde{w}_{\boldsymbol{k'k}} = w_{\boldsymbol{k'k}} + \frac{2\Gamma}{\hbar n(E(\boldsymbol{k'}))}\delta(E(\boldsymbol{k}) - E(\boldsymbol{k'})), \tag{7.4}$$

where $n(E)$ defines the density of states.

Therefore, the Boltzmann equation (Eq. (7.5)) is solved including the constant energy term by the relaxation time $\tilde{\tau}_{\boldsymbol{k}}$ and the scattering rate $\tilde{w}_{\boldsymbol{k'k}}$, which are calculated according to Eqs. (7.3),(7.4), as follows

$$\boldsymbol{\Lambda_k} \cdot \hat{n}_{\boldsymbol{\mathcal{E}}} = \tilde{\tau}_{\boldsymbol{k}} \left[\boldsymbol{v_k} \cdot \hat{n}_{\boldsymbol{\mathcal{E}}} + \sum_{\boldsymbol{k'}} \tilde{w}_{\boldsymbol{k'k}} (\boldsymbol{\Lambda_{k'}} \cdot \hat{n}_{\boldsymbol{\mathcal{E}}}) \right]. \tag{7.5}$$

Longitudinal resistivity

By the solution of the Boltzmann equation, we compute the conductivity tensor $\boldsymbol{\sigma}$, as described in Section 3.2. From this follows the resistivity tensor $\boldsymbol{\rho}$,

$$\boldsymbol{\rho} = \boldsymbol{\sigma}^{-1}. \tag{7.6}$$

In the following, we investigate the computed longitudinal resistivity ρ_{xx} for the different skyrmion sizes which is almost identical to ρ_{yy}, as we have found in the calculations.

Moreover, we derive results for five different skyrmion concentrations (0.1%, 2%, 4%, 6%, and 10%) in this system. Hence, we can find how the skyrmion concentration in the film surface affects the spin-transport properties. In addition, considering different skyrmion concentrations in the system, we can examine our calculations for numerical noise. Nevertheless, the only realistic skyrmion concentration in the surface among the different computed concentrations, is the lowest, i.e., 0.1% concentration of skyrmion in the system surface [1]. A system with 0.1% concentration of skyrmion in Pd/Fe/Ir film is experimentally feasible. Otherwise, in the case of a defect (skyrmion) concentration higher than 1%, the surface will be practically fully covered by skyrmions, at least in the case of the skyrmions that are converged in diameter (0.99 nm, including 121 Fe atoms). The higher concentrations should be considered numerical experiments for a consistency check of our results.

In Figs. 7.4(a-b) the effect of the disorder strength Γ (Eq. (7.3)), induced by the band broadening, on the longitudinal resistivity ρ_{xx}, is shown for the two different skyrmion sizes. The scattering calculations were performed considering only the Fe atoms in the skyrmion defect cluster (excluding from the scattering calculations the contribution of Ir and Pd atoms in the skyrmion region). We find that the longitudinal resistivity has a linear dependence on the band broadening in the realistic case of 0.1% skyrmion concentration

[1] 1% skyrmion concentration in the system surface corresponds to one single skyrmion in 100 atoms in the surface.

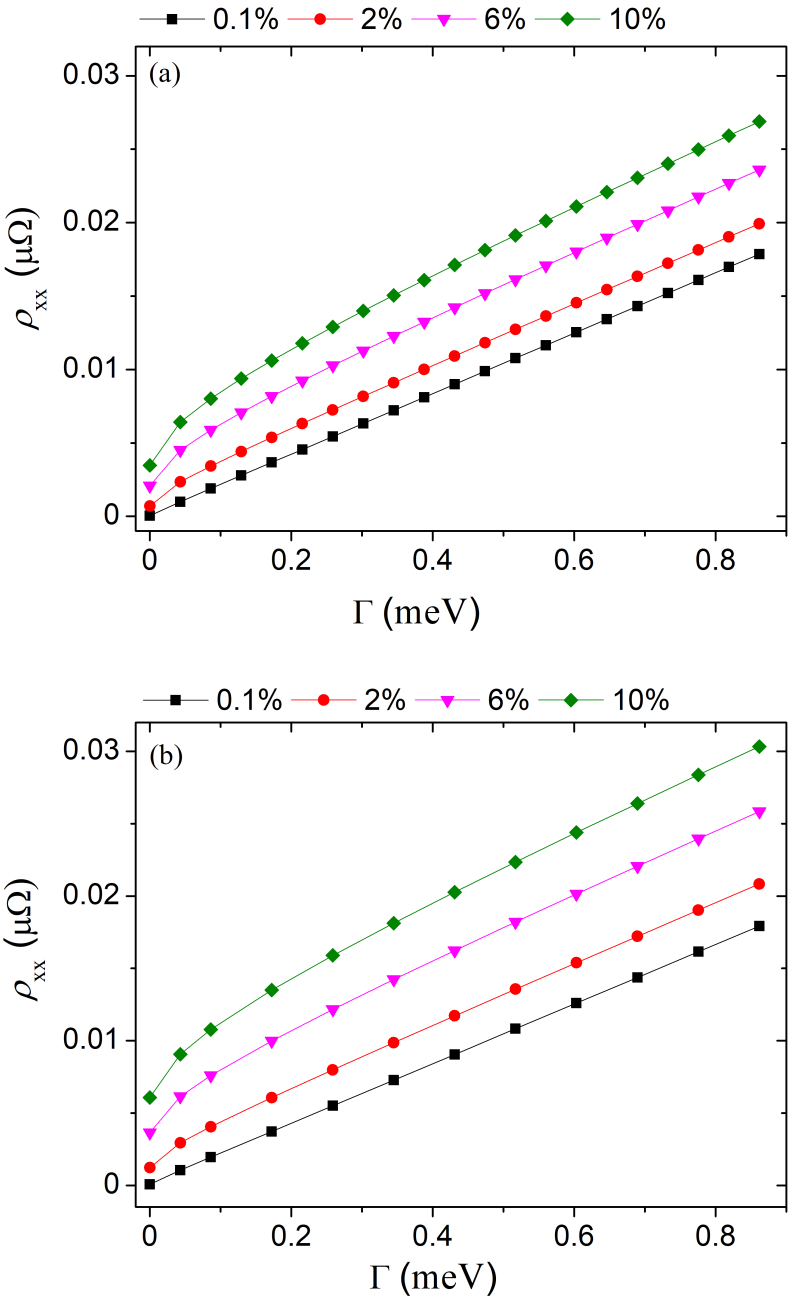

Figure 7.4: The longitudinal resistivity ρ_{xx} as a function of the disorder broadening Γ (Eq. (7.3)) for the skyrmion with diameter (a) 0.77 nm (consists of 37 Fe spins) and (b) 0.99 nm (consists of 121 Fe spins), in Pd/Fe/Ir(111) film. The black rectangular, red circles, pink down-triangles and green rhombus, correspond to the five different skyrmion concentrations, 0.1%, 2%, 6% and 10% in Pd/Fe/Ir(111) film, respectively.

in the system surface, whereas an almost linear correlation between the resistivity and the constant energy parameter Γ, is observed in higher skyrmion concentrations. In addition, comparing the two differently sized skyrmions, we find that the longitudinal resistivity is independent of the skyrmion size, at least in the realistic system.

Hall angle

For the application of an external electric field $\mathcal{E}_y$ along the y-direction, and the propagation of a perpendicular charge current along the x-direction, the anomalous Hall conductivity (or the Hall conductivity in general) can be defined as the non-diagonal xy-component of the charge conductivity tensor σ^{c}_{xy}. Then, the anomalous Hall angle is defined as

$$\alpha^{\mathrm{c}} = \frac{\sigma^{\mathrm{c}}_{xy}}{\sigma^{\mathrm{c}}_{yy}}. \tag{7.7}$$

In analogy, we define the Hall angle due to topological Hall effect, arising from the non-collinear spin texture of the magnetic skyrmions in Pd/Fe/Ir(111) film.

For practical applications, the behavior of the topological Hall angle (THA) (Eq. (7.7)) in the presence of the disorder in the sample is of great importance. In Figs. 7.5(a-b) the topological Hall angle is depicted as a function of the disorder strength Γ for the two differently sized skyrmion systems and for the different skyrmion concentrations in the surface. Thus, we can analyze the influence of the skyrmion size on the THE measurements. Comparing the extracted results of THA of the larger skyrmion system (Fig. 7.5(b)) with the corresponding results of the smaller skyrmion system (Fig. 7.5(a)), we can see that the Hall angle is one order of magnitude higher in the case of the larger skyrmion. Since the longitudinal resistivity, i.e., the diagonal term of the conductivity tensor, is quite similar for the different skyrmion sizes, we conclude that the larger Hall angle which is calculated in the larger skyrmion system, arises from the non-diagonal conductivity term. The latter indicates that the studied skyrmion system should be converged with respect to its radius, without setting boundary conditions which limit the skyrmion size, since the Hall effect is affected significantly. However, it should be mentioned that in the experimentally feasible system of 0.1% skyrmion concentration, the Hall angle becomes rather small as the disorder strength increases.

We follow up our analysis with the investigation of the topological Hall effect caused by the larger formed stable magnetic skyrmion (of diameter 0.99 nm) in the Pd/Fe/Ir film. We consider the 0.1% skyrmion concentration in the system surface, and we examine the influence on the THA in the cases of either taking into account, or, alternatively, excluding the Ir and Pd atoms in the skyrmion region in the scattering calculations. In order to achieve this, we compute the resistivity and the Hall angle including in the scattering region the Fe atoms, as well as the nearest Pd and Ir atoms which form the skyrmion defect cluster (black rectangular in Fig. 7.6). Moreover, we calculate results taking into account in our calculations the scattering caused by (i) only the Fe atoms (red circles in Fig. 7.6), (ii) the Fe and the nearest Pd atoms (blue up-triangles in Fig. 7.6), and (iii) the Fe and the nearest Ir atoms (pink down-triangles in Fig. 7.6).

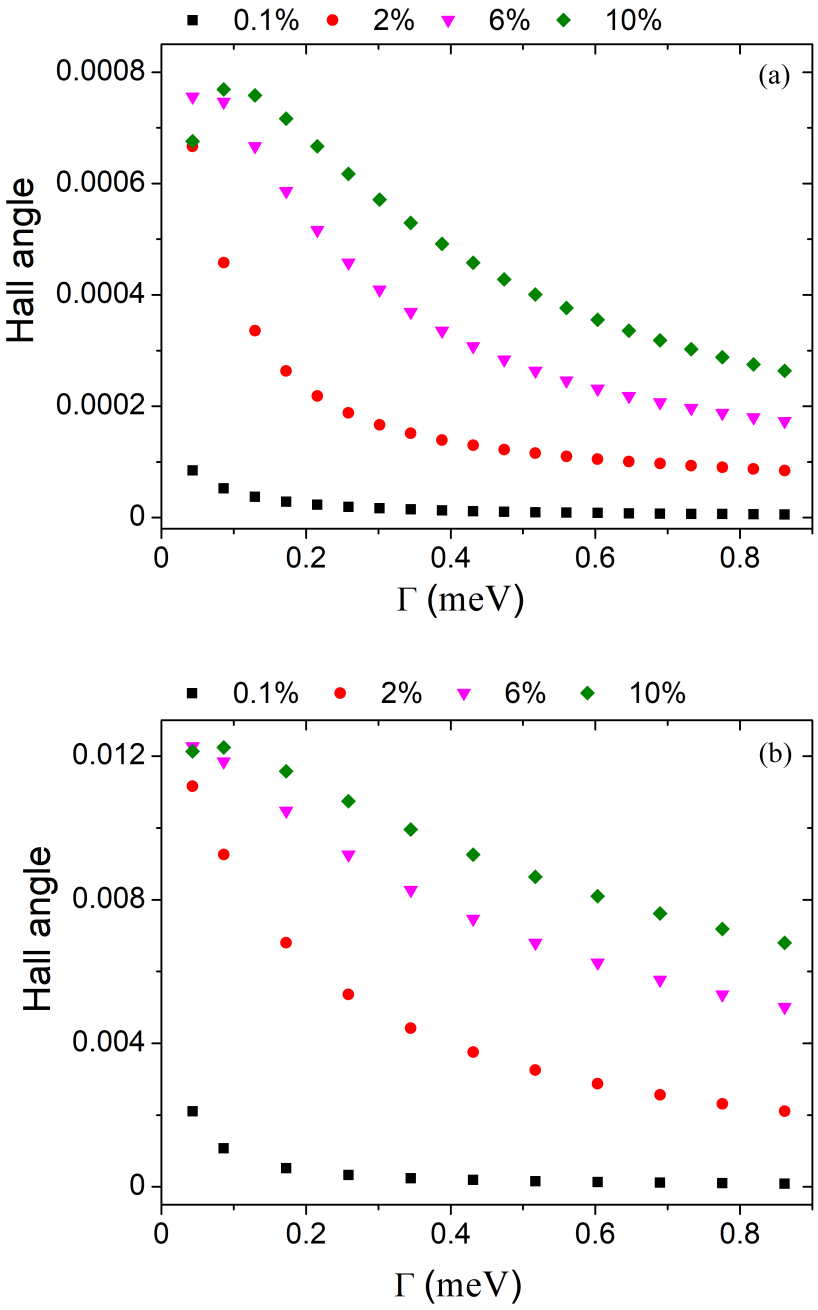

Figure 7.5: The Topological Hall angle as a function of the disorder broadening Γ (Eq. (7.3)), for the skyrmion with diameter (a) 0.77 nm (consists of 37 Fe spins) and (b) 0.99 nm (consists of 121 Fe spins), in Pd/Fe/Ir(111) film. The black rectangular, red circles, pink down-triangles and green rhombus, correspond to the five different skyrmion concentrations, 0.1%, 2%, 6% and 10% in Pd/Fe/Ir(111) film, respectively.

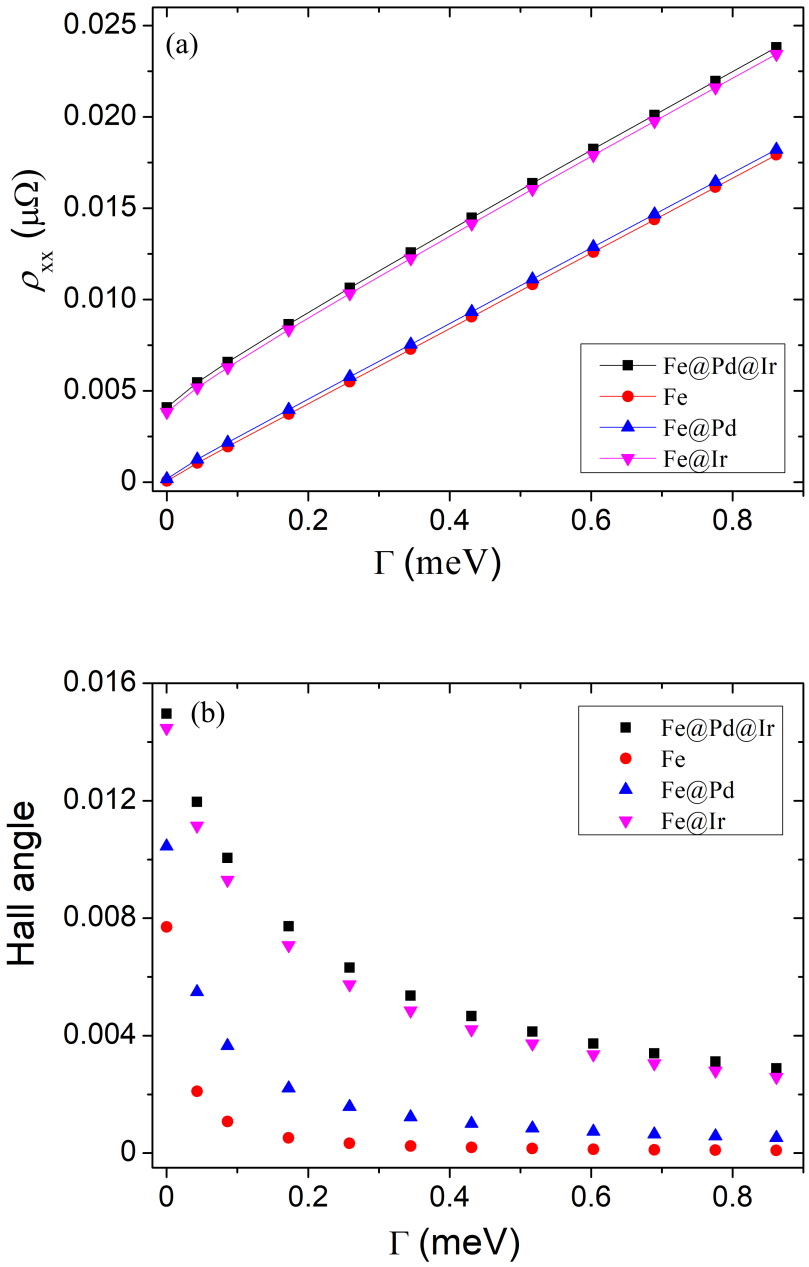

Figure 7.6: (a) The longitudinal resistivity ρ_{xx} and (b) the Topological Hall angle as a function of the disorder broadening Γ (Eq. (7.3)) for the skyrmion of diameter 0.99 nm, considering 0.1% skyrmion concentration in the surface of Pd/Fe/Ir(111). The black rectangular represent the calculations, considering in the scattering process the skyrmion consists of 349 atoms (121 Fe atoms, including Ir and Pd atoms in the skyrmion region), the red circles represent the scattering arising only by the skyrmion defect cluster consists of 121 Fe atoms, the blue up-triangles to the skyrmion defect cluster of 121 Fe atoms including the nearest Pd atoms, and the pink down-triangles to the skyrmion defect cluster of 121 Fe atoms including the nearest Ir atoms.

In Fig. 7.6 it is shown that the computed longitudinal resistivity (Fig. 7.6(a)) and the topological Hall angle (Fig. 7.6(b)) differ if we take into account in the scattering process the whole defect cluster of skyrmion (i.e., Fe, including nearest Pd and Ir atoms) compared to the corresponding results that are found considering only the Fe atoms that form the skyrmion. In contrast, we observe a similar behavior of the results of the whole defect cluster with the corresponding results of the defect cluster which includes Fe and its nearest Ir atoms.

Because of these findings, we calculate the longitudinal resistivity of the large, full-skyrmion system, where the skyrmion defect cluster consists of Fe, as well as its nearest Ir and Pd atoms. As it is shown in Fig. 7.7(a), the calculated resistivity of the systems with higher skyrmion concentrations is one order of magnitude greater compared to the results of the corresponding concentrations in the case that the scattering is calculated for a skyrmion consisting of only Fe spins in the defect cluster (Fig. 7.4(b)).

In Fig. 7.7(b) the THA as a function of the disorder strength is depicted for different skyrmion concentrations in the surface of Pd/Fe/Ir film. A decrease of the THA is seen as the degree of the disorder increases. Therefore, the measured Hall angle in experiments is expected to strongly depend on the degree of disorder of the sample. Comparison of experiment with theory should be possible only if the degree and type of disorder is known in experiment.

Computational details

In a first step, using the JuKKR-PKKprime code [100] we form the Fermi surface of Pd/Fe/Ir film. Next, we apply the DFT within KKR Green function method in order to compute the scattering matrix $T_{\boldsymbol{k}'\boldsymbol{k}}$ elements (Section 2.4) on the Fermi surface states, using the DFT-code JuKKR-KKRhost [100]. Combining the KKR method with the Boltzmann formalism we solve the semi-classical Boltzmann transport equation self-consistently (Section 3.1) with the JuKKR-PKKprime code. These calculations were carried out considering an ultra thin film of Pd/Fe/Ir(111) system. This ultra thin film is modeled by 17 Ir, 1 Fe and 1 Pd atomic layers, including 2 vacuum layers on top and bottom, i.e., 23 atomic layers in total. For the computation of the conductivity tensor we used 41700 k-points in the full Fermi surface of Pd/Fe/Ir.

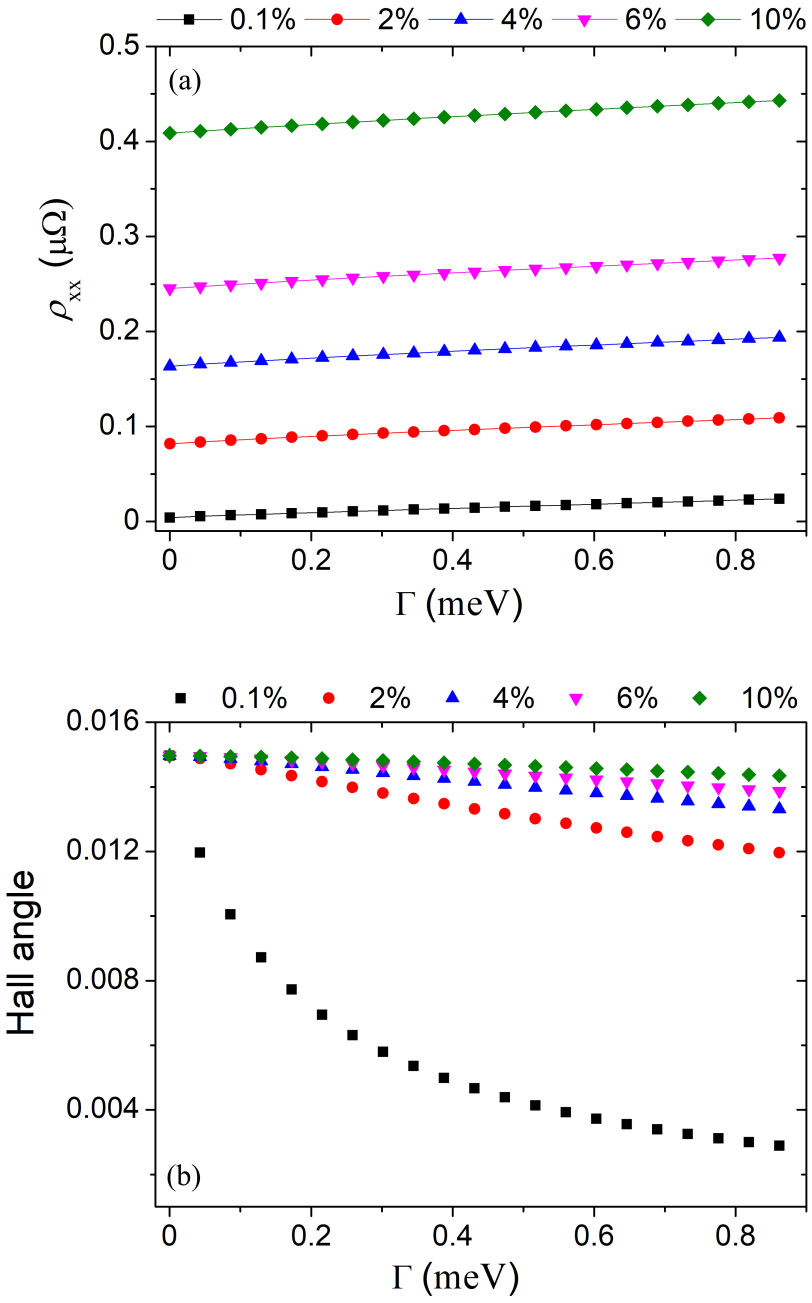

Figure 7.7: (a) The longitudinal resistivity ρ_{xx} and (b) the Topological Hall angle as a function of the disorder broadening Γ (Eq. (7.3)) for the skyrmion of diameter 0.99 nm in Pd/Fe/Ir(111) film. The black rectangular, red circles, blue up-triangles, pink down-triangles and green rhombus, correspond to the five different skyrmion concentrations, 0.1%, 2%, 4%, 6% and 10% in Pd/Fe/Ir(111) system surface, respectively.

8 Conclusions

Motivated by anticipated applications of topological materials in information technology, this Thesis provides an ab-initio microscopic computational study of spin-transport phenomena in topological insulators and magnetic skyrmions, based on electronic scattering theory and density functional theory. For the calculation of the transport properties, the linearized semiclassical Boltzmann equation is employed, with the scattering rate provided by the Korringa-Kohn-Rostoker Green function method. Its solution gives the non-equilibrium distribution function in terms of a mean free path, from which all linear response coefficients to the external electric field follow.

The present Thesis studies phenomena extrinsic in their origin, i.e., arising from defects (either impurity atoms or skyrmions). The applied methods are complementary to the methods for the intrinsic spin torque or the intrinsic anomalous Hall effect in ferromagnets. Both methodologies are necessary for a full picture of transport phenomena in topological materials, contributing to applications in magnetism-based memory.

The first part of the results concerns the surface of the topological insulator Bi_2Te_3 doped with ferromagnetically coupled transition metal impurities (Cr, Mn, Fe, Co) at 2-5% concentration. Among these systems, previous experimental and theoretical work [83] has found a ferromagnetic state and an out-of-plane anisotropy. The quantity of interest here is the spin-orbit torque on the impurity magnetic moments, which is found to be sizeable. We find the Mn-doped system advantageous over the others because it also shows low resistivity and Joule heat production. The effect of sizeable spin-orbit torque

is traced back to a number of reasons. Firstly, all current flows through the surface, as the bulk is insulating. Secondly, the absence of spin degeneracy in the topological surface states means that an electric current is necessarily accompanied by a spin current and a spin accumulation. These two facts are ubiquitous in topological insulators. Thirdly, the spin polarization of the surface states is directed largely in-plane, as is the case in topological insulators with a Dirac cone at the Brillouin zone center. In concurrence with an out-of-plane direction of the impurity magnetic moment, this means that the impurity and conduction spins are mutually perpendicular, resulting in a maximal torque. Thus the sizeable spin-orbit torque depends on characteristics that could be repeated in other similar systems. In particular, the ferromagnetic coupling of impurities relies on the large Fermi wavelength and can be engineered by changing the concentration, while the out-of-plane easy magnetization axis can be engineered by additional n or p doping. Thus our conclusions are relevant from a wider point of view and reinforce the prospects of such systems.

The second part of the results concerns the Hall effect caused by non-collinear, chiral topological magnetic structures, in particular magnetic skyrmions, formed in the Pd/Fe/Ir(111) heterostructure. The choice of the system is based on previous experiments and density-functional calculations, that have shown its existence and stability. Here, non-collinear spin density functional theory calculations within the KKR Green function method were performed, examining the formation of differently sized stable magnetic skyrmions in the Fe ferromagnetic layer. The skyrmion size is varied until a relaxation of the magnetization was reached at a conventional skyrmion radius of 0.5 nm corresponding to a magnetization angle of 2° at the rim (1.5 nm from the center). The skyrmion size is smaller than the experimental result, probably due to an overestimation of the spin stiffness in the local spin density approximation. Next, calculations based on the KKR Green function method and the linearized Boltzmann equation show the emergence of the topological Hall effect. Calculations on differently sized skyrmions demonstrate that the topological Hall angle is significantly affected by the skyrmion size. In addition, taking into account a generic form of disorder in the heterostructure reveals a strong dependence of the topological Hall angle on the degree of the disorder.

Bibliography

[1] I. Žutić, J. Fabian, and S. Das Sarma, "Spintronics: fundamentals and applications", Rev. Mod. Phys. **76**, 323–410 (2004).

[2] S. A. Wolf, D. D. Awschalom, R. A. Buhrman, J. M. Daughton, S. v. Molnár, M. L. Roukes, A. Y. Chtchelkanova, and D. M. Treger, "Spintronics: a spin-based electronics vision for the future", Science **294**, 1488–1495 (2001).

[3] S. Bhatti, R. Sbiaa, A. Hirohata, H. Ohno, S. Fukami, and S. N. Piramanayagam, "Spintronics based random access memory: a review", Materials Today **20**, 530–548 (2017).

[4] C. Chappert, A. Fert, and F. N. Van Dau, "The emergence of spin electronics in data storage", Nature Materials **6**, 813–823 (2007).

[5] J. C. Slonczewski, "Current-driven excitation of magnetic multilayers", Journal of Magnetism and Magnetic Materials **159**, L1–L7 (1996).

[6] L. Berger, "Emission of spin waves by a magnetic multilayer traversed by a current", Phys. Rev. B **54**, 9353–9358 (1996).

[7] D. C. Ralph and M. D. Stiles, "Spin transfer torques", Journal of Magnetism and Magnetic Materials **320**, 1190–1216 (2008).

[8] D. Apalkov, B. Dieny, and J. M. Slaughter, "Magnetoresistive Random Access Memory", Proceedings of the IEEE **104**, 1796–1830 (2016).

[9] A. Manchon, J. Železný, I. M. Miron, T. Jungwirth, J. Sinova, A. Thiaville, K. Garello, and P. Gambardella, "Current-induced spin-orbit torques in ferromagnetic and antiferromagnetic systems", Rev. Mod. Phys. **91**, 035004 (2019).

[10] A. Manchon and S. Zhang, "Theory of nonequilibrium intrinsic spin torque in a single nanomagnet", Phys. Rev. B **78**, 212405 (2008).

[11] P. Gambardella and I. M. Miron, "Current-induced spin–orbit torques", Phil. Trans. R. Soc. A **369**, 3175–3197 (2011).

[12] I. Garate and A. H. MacDonald, "Influence of a transport current on magnetic anisotropy in gyrotropic ferromagnets", Phys. Rev. B **80**, 134403 (2009).

[13] F. Freimuth, S. Blügel, and Y. Mokrousov, "Spin-orbit torques in Co/Pt(111) and Mn/W(001) magnetic bilayers from first principles", Phys. Rev. B **90**, 174423 (2014).

[14] F. Freimuth, S. Blügel, and Y. Mokrousov, "Direct and inverse spin-orbit torques", Phys. Rev. B **92**, 064415 (2015).

[15] G. Géranton, F. Freimuth, S. Blügel, and Y. Mokrousov, "Spin-orbit torques in $L1_0$-FePt/Pt thin films driven by electrical and thermal currents", Phys. Rev. B **91**, 014417 (2015).

[16] G. Géranton, B. Zimmermann, N. H. Long, P. Mavropoulos, S. Blügel, F. Freimuth, and Y. Mokrousov, "Spin-orbit torques and spin accumulation in FePt/Pt and Co/Cu thin films from first principles: the role of impurities", Phys. Rev. B **93**, 224420 (2016).

[17] F. Mahfouzi and N. Kioussis, "First-principles study of the angular dependence of the spin-orbit torque in Pt/Co and Pd/Co bilayers", Phys. Rev. B **97**, 224426 (2018).

[18] I. M. Miron, G. Gaudin, S. Auffret, B. Rodmacq, A. Schuhl, S. Pizzini, J. Vogel, and P. Gambardella, "Current-driven spin torque induced by the Rashba effect in a ferromagnetic metal layer", Nature Materials **9**, 230–234 (2010).

[19] I. M. Miron, K. Garello, G. Gaudin, P.-J. Zermatten, M. V. Costache, S. Auffret, S. Bandiera, B. Rodmacq, A. Schuhl, and P. Gambardella, "Perpendicular switching of a single ferromagnetic layer induced by in-plane current injection", Nature **476**, 189–193 (2011).

[20] K. Garello, I. M. Miron, C. O. Avci, F. Freimuth, Y. Mokrousov, S. Blügel, S. Auffret, O. Boulle, G. Gaudin, and P. Gambardella, "Symmetry and magnitude of spin–orbit torques in ferromagnetic heterostructures", Nature Nanotechnology **8**, 587–593 (2013).

[21] A. Manchon and S. Zhang, "Theory of spin torque due to spin-orbit coupling", Phys. Rev. B **79**, 094422 (2009).

[22] C. L. Kane and E. J. Mele, "Z_2 topological order and the quantum spin Hall effect", Phys. Rev. Lett. **95**, 146802 (2005).

[23] J. E. Moore, "The birth of topological insulators", Nature **464**, 194–198 (2010).

[24] M. Z. Hasan and C. L. Kane, "Colloquium: Topological insulators", Rev. Mod. Phys. **82**, 3045–3067 (2010).

[25] M. Z. Hasan and J. E. Moore, "Three-dimensional topological insulators", Annu. Rev. Condens. Matter Phys. **2**, 55–78 (2011).

[26] D. Pesin and A. H. MacDonald, "Spintronics and pseudospintronics in graphene and topological insulators", Nature Materials **11**, 409–416 (2012).

[27] F. Mahfouzi, N. Nagaosa, and B. K. Nikolić, "Spin-orbit coupling induced spin-transfer torque and current polarization in topological-insulator/ferromagnet vertical heterostructures", Phys. Rev. Lett. **109**, 166602 (2012).

[28] A. R. Mellnik, J. S. Lee, A. Richardella, J. L. Grab, P. J. Mintun, M. H. Fischer, A. Vaezi, A. Manchon, E.-A. Kim, N. Samarth, and D. C. Ralph, "Spin-transfer torque generated by a topological insulator", Nature **511**, 449–451 (2014).

[29] Y. Wang, P. Deorani, K. Banerjee, N. Koirala, M. Brahlek, S. Oh, and H. Yang, "Topological surface states originated spin-orbit torques in Bi_2Te_3", Phys. Rev. Lett. **114**, 257202 (2015).

[30] M. H. Fischer, A. Vaezi, A. Manchon, and E.-A. Kim, "Spin-torque generation in topological insulator based heterostructures", Phys. Rev. B **93**, 125303 (2016).

[31] Y. Fan, X. Kou, P. Upadhyaya, Q. Shao, L. Pan, M. Lang, X. Che, J. Tang, M. Montazeri, K. Murata, L.-T. Chang, M. Akyol, G. Yu, T. Nie, K. L. Wong, J. Liu, Y. Wang, Y. Tserkovnyak, and K. L. Wang, "Electric-field control of spin–orbit torque in a magnetically doped topological insulator", Nature Nanotechnology **11**, 352–359 (2016).

[32] Y. Wang, D. Zhu, Y. Wu, Y. Yang, J. Yu, R. Ramaswamy, R. Mishra, S. Shi, M. Elyasi, K.-L. Teo, Y. Wu, and H. Yang, "Room temperature magnetization switching in topological insulator-ferromagnet heterostructures by spin-orbit torques", Nature Communications **8**, 1364 (2017).

[33] S. Ghosh and A. Manchon, "Spin-orbit torque in a three-dimensional topological insulator–ferromagnet heterostructure: crossover between bulk and surface transport", Phys. Rev. B **97**, 134402 (2018).

[34] H. Wu, P. Zhang, P. Deng, Q. Lan, Q. Pan, S. A. Razavi, X. Che, L. Huang, B. Dai, K. Wong, X. Han, and K. L. Wang, "Room-temperature spin-orbit torque from topological surface states", Phys. Rev. Lett. **123**, 207205 (2019).

[35] S. Shin and H.-W. Lee, "Spin-orbit torque from spin-flipping scattering at ferromagnetic metal/topological insulator interface", Current Applied Physics **19**, 241–245 (2019).

[36] H. Zhang, C.-X. Liu, X.-L. Qi, X. Dai, Z. Fang, and S.-C. Zhang, "Topological insulators in Bi_2Se_3, Bi_2Te_3 and Sb_2Te_3 with a single Dirac cone on the surface", Nature Physics **5**, 438–442 (2009).

[37] D. Hsieh, Y. Xia, D. Qian, L. Wray, F. Meier, J. H. Dil, J. Osterwalder, L. Patthey, A. V. Fedorov, H. Lin, A. Bansil, D. Grauer, Y. S. Hor, R. J. Cava, and M. Z. Hasan, "Observation of Time-Reversal-protected single-Dirac-cone topological-insulator states in Bi_2Te_3 and Sb_2Te_3", Phys. Rev. Lett. **103**, 146401 (2009).

[38] Y. L. Chen, J. G. Analytis, J.-H. Chu, Z. K. Liu, S.-K. Mo, X. L. Qi, H. J. Zhang, D. H. Lu, X. Dai, Z. Fang, S. C. Zhang, I. R. Fisher, Z. Hussain, and Z.-X. Shen, "Experimental realization of a three-dimensional topological insulator, Bi_2Te_3", Science **325**, 178–181 (2009).

[39] L. Fu, "Hexagonal warping effects in the surface states of the topological insulator Bi_2Te_3", Phys. Rev. Lett. **103**, 266801 (2009).

[40] S. S. P. Parkin, M. Hayashi, and L. Thomas, "Magnetic domain-wall racetrack memory", Science **320**, 190–194 (2008).

[41] A. Fert, V. Cros, and J. Sampaio, "Skyrmions on the track", Nature Nanotech **8**, 152–156 (2013).

[42] A. Fert, N. Reyren, and V. Cros, "Magnetic skyrmions: advances in physics and potential applications", Nat Rev Mater **2**, 1–15 (2017).

[43] S. Rohart, J. Miltat, and A. Thiaville, "Path to collapse for an isolated Néel skyrmion", Phys. Rev. B **93**, 214412 (2016).

[44] F. Jonietz, S. Mühlbauer, C. Pfleiderer, A. Neubauer, W. Münzer, A. Bauer, T. Adams, R. Georgii, P. Böni, R. A. Duine, K. Everschor, M. Garst, and A. Rosch, "Spin transfer torques in MnSi at ultralow current densities", Science **330**, 1648–1651 (2010).

[45] X. Z. Yu, N. Kanazawa, W. Z. Zhang, T. Nagai, T. Hara, K. Kimoto, Y. Matsui, Y. Onose, and Y. Tokura, "Skyrmion flow near room temperature in an ultralow current density", Nature Communications **3**, 988 (2012).

[46] N. Romming, C. Hanneken, M. Menzel, J. E. Bickel, B. Wolter, K. von Bergmann, A. Kubetzka, and R. Wiesendanger, "Writing and deleting single magnetic skyrmions", Science **341**, 636–639 (2013).

[47] N. Romming, A. Kubetzka, C. Hanneken, K. von Bergmann, and R. Wiesendanger, "Field-dependent size and shape of single magnetic skyrmions", Phys. Rev. Lett. **114**, 177203 (2015).

[48] A. Neubauer, C. Pfleiderer, B. Binz, A. Rosch, R. Ritz, P. G. Niklowitz, and P. Böni, "Topological Hall effect in the A phase of MnSi", Phys. Rev. Lett. **102**, 186602 (2009).

[49] S. Mühlbauer, B. Binz, F. Jonietz, C. Pfleiderer, A. Rosch, A. Neubauer, R. Georgii, and P. Böni, "Skyrmion lattice in a chiral magnet", Science **323**, 915–919 (2009).

[50] N. Kanazawa, Y. Onose, T. Arima, D. Okuyama, K. Ohoyama, S. Wakimoto, K. Kakurai, S. Ishiwata, and Y. Tokura, "Large topological Hall effect in a short-period helimagnet MnGe", Phys. Rev. Lett. **106**, 156603 (2011).

[51] N. Kanazawa, M. Kubota, A. Tsukazaki, Y. Kozuka, K. S. Takahashi, M. Kawasaki, M. Ichikawa, F. Kagawa, and Y. Tokura, "Discretized topological Hall effect emerging from skyrmions in constricted geometry", Phys. Rev. B **91**, 041122 (2015).

[52] K. Hamamoto, M. Ezawa, and N. Nagaosa, "Quantized topological Hall effect in skyrmion crystal", Phys. Rev. B **92**, 115417 (2015).

[53] B. Göbel, A. Mook, J. Henk, and I. Mertig, "Unconventional topological hall effect in skyrmion crystals caused by the topology of the lattice", Phys. Rev. B **95**, Publisher: American Physical Society, 094413 (2017).

[54] D. Maccariello, W. Legrand, N. Reyren, K. Garcia, K. Bouzehouane, S. Collin, V. Cros, and A. Fert, "Electrical detection of single magnetic skyrmions in metallic multilayers at room temperature", Nature Nanotechnology **13**, 233–237 (2018).

[55] K. S. Denisov, I. V. Rozhansky, M. N. Potkina, I. S. Lobanov, E. Lähderanta, and V. M. Uzdin, "Topological Hall effect for electron scattering on nanoscale skyrmions in external magnetic field", Phys. Rev. B **98**, 214407 (2018).

[56] N. Nagaosa, J. Sinova, S. Onoda, A. H. MacDonald, and N. P. Ong, "Anomalous Hall effect", Rev. Mod. Phys. **82**, 1539–1592 (2010).

[57] D. M. Crum, M. Bouhassoune, J. Bouaziz, B. Schweflinghaus, S. Blügel, and S. Lounis, "Perpendicular reading of single confined magnetic skyrmions", Nature Communications **6**, 8541 (2015).

[58] I. Lima Fernandes, J. Bouaziz, S. Blügel, and S. Lounis, "Universality of defect-skyrmion interaction profiles", Nature Communications **9**, 4395 (2018).

[59] P. Hohenberg and W. Kohn, "Inhomogeneous electron gas", Phys. Rev. **136**, B864–B871 (1964).

[60] W. Kohn and L. J. Sham, "Self-consistent equations including exchange and correlation effects", Phys. Rev. **140**, A1133–A1138 (1965).

[61] J. P. Perdew and W. Yue, "Accurate and simple density functional for the electronic exchange energy: generalized gradient approximation", Phys. Rev. B **33**, 8800–8802 (1986).

[62] V. L. Moruzzi, J. F. Janak, and A. R. Williams, *Calculated electronic properties of metals* (1978).

[63] S. H. Vosko, L. Wilk, and M. Nusair, "Accurate spin-dependent electron liquid correlation energies for local spin density calculations: a critical analysis", Can. J. Phys. **58**, 1200–1211 (1980).

[64] U. v. Barth and L. Hedin, "A local exchange-correlation potential for the spin polarized case. i", J. Phys. C: Solid State Phys. **5**, 1629–1642 (1972).

[65] E. N. Economou, *Green's functions in quantum physics* (Springer, 2006).

[66] J. Zabloudil, R. Hammerling, P. Weinberger, and L. Szunyogh, *Electron scattering in solid matter* (Springer, 2005).

[67] A. Gonis and W. H. Butler, *Multiple scattering in solids* (Springer, 2000).

[68] A. Böhm, *Quantum mechanics: foundations and applications* (Springer-Verlag, 1993).

[69] D. S. G. Bauer, "Development of a relativistic full-potential first-principles multiple scattering green function method applied to complex magnetic textures of nano structures at surfaces", PhD thesis (Forschungszentrum Jülich, 2014).

[70] R. Zeller, "Multiple-scattering solution of schrodinger's equation for potentials of general shape", J. Phys. C: Solid State Phys. **20**, 2347–2360 (1987).

[71] S. Heers, "Effect of spin-orbit scattering on transport properties of low-dimensional dilute alloys", PhD thesis (RWTH Aachen University, Aachen, 2011).

[72] B. Zimmermann, "Ab initio description of transverse transport due to impurity scattering in transition metals", PhD thesis (RWTH Aachen University, 2014).

[73] M. Gradhand, D. V. Fedorov, P. Zahn, and I. Mertig, "Extrinsic spin Hall effect from first principles", Phys. Rev. Lett. **104**, 186403 (2010).

[74] I. Mertig, "Transport properties of dilute alloys", Rep. Prog. Phys. **62**, 237–276 (1999).

[75] N. H. Long, P. Mavropoulos, B. Zimmermann, D. S. G. Bauer, S. Blügel, and Y. Mokrousov, "Spin relaxation and spin Hall transport in 5d transition-metal ultrathin films", Phys. Rev. B **90**, 064406 (2014).

[76] K. Tauber, D. V. Fedorov, M. Gradhand, and I. Mertig, "Spin Hall and spin Nernst effect in dilute ternary alloys", Phys. Rev. B **87**, 161114 (2013).

[77] W. Kohn and J. M. Luttinger, "Quantum theory of electrical transport phenomena", Phys. Rev. **108**, 590–611 (1957).

[78] W. H. Butler, "Theory of electronic transport in random alloys: Korringa-Kohn-Rostoker coherent-potential approximation", Phys. Rev. B **31**, 3260–3277 (1985).

[79] B. Zimmermann, P. Mavropoulos, N. H. Long, C.-R. Gerhorst, S. Blügel, and Y. Mokrousov, "Fermi surfaces, spin-mixing parameter, and colossal anisotropy of spin relaxation in transition metals from ab initio theory", Phys. Rev. B **93**, 144403 (2016).

[80] O. Wessely, B. Skubic, and L. Nordström, "Current driven magnetization dynamics in helical spin density waves", Phys. Rev. Lett. **96**, 256601 (2006).

[81] G. Géranton, "Intrinsic and extrinsic spin-orbit torques from first principles", PhD thesis (Forschungszentrum Jülich, 2017).

[82] P. Sessi, F. Reis, T. Bathon, K. A. Kokh, O. E. Tereshchenko, and M. Bode, "Signatures of dirac fermion-mediated magnetic order", Nature Communications **5**, 1–8 (2014).

[83] P. Rüßmann, S. K. Mahatha, P. Sessi, M. A. Valbuena, T. Bathon, K. Fauth, S. Godey, A. Mugarza, K. A. Kokh, O. E. Tereshchenko, P. Gargiani, M. Valvidares, E. Jiménez, N. B. Brookes, M. Bode, G. Bihlmayer, S. Blügel, P. Mavropoulos, C. Carbone, and A. Barla, "Towards microscopic control of the magnetic exchange coupling at the surface of a topological insulator", J. Phys. Mater. **1**, 015002 (2018).

[84] T. Eelbo, M. Waśniowska, M. Sikora, M. Dobrzański, A. Kozłowski, A. Pulkin, G. Autès, I. Miotkowski, O. V. Yazyev, and R. Wiesendanger, "Strong out-of-plane magnetic anisotropy of fe adatoms on Bi_2Te_3", Phys. Rev. B **89**, 104424 (2014).

[85] A. Kosma, P. Rüßmann, S. Blügel, and P. Mavropoulos, "Strong spin-orbit torque effect on magnetic defects due to topological surface state electrons in Bi_2Te_3", Phys. Rev. B **102**, 144424 (2020).

[86] K. v. Klitzing, G. Dorda, and M. Pepper, "New method for high-accuracy determination of the fine-structure constant based on quantized hall resistance", Phys. Rev. Lett. **45**, 494–497 (1980).

[87] K. von Klitzing, "The quantized Hall effect", Rev. Mod. Phys. **58**, 519–531 (1986).

[88] D. J. Thouless, M. Kohmoto, M. P. Nightingale, and M. den Nijs, "Quantized Hall conductance in a two-dimensional periodic potential", Phys. Rev. Lett. **49**, 405–408 (1982).

[89] Y. Mokrousov, *Berry phase in quantum mechanics* (Forschungszentrum Jülich GmbH Zentralbibliothek, Verlag, 2017).

[90] F. D. M. Haldane, "Model for a quantum Hall effect without Landau levels: Condensed-matter realization of the "parity anomaly"", Phys. Rev. Lett. **61**, 2015–2018 (1988).

[91] C.-Z. Chang, J. Zhang, X. Feng, J. Shen, Z. Zhang, M. Guo, K. Li, Y. Ou, P. Wei, L.-L. Wang, Z.-Q. Ji, Y. Feng, S. Ji, X. Chen, J. Jia, X. Dai, Z. Fang, S.-C. Zhang, K. He, Y. Wang, L. Lu, X.-C. Ma, and Q.-K. Xue, "Experimental observation of the quantum anomalous Hall effect in a magnetic topological insulator", Science **340**, 167–170 (2013).

[92] B. A. Bernevig, T. L. Hughes, and S.-C. Zhang, "Quantum spin Hall effect and topological phase transition in HgTe quantum wells", Science **314**, 1757–1761 (2006).

[93] M. König, S. Wiedmann, C. Brüne, A. Roth, H. Buhmann, L. W. Molenkamp, X.-L. Qi, and S.-C. Zhang, "Quantum spin Hall insulator state in HgTe quantum wells", Science **318**, 766–770 (2007).

[94] L. Fu and C. L. Kane, "Topological insulators with inversion symmetry", Phys. Rev. B **76**, 045302 (2007).

[95] J. E. Moore and L. Balents, "Topological invariants of time-reversal-invariant band structures", Phys. Rev. B **75**, 121306 (2007).

[96] D. Hsieh, D. Qian, L. Wray, Y. Xia, Y. S. Hor, R. J. Cava, and M. Z. Hasan, "A topological Dirac insulator in a quantum spin Hall phase", Nature **452**, 970–974 (2008).

[97] P. Roushan, J. Seo, C. V. Parker, Y. S. Hor, D. Hsieh, D. Qian, A. Richardella, M. Z. Hasan, R. J. Cava, and A. Yazdani, "Topological surface states protected from backscattering by chiral spin texture", Nature **460**, 1106–1109 (2009).

[98] W. Zhang, R. Yu, H.-J. Zhang, X. Dai, and Z. Fang, "First-principles studies of the three-dimensional strong topological insulators Bi_2Te_3, Bi_2Se_3 and Sb_2Te_3", New J. Phys. **12**, 065013 (2010).

[99] A. Kosma, "Calculations of spin transport properties on topological insulator surfaces doped with magnetic defects", masterthesis (National and Kapodistrian University of Athens, 2018).

[100] *Jukkr*, `https://jukkr.fz-juelich.de/`.

[101] R. Zeller, "An elementary derivation of Lloyd's formula valid for full-potential multiple-scattering theory", J. Phys.: Condens. Matter **16**, 6453 (2004).

[102] R. Zeller, "Lloyd's formula in multiple-scattering calculations with finite temperature", J. Phys.: Condens. Matter **17**, 5367 (2005).

[103] K. D. Belashchenko, A. A. Kovalev, and M. van Schilfgaarde, "First-principles calculation of spin-orbit torque in a Co/Pt bilayer", Phys. Rev. Materials **3**, 011401 (2019).

[104] P. Rüßmann, "Spin scattering of topologically protected electrons at defects", PhD thesis (RWTH Aachen University, Aachen, 2018).

[105] W.-C. Lee, C. Wu, D. P. Arovas, and S.-C. Zhang, "Quasiparticle interference on the surface of the topological insulator Bi_2Te_3", Phys. Rev. B **80**, 245439 (2009).

[106] A. N. Bogdanov and U. K. Rößler, "Chiral symmetry breaking in magnetic thin films and multilayers", Phys. Rev. Lett. **87**, 037203 (2001).

[107] U. K. Rößler, A. N. Bogdanov, and C. Pfleiderer, "Spontaneous skyrmion ground states in magnetic metals", Nature **442**, 797–801 (2006).

[108] X. Z. Yu, Y. Onose, N. Kanazawa, J. H. Park, J. H. Han, Y. Matsui, N. Nagaosa, and Y. Tokura, "Real-space observation of a two-dimensional skyrmion crystal", Nature **465**, 901–904 (2010).

[109] N. Nagaosa and Y. Tokura, "Topological properties and dynamics of magnetic skyrmions", Nature Nanotechnology **8**, 899–911 (2013).

[110] S. Heinze, K. von Bergmann, M. Menzel, J. Brede, A. Kubetzka, R. Wiesendanger, G. Bihlmayer, and S. Blügel, "Spontaneous atomic-scale magnetic skyrmion lattice in two dimensions", Nature Phys **7**, 713–718 (2011).

[111] F. R. Lux, F. Freimuth, S. Blügel, and Y. Mokrousov, "Chiral and topological orbital magnetism of spin textures", `10.48550/arXiv.1706.06068` (2017).

[112] N. Papanicolaou and T. N. Tomaras, "Dynamics of magnetic vortices", Nuclear Physics B **360**, 425–462 (1991).

[113] B. Göbel, I. Mertig, and O. A. Tretiakov, "Beyond skyrmions: Review and perspectives of alternative magnetic quasiparticles", Physics Reports **895**, 1–28 (2021).

[114] O. A. Tretiakov and O. Tchernyshyov, "Vortices in thin ferromagnetic films and the skyrmion number", Phys. Rev. B **75**, 012408 (2007).

[115] M. Hoffmann, B. Zimmermann, G. P. Müller, D. Schürhoff, N. S. Kiselev, C. Melcher, and S. Blügel, "Antiskyrmions stabilized at interfaces by anisotropic Dzyaloshinskii-Moriya interactions", Nature Communications **8**, 10.1038/s41467-017-00313-0 (2017).

[116] I. Kézsmárki, S. Bordács, P. Milde, E. Neuber, L. M. Eng, J. S. White, H. M. Rønnow, C. D. Dewhurst, M. Mochizuki, K. Yanai, H. Nakamura, D. Ehlers, V. Tsurkan, and A. Loidl, "Néel-type skyrmion lattice with confined orientation in the polar magnetic semiconductor GaV_4S_8", Nature Materials **14**, 1116–1122 (2015).

[117] I. Dzyaloshinsky, "A thermodynamic theory of "weak" ferromagnetism of antiferromagnetics", Journal of Physics and Chemistry of Solids **4**, 241–255 (1958).

[118] T. Moriya, "Anisotropic superexchange interaction and weak ferromagnetism", Phys. Rev. **120**, 91–98 (1960).

[119] A. Crépieux and C. Lacroix, "Dzyaloshinsky–moriya interactions induced by symmetry breaking at a surface", Journal of Magnetism and Magnetic Materials **182**, 341–349 (1998).

[120] P. F. Bessarab, V. M. Uzdin, and H. Jónsson, "Method for finding mechanism and activation energy of magnetic transitions, applied to skyrmion and antivortex annihilation", Computer Physics Communications **196**, 335–347 (2015).

[121] C. Hanneken, A. Kubetzka, K. v. Bergmann, and R. Wiesendanger, "Pinning and movement of individual nanoscale magnetic skyrmions via defects", New J. Phys. **18**, 055009 (2016).

[122] Y. Yafet, *g Factors and spin-lattice relaxation of conduction electrons*, Vol. 14 (1963), pp. 1–98.

[123] B. Dupé, M. Hoffmann, C. Paillard, and S. Heinze, "Tailoring magnetic skyrmions in ultra-thin transition metal films", Nature Communications **5**, 4030 (2014).

[124] E. Simon, K. Palotás, L. Rózsa, L. Udvardi, and L. Szunyogh, "Formation of magnetic skyrmions with tunable properties in PdFe bilayer deposited on Ir(111)", Phys. Rev. B **90**, 094410 (2014).

[125] J. Bouaziz, "Spin-orbitronics at the nanoscale: from analytical models to real materials", PhD thesis (Forschungszentrum Jülich, 2019).

[126] S. Komineas, C. Melcher, and S. Venakides, "The profile of chiral skyrmions of small radius", Nonlinearity **33**, 3395 (2020).

[127] H. Jia, B. Zimmermann, M. Hoffmann, M. Sallermann, G. Bihlmayer, and S. Blügel, "Material systems for FM-/AFM-coupled skyrmions in Co/Pt-based multilayers", Phys. Rev. Materials **4**, 094407 (2020).

[128] X. S. Wang, H. Y. Yuan, and X. R. Wang, "A theory on skyrmion size", Communications Physics **1**, 1–7 (2018).

[129] K. Everschor-Sitte, J. Masell, R. M. Reeve, and M. Kläui, "Perspective: magnetic skyrmions—overview of recent progress in an active research field", Journal of Applied Physics **124**, Publisher: American Institute of Physics, 240901 (2018).

[130] S. Wimmer, K. Chadova, M. Seemann, D. Ködderitzsch, and H. Ebert, "Fully relativistic description of spin-orbit torques by means of linear response theory", Phys. Rev. B **94**, 054415 (2016).

[131] A. Soumyanarayanan, M. Raju, A. L. Gonzalez Oyarce, A. K. C. Tan, M.-Y. Im, A. P. Petrović, P. Ho, K. H. Khoo, M. Tran, C. K. Gan, F. Ernult, and C. Panagopoulos, "Tunable room-temperature magnetic skyrmions in Ir/Fe/Co/Pt multilayers", Nature Materials **16**, 898–904 (2017).

[132] K. Zeissler, S. Finizio, K. Shahbazi, J. Massey, F. A. Ma'Mari, D. M. Bracher, A. Kleibert, M. C. Rosamond, E. H. Linfield, T. A. Moore, J. Raabe, G. Burnell, and C. H. Marrows, "Discrete Hall resistivity contribution from Néel skyrmions in multilayer nanodiscs", Nature Nanotechnology **13**, 1161–1166 (2018).

[133] M. Raju, A. Yagil, A. Soumyanarayanan, A. K. C. Tan, A. Almoalem, F. Ma, O. M. Auslaender, and C. Panagopoulos, "The evolution of skyrmions in Ir/Fe/Co/Pt multilayers and their topological Hall signature", Nature Communications **10**, 696 (2019).

[134] Q. Shao, Y. Liu, G. Yu, S. K. Kim, X. Che, C. Tang, Q. L. He, Y. Tserkovnyak, J. Shi, and K. L. Wang, "Topological Hall effect at above room temperature in heterostructures composed of a magnetic insulator and a heavy metal", Nature Electronics **2**, 182–186 (2019).

[135] A. S. Ahmed, A. J. Lee, N. Bagués, B. A. McCullian, A. M. A. Thabt, A. Perrine, P.-K. Wu, J. R. Rowland, M. Randeria, P. C. Hammel, D. W. McComb, and F. Yang, "Spin-Hall topological Hall effect in highly tunable Pt/ferrimagnetic-insulator bilayers", Nano Lett. **19**, 5683–5688 (2019).

[136] E. H. Hall, "On a new action of the magnet on electric currents", American Journal of Mathematics **2**, 287–292 (1879).

[137] E. Hall, "On the "Rotational Coefficient" in nickel and cobalt", The London, Edinburgh, and Dublin Philosophical Magazine and Journal of Science **12** (1881).

[138] J. M. Luttinger, "Theory of the Hall effect in ferromagnetic substances", Phys. Rev. **112**, 739–751 (1958).

[139] J. Smit, "The spontaneous Hall effect in ferromagnetics I", Physica **21**, 877–887 (1955).

[140] P. Bruno, V. K. Dugaev, and M. Taillefumier, "Topological Hall effect and Berry phase in magnetic nanostructures", Phys. Rev. Lett. **93**, 096806 (2004).

[141] F. Freimuth, R. Bamler, Y. Mokrousov, and A. Rosch, "Phase-space Berry phases in chiral magnets: Dzyaloshinskii-Moriya interaction and the charge of skyrmions", Phys. Rev. B **88**, 214409 (2013).

[142] C. Franz, F. Freimuth, A. Bauer, R. Ritz, C. Schnarr, C. Duvinage, T. Adams, S. Blügel, A. Rosch, Y. Mokrousov, and C. Pfleiderer, "Real-space and reciprocal-space Berry phases in the Hall effect of $Mn_{1-x}Fe_xSi$", Phys. Rev. Lett. **112**, 186601 (2014).

[143] S. S.-L. Zhang and O. Heinonen, "Topological Hall effect in diffusive ferromagnetic thin films with spin-flip scattering", Phys. Rev. B **97**, 134401 (2018).

List of Publications

Publication in international refereed journal

- A. Kosma, P. Rüßmann, S. Blügel, and P. Mavropoulos, "Strong spin-orbit torque effect on magnetic defects due to topological surface state electrons in Bi_2Te_3". Phys. Rev. B **102**, 144424 (2020). http://doi.org/10.1103/PhysRevB.102.144424

Presentations in Conferences and Workshops

- A. Kosma, P. Rüßmann, S. Blügel, and P. Mavropoulos, "Spin-orbit torque on the magnetization of defects on the surface of the topological insulator Bi_2Te_3", XXXIII Panhellenic Conference on Solid State Physics and Materials Science Nicosia, September 2018 (Best poster award).
- A. Kosma, P. Rüßmann, S. Blügel, and P. Mavropoulos, "Spin-orbit torque in the surface of the topological insulator Bi_2Te_3 doped with magnetic defects", DPG Spring Meeting of the Condensed Matter Section, Regensburg, April 2019.
- A. Kosma, P. Rüßmann, S. Blügel, and P. Mavropoulos, "Calculations of spin transport properties on topological insulator surfaces doped with magnetic defects", XXXIV Panhellenic Conference on Solid State Physics and Materials Science, Patras, September 2019 (2nd Prize of the Best M.Sc. Thesis Award 2019 on Condensed Matter and Materials Science).
- A. Kosma, P. Rüßmann, S. Blügel, and P. Mavropoulos, "Spin-orbit torque effect in the surface of Bi_2Te_3 doped with magnetic transition-metal defects", WE-Heraus-Seminar on Spin Transport in Complex Magnetic Structures, Physikzentrum Bad Honnef, Germany, January 2020.
- P. Mavropoulos and A. Kosma, "Electrical control of magnetization by spin orbit torque in doped topological insulator surfaces", Online workshop on Computational Materials Science, December 2020.
- A. Kosma, P. Rüßmann, S. Blügel, and P. Mavropoulos, "Magnetic skyrmions in ultrathin film Pd/Fe/Ir(111): an ab-initio study", XXXV Panhellenic Conference on Solid State Physics and Materials Science, September 2021, Athens, Greece.
- A. Kosma, P. Rüßmann, S. Blügel, and P. Mavropoulos, "Spin-orbit torque on magnetic transition-metal defects in the surface of the topological insulator Bi2Te3. Topology in modern condensed matter physics and beyond: from fundamentals to quantum applications", SPP1666 Young Researchers Workshop, October 2021, Munich, Germany.

- A. Kosma, P. Rüßmann, S. Blügel, and P. Mavropoulos, "Ab-initio study of the Topological Hall effect in magnetic skyrmions in Pd/Fe/Ir(111)", Young researchers retreat on Topological Spin Phenomena in Real-Space for Applications, Annweiler am Trifels, Germany, September 2022.

Acknowledgements

First of all, I would like to express my deepest gratitude to my supervisor Prof. Phivos Mavropoulos for his excellent guidance and constant support throughout this journey in the scientific world. I learned so much from our countless discussions which ranged over general condensed matter physics to the field of the simulations related to spin-transport phenomena, and the KKR world. Thank you Phivos for the continuous mentoring and the encouragement you always provided me with throughout these years. I couldn't have wished for a better supervisor.

I am most grateful to Prof. Nikolaos Stefanou for the plethora of scientific discussions, and his valuable advice during the years of my studies, and for his willingness to devote time on the examination of this thesis.

I am thankful to Prof. Yuriy Mokrousov for our fruitful discussions and for sharing with me his expertise related to spin-orbit torque phenomena, as well as for his willingness to examine this thesis and be my co-advisor during my visit in Forschungszentrum Jülich (PGI-1/IAS-1) within the DAAD grant.

I am grateful to Dr. Marjana Lezaic, Dr. Athanasios Dimoulas, Prof. Iosif Galanakis, and Prof. George Kioseoglou for being members of the Examination Committee.

I would also like to express my special thanks to Dr. Philipp Rüßmann for the enjoyable collaboration and his valuable help, as well as for sharing with me his strong expertise in KKR codes; I always enjoy working with you!

I am deeply thankful to Prof. Stefan Blügel for the fruitful and motivating discussions we had, and for providing me with excellent working environment during my visits at the institute "Quantum Theory of Materials" at the Peter Grünberg Institut and Institute for Advanced Simulation.

I want to thank Dr. Imara Fernandes and Dr. Juba Bouaziz for sharing with me their knowledge in skyrmions systems.

I would also like to thank the members of the group and many of my colleagues who I met during my time at the Department of Physics. Special thanks to my friend and my long-term office-mate Dr. Petros Pantazopoulos for his continuous mental support and for making the office the most enjoyable working place, and also to my friend and colleague Dr. Dimitra Manousou for the support and the great moments throughout the years of PhD studies that we shared together.

Special thanks to the members of PGI-1/IAS-1. My visits in Germany were always enjoyable with you.

Financial support by the Hellenic Foundation for Research and Innovation (HFRI) for this research work under the HFRI PhD Fellowship grant (No. 1314), as well as computational support from the Greek Research & Technology Network (GRNET) in the National HPC facility – ARIS are gratefully acknowledged.

I also acknowledge the German Academic Exchange Service (DAAD) for supporting my visit in the Forschungzentrum Jülich, Peter Grünberg Institut and Institute for Advanced

Simulation, for 5 months in 2020-2021, the EC Research Innovation Action under the H2020 Programme for supporting my visit in the Peter Grünberg Institut and Institute for Advanced Simulation for 2 months in 2022 under the H2020 Programme under the Project HPC-EUROPA3 (HPC17CTZOF); in particular, and the computer resources and technical support provided by HLRS.

A big thanks to all my friends for their constant support and for making life so enjoyable during these years.

Last but not least, I want to thank my biggest supporters, my mother Marina, my father Nikos, and my brother Dimitris, for being always by my side. This thesis is devoted to my family! Μαμά, μπαμπά, ευχαριστώ!